Beam focusing and consequences for Doppler backscattering measurements

J. Ruiz Ruiz[1], F.I. Parra[2], V.H. Hall-Chen[3], N. Belrhali[4], C. Giroud[5], J.C. Hillesheim[6], N.A. Lopez[1] and JET contributors[†]

[1]Rudolf Peierls Centre for Theoretical Physics, University of Oxford, Oxford OX1 3NP, UK
[2]Princeton Plasma Physics Laboratory, Princeton, NJ 08543, USA
[3]Future Energy Acceleration and Translation Programme, Agency of Science, Technology and Research (A*STAR)138632, Singapore, Republic of Singapore
[4]Ecole Normale Supérieure (ENS), Paris, France
[5]CCFE, Culham Science Centre, Abingdon OX14 3DB, UK
[6]Commonwealth Fusion Systems, Devens, MA, USA

Corresponding author: J. Ruiz Ruiz, juan.ruiz@physics.ox.ac.uk

The phenomenon of focusing of microwave beams in a plasma near a turning-point caustic is discussed by exploiting the analytical solution to the Gaussian beam-tracing equations in the two-dimensional (2-D) linear-layer problem. The location of maximum beam focusing and the beam width at that location are studied in terms of the beam initial conditions. This focusing must be taken into account to interpret Doppler backscattering (DBS) measurements. We find that the filter function that characterises the scattering intensity contribution along the beam path through the plasma is inversely proportional to the beam width, predicting enhanced scattering from the beam focusing region. We show that the DBS signal enhancement for decreasing incident angles between the beam path and the density gradient is due to beam focusing and not due to forward scattering, as was originally proposed by (Gusakov *et al.*, (Plasma Phys. Contr. Fusion, vol. 56, 2014, p. 0250092014, 2017); Plasma Phys. Rep. vol. 43(6), 2017, pp. 605–613). The analytic beam model is used to predict the measurement of the k_y density-fluctuation wavenumber power spectrum via DBS, showing that, in an NSTX-inspired example, the spectral exponent of the turbulent, intermediate-to-high k_y density-fluctuation spectrum might be quantitatively measurable via DBS, but not the spectral peak corresponding to the driving scale of the turbulent cascade.

Keywords: Fusion Plasma, Plasma Diagnostics, Plasma Waves

[†]See the author list of 'Overview of T and D-T results in JET with ITER-like wall' by CF Maggi *et al.* to be published in Nuclear Fusion Special Issue: Overview and Summary Papers from the 29th Fusion Energy Conference (London, UK, 16–21 October 2023)

1. Introduction

The confinement of plasmas in magnetically confined fusion experiments, such as tokamaks and stellarators, is dictated by small-scale microturbulence fluctuations. The turbulence produces anomalous transport of particles and heat, determining the background equilibrium profiles of density and temperature. In the past decades, we have improved our understanding of microturbulence fluctuations and their related anomalous transport using experimental measurements (Liewer 1985; Tynan, Fujisawa & McKee 2009), analytical calculations of the micro-instabilities driving the turbulence (Horton 1999; Garbet 2001), and using direct numerical turbulence simulations (Garbet *et al.* 2010) and reduced fluid models (Staebler, Kinsey & Waltz 2005; Ivanov *et al.* 2020). To study turbulence in magnetic confinement fusion devices, the theory of gyrokinetics (Catto 1978; Frieman & Chen 1982) has been developed. Gyrokinetics has been highly successful at predicting the linear micro-instabilities driving turbulence and the associated transport. Due to the complexity of the equations, only linear calculations are analytically tractable in certain limits, but these cannot predict the saturated turbulence. To systematically study the turbulence saturated state and transport, the nonlinear gyrokinetic system of equations (Frieman & Chen 1982) has been implemented over the years in performance codes such as GENE (Jenko *et al.* 2000), GS2 (Kotschenreuther 1995), GYRO (Candy & Waltz 2003*a*; Candy & Belli 2014), CGYRO (Candy, Belli & Bravenec 2016), STELLA (Barnes, Parra & Landreman 2019) etc. These codes have been well benchmarked (Dimits *et al.*, 2000; Nevins *et al.* 2006; Bravenec *et al.* 2013) and have proven successful at predicting the experimentally inferred transport levels (Candy & Waltz, 2003*b*; Howard *et al.* 2013).

Gyrokinetic codes can also calculate intrinsic turbulence characteristics, some of which can be measured by fluctuation diagnostics. Detailed comparisons of the intrinsic turbulence characteristics (fluctuation spectrum, correlation length, etc.) between the measurements and simulations remain difficult, but are becoming more common practice (White *et al.* 2008; Holland *et al.* 2009; Hillesheim *et al.* 2012; Holland *et al.* 2012; Leerink *et al.* 2012; Gusakov *et al.* 2013; Stroth *et al.* 2015; Lechte *et al.* 2017; Happel *et al.* 2017; Ruiz *et al.* 2019; Krutkin *et al.*, 2019*a*). As we approach burning-plasma scenarios in the coming decade (ITER, Ikeda 2007; SPARC, Creely *et al.* 2020; STEP, Wilson *et al.* 2020), it is important to measure and characterise detailed physical turbulence processes in today's tokamaks to validate our models and to build confidence in the model's predictions for next generation fusion devices (Terry *et al.* 2008; Greenwald 2010; Holland 2016; White 2019). This motivates a detailed understanding of the complex turbulent phenomena being measured, as well as the detailed physical mechanisms in the measurement process itself. Both should be understood from a fundamental level.

To make quantitative comparisons between fluctuation diagnostics and numerical turbulence simulations, synthetic diagnostics are needed. Synthetic diagnostics enable the understanding of the diagnostic effects on the measurement (Bravenec & Nevins 2006; Shafer *et al.* 2006) and are a natural tool to help design new fluctuation diagnostics. These require a detailed understanding of the physical process behind the experimental measurement: collisional excitation and charge exchange rates in the case of beam emission spectroscopy (BES) (Fonck, Duperrex & Paul 1990; Hutchinson 2002), electron cyclotron emission (ECE) physics in the case of

ECE (Sattler, Hartfuss & Team 1994; Cima *et al.* 1995), plasma sheath physics for magnetic probe measurements (Hutchinson 2002), wave diffraction physics in phase-contrast imaging (Weisen 1988; Coda & Porkolab 1992), and microwave scattering physics in the case of microwave diagnostics such as reflectometry (Cripwell *et al.* 1989; Costley *et al.* 1990), Doppler backscattering (DBS) (Holzhauer *et al.* 1998; Hirsch *et al.* 2001) and high-k scattering (Mazzucato 1976; Surko & Slusher 1976; Slusher & Surko 1980; Peebles *et al.* 1981), to name a few. In this manuscript, we focus on the measurement of the turbulence wavenumber spectrum via DBS. We use a linear-response beam-tracing model for the propagation and scattering of the microwaves inside the plasma to assess the impact of the beam properties on the backscattered power spectrum measured by DBS.

The Doppler backscattering technique (Holzhauer *et al.* 1998; Hirsch *et al.* 2001) can measure the turbulent wavenumber spectrum (Hennequin *et al.* 2006; Hillesheim *et al.* 2015), zonal and equilibrium flows (Hirsch & Holzhauer 2004; Hennequin *et al.* 2004; Hillesheim *et al.* 2016) as well as the turbulent correlation length (Schirmer *et al.* 2007). To perform the measurement, a beam of microwaves is launched into the core plasma with a finite incidence angle α_0 with respect to the density gradient ∇n. The beam propagates in the plasma until it encounters a cutoff surface, following which the forward beam is deviated away from the detector. The detector receives backscattered radiation from all along the beam path from turbulent fluctuations with characteristic wavevector $\mathbf{k}$, which are related to the incident beam wavevector $\mathbf{K}$ via the Bragg condition for backscattering $\mathbf{k} = -2\mathbf{K}$. Despite the simple qualitative idea behind the measurement, there is very rich physics impacting the scattering measurement, such as scattering along the path (Gusakov & Surkov 2004), the mismatch angle between the incident beam $\mathbf{K}$ and the turbulence wavenumber $\mathbf{k}$ (Rhodes *et al.* 2006; Hillesheim *et al.* 2015; Hall-Chen *et al.* 2022*a*,*b*,*c*), the Doppler shift, and a nonlinear response of the diagnostic for sufficiently large fluctuations (Gusakov, Surkov & Popov 2005; Blanco & Estrada 2013; Fernández-Marina *et al.* 2014; Krutkin *et al.* 2019*b*). One option to understand some of these effects is to couple high-fidelity full-wave models with direct nonlinear gyrokinetic simulations. This is a daunting task, but has been successfully carried out by some authors in the context of DBS (Stroth *et al.* 2015; Happel *et al.* 2017; Lechte *et al.* 2017, 2020). This critical and necessary exercise validates full-physics turbulence simulations as well as full-wave codes, where agreement should be reached between the full-physics modelling and experimental measurements. When agreement is not reached, the difference might be due to insufficient physics or resolution in the simulated turbulence, full-wave simulations or both. These exercises make it difficult to isolate particular physics phenomena affecting the measurement, which hinders fundamental understanding. A second option to understand DBS is to split the problem into smaller pieces and to use reduced models for the turbulence, the wave propagation or both. With reduced models, one can make analytical progress, have a strong handle on the hypotheses and limitations and establish a clear origin of the results and predictions. The latter is the approach we have opted for in this manuscript.

First-principles theory and analytical calculations of the DBS scattered power spectra have been carried out for almost two decades by Gusakov *et al.* (Gusakov & Surkov 2004; Gusakov & Popov 2011; Gusakov *et al.* 2014, 2017). These calculations start from the full-wave analytical solution to the Helmholtz wave equation, and they are restricted to two-dimensional (2-D) geometry in a Cartesian slab, although some preliminary calculations have been performed in a cylinder (Gusakov & Krutkin 2017). In their work, Gusakov *et al.* argue that non-local 'forward-scattering'

events cause an enhancement of the DBS signal preferentially for decreasing incidence angles α_0. Gusakov *et al.* also analysed the measurement locality, challenging the traditional understanding that DBS is sensitive to fluctuations from the cutoff (in this manuscript, we will interchangeably refer to this location as the cutoff, or turning point). These calculations use a realistic representation of the wave scattering process and a simple turbulence spectrum (Gaussian) in their analytical calculations.

In this work, we adopt Gaussian beam tracing to model the propagation of the electric field in a simple 2-D slab geometry, as used previously (Gusakov & Surkov 2004; Gusakov & Popov 2011; Gusakov *et al.* 2014, 2017). The theory of Gaussian beam-tracing has been developed in different fields of physics (Casperson 1973; Červený *et al.* 1982; Yu. A. Kravtsov and Berczynski P. 2007). In magnetic confinement fusion, the theory of Gaussian beam propagation in anisotropic media has been used for approximately three decades (Pereverzev 1992, 1993, 1996, 1998; Poli, Pereverzev & Peeters 1999, 2001*b*,c) and has been successfully implemented in numerical codes such as TORBEAM (Poli *et al.* 2001*a*,2018) and more recently in Scotty (Hall-Chen *et al.* 2025) to model reflectometry/DBS and electron cyclotron (EC) beam absorption. The Gaussian beam-tracing equations are a set of ordinary differential equations (ODEs), which present great computational advantage with respect to full-wave codes, even in two dimensions. Although scarce, analytic solutions for beam-tracing exist (Maj *et al.* 2009, 2010; Weber, Maj & Poli 2018) and are exploited in this work. Previous authors have shown that the Gaussian beam-tracing model remains a good approximation when the incidence angle α_0 is not too small (Balakin *et al.* 2007, 2008; Maj *et al.* 2009, 2010). Gaussian beam tracing is bound to break near the cutoff at small angles ($\alpha_0 \sim 10°$ for $K_0 L$ values of approximately 10^3 characteristic of magnetic confinement experiments (Belrhali *et al.* 2025)). For these small angles, beam tracing could yield inaccurate predictions for a small part of the beam and the resulting scattering. Some of the concerns are revisited in this manuscript.

The rest of the manuscript proceeds as follows. In § 2, we introduce Gaussian beam tracing. We use the analytical solution by Maj *et al.* (2009, 2010) that exhibits beam focusing (also referred to as pinching or lensing) near the turning point. This phenomenon of beam focusing was already observed in past work using numerical simulations (Poli *et al.* 1999, 2001*c*; Yu. A. Kravtsov and Berczynski P., 2007; Conway *et al.* 2007). We characterise how an O-mode beam focuses in a 2-D Cartesian slab with a linear density profile as a function of the beam initial conditions. In § 3, we use the analytic solution for beam tracing in conjunction with a recently developed linear-response beam model of DBS (Hall-Chen *et al.* 2022*b*) to find an analytic expression for the DBS filter function $|F_{x\mu}|^2$. With this filter function, we develop and implement an analytic synthetic diagnostic for DBS, which can be used to analyse fluctuation data from gyrokinetic codes. In § 4, we show that by parametrising the filter function $|F_{x\mu}|^2$ by the scattered radial wavenumber component k_x of the turbulent wavevector along the path, we are able to recover previous known results for the scattered power (Gusakov & Surkov 2004; Gusakov *et al.* 2014, 2017). Our results confirm that the results by Gusakov *et al.* (2014, 2017) can be obtained using the Gaussian beam-tracing approximation, and hence, do not include full-wave effects. Gusakov *et al.* argued that the enhancement of the DBS signal power was due to a forward-scattering component, which is absent in our model by design. We find the exact same analytical formulae as Gusakov *et al.* for the DBS filter function $|F_{x\mu}|^2$ by using a model only based on backscattering and Gaussian beam tracing, instead of the full-wave solution. This suggests that forward

scattering, in the form described by Gusakov *et al.* (2014, 2017), is not the physical phenomenon leading to the enhancement of the DBS power for finite k_x values near the turning point, but rather that beam focusing is. Section 4, in conjunction with Appendices C and D, establishes the equivalence between the beam model of DBS by Hall-Chen *et al.* (2022*b*) and the 2-D DBS model by Gusakov *et al.* In the last section of this manuscript, we apply the analytical filter function $|F_{x\mu}|^2$ from the beam model to understand its effect on scattered power measurements from DBS. We use a realistic turbulence spectrum obtained from gyrokinetic simulations, following recent work by Ruiz *et al.* (2022). Our model predicts that, for a representative NSTX-inspired example, the Doppler-backscattered power spectrum cannot reproduce the peak in k_y from the true density-fluctuation spectrum, but is accurate at predicting the characteristic spectral exponent of the turbulent cascade.

2. Beam focusing and beam tracing

In DBS experiments, one can model the propagation of the microwaves launched externally from the plasma as a Gaussian beam. The behaviour of a Gaussian beam can be complex due to the inhomogeneities in density and magnetic field. To gain physical understanding of the phenomena affecting beam propagation, we first discuss vacuum propagation.

In vacuum, a Gaussian beam will propagate in a straight line. If the beam is not focusing, then it will constantly expand. Asymptotically, the width of the beam will grow linearly with the propagation path length. If the beam is initially focusing, it will focus to a minimum width, called the waist, following which the beam will expand, as previously described by Goldsmith (1998). This behaviour is due to diffraction: a wave packet of finite extent does not want to be confined: if initially expanding, it will not cease to expand; if initially focusing, it will focus before expanding.

For a beam propagating in an anisotropic, inhomogeneous medium, its trajectory can substantially differ from that in vacuum. The inhomogeneity in space causes refraction of the central ray. The inhomogeneity experienced by the central ray causes changes in the group velocity $\mathbf{g}$, which affects the intensity of the electric field, which scales as $E \propto 1/|\mathbf{g}|^{\frac{1}{2}}$ (Lopez & Dodin 2021).[1] Of particular interest is the problem of a wave encountering a cutoff surface at normal incidence. This is the situation encountered by diagnostics such as reflectometry, where the group velocity along the inhomogeneity approaches zero at the cutoff and the electric field diverges. This is a well-known limitation of beam tracing when close to normal incidence to the inhomogeneity. Close to a turning point, one cannot assume slow variation of the background experienced by the wave and the beam-tracing approximation fails. To solve this problem, one needs to resort to solving the full Helmholtz wave equation. This limitation disappears when the angle of incidence with respect to the inhomogeneity is finite (or more precisely, large enough, as we will discuss), such as encountered in DBS. The group velocity still decreases approaching the cutoff (the component of $\mathbf{g}$ along the inhomogeneity vanishes, while the $\mathbf{g}$ component perpendicular to it remains approximately constant). This produces an enhancement of the electric field E near the turning point, which should remain finite due to a

---

[1]In contrast to beam tracing, the electric field intensity in ray tracing reads $E \sim 1/(|\mathbf{g}||\cos\alpha|)^{\frac{1}{2}}$ for the 2-D linear layer (Lopez & Dodin 2021), where α is the angle between $\mathbf{g}$ and the density gradient, see figure 1 and (A.9). This divergence is integrable in ray tracing and resolved in beam tracing.

finite $|\mathbf{g}|$. The decrease of the group velocity near the turning point is one factor that enhances the electric-field amplitude in DBS and will be discussed in this manuscript. This will show up as a ray term affecting the filter function $|F_{x\mu}|^2$ for backscattering. As we will see, $|F_{x\mu}|^2 \propto 1/|\mathbf{g}| \propto 1/K$. Importantly, there is another factor that can enhance the intensity of the electric field and that is the beam width.

For a beam propagating in an anisotropic, inhomogeneous medium, the behaviour of the beam width can also be substantially different from the behaviour in vacuum. Beam tracing can describe diffraction effects due to the finite extent $\sim W$ of a wave packet in the direction transverse to the direction of propagation. In addition to the beam waist present in vacuum, other authors have shown that the beam can experience additional focusing, or lensing, in the presence of inhomogeneity (Poli *et al.* 1999, 2001*c*; Bornatici & Maj 2003; Maj 2005; Yu. A. Kravtsov and Berczynski P. 2007; Conway *et al.* 2007; Berczyński *et al.* 2008; Maj *et al.* 2009, 2010). This phenomenon tends to happen close to the turning point. In the beam-tracing formulation, one can show that the electric-field amplitude E scales inversely proportional to the beam width W, as $E \propto 1/W^{\frac{1}{2}}$ (Yu. A. Kravtsov and Berczynski P. 2007; Hall-Chen *et al.* 2022*b*).[2] This shows that when the beam focuses, the electric field is enhanced. This is a different effect from the enhancement due to the decreasing group velocity of the central ray. In fact, it can be shown that the electric field scales as $E \propto 1/(|\mathbf{g}|W)^{\frac{1}{2}}$ (Yu. A. Kravtsov and Berczynski P. 2007; Hall-Chen *et al.* 2022*b*). It is this phenomenon, the beam focusing in an inhomogeneous medium, that we explore in this manuscript. In full toroidal geometry, this results in the filter function $\propto 1/|\mathbf{g}|W \propto 1/KW$ (Hall-Chen *et al.* 2022*b*).[3] In the 2-D linear-layer model, we will find $\mathbf{g} = 2\mathbf{K}/K_0^2$ and $|F_{x\mu}|^2/|F_0|^2 = K_0 W_0/KW$, where $|F_0|^2$, K_0 and W_0 are the filter function $|F_{x\mu}|^2$, the magnitude of the beam central wavenumber $\mathbf{K}$ and the beam width W evaluated at the initial condition. We call the $1/W$ term the beam term in the filter function (Hall-Chen *et al.* 2022*b*). Importantly, the beam term and the ray term can both separately contribute to the enhancement of the electric field in the vicinity of a turning point. This motivates studying the propagation of a ray and a beam in inhomogeneous, anisotropic media. For this, we adopt the ray-tracing and beam-tracing formulation, which we describe next.

2.1. *Ray tracing and Gaussian beam tracing*

This section closely follows notation introduced by Hall-Chen *et al.* (2022*b*), who rederived Gaussian beam tracing from first principles and presented it in full detail.

The beam-tracing method (or paraxial WKB) is an asymptotic representation of the electric field in anisotropic media for finite size wave packets with characteristic scale in the transverse direction of propagation $\sim W$. Beam tracing extends ray tracing by including diffraction effects in a set of ODEs. As in ray tracing, the wavevector of the wave $\mathbf{K}$ is ordered inversely proportional to the wavelength $\sim 1/\lambda$,

---

[2]Here, we consider a 2-D configuration, with one of the directions being the direction of propagation, and the other the transverse direction. In three dimensions, there is a second transverse direction with a second characteristic width W_X. Then, in three dimensions, the electric field scales as $E \propto (WW_X)^{-\frac{1}{2}}$.

[3]Note that Hall-Chen *et al.* (2022*b*) find that the filter function $\propto 1/g^2$ (see (196)), whereas here we have $\propto 1/g$. This apparent inconsistency is due to the fact that Hall-Chen *et al.* (2022*b*) express their filter function as an integral in l, but here we express it as an integral in k_x. The additional factor of g appears from the change of integration variable from k_x to l, as shown in the comments preceding (3.13).

while the background equilibrium is assumed to vary on a scale $L \gg \lambda$. In beam tracing, the scale W is intermediate and obeys $L \gg W \gg \lambda$, with $W \sim (\lambda L)^{\frac{1}{2}}$. In this manuscript, we denote the wavevector associated with the wave with the capital letter $\mathbf{K}$. The same notation will apply to its components K_g, K_x, etc., while the wavevector components associated with the turbulence will be in lower case, e.g. k_x and k_y.

In Gaussian beam tracing, the variation of the wave electric field perpendicular to a central ray is assumed to be of Gaussian shape. The central ray propagation obeys the traditional ray-tracing equations for the ray position vector $\mathbf{q}(\tau) \sim L$ and wavevector $\mathbf{K}(\tau) \sim 1/\lambda$, where τ is a parameter along the central ray. For reference, the ray-tracing equations are

$$
\begin{aligned}
\frac{d\mathbf{q}}{d\tau} &= \nabla_K H, \\
\frac{d\mathbf{K}}{d\tau} &= -\nabla H,
\end{aligned}
\tag{2.1}
$$

where H is the cold-plasma dispersion relation and $\mathbf{g} = \nabla_K H$ is the effective group velocity. Note that there are infinite ways to define an H that give rise to the same $\mathbf{q}$ and $\mathbf{K}$ (the different definitions of H only change the dummy parameter τ). We use a specific definition that ensures that the wave electric field scales as $\sim 1/g^{\frac{1}{2}}$, where $\mathbf{g} = d\mathbf{q}/d\tau$ (see discussion in § 2.2 of Hall-Chen *et al.* (2022*b*) for details). Equations (2.1) are routinely solved by codes such as GENRAY (Smirnov *et al.* 2009).

In the Gaussian beam-tracing approximation, the beam electric field $\mathbf{E}_b$ is written in amplitude and phase as $\mathbf{E}_b(\mathbf{r}) = \mathbf{A}(\mathbf{r}) \exp[i\psi(\mathbf{r})] + $ c.c., where the phase ψ is expanded to second order about the central ray in the perpendicular direction to $\mathbf{g}$,

$$
\psi(\mathbf{r}) = s(\tau) + \mathbf{K}_w \cdot \mathbf{w} + \frac{1}{2} \mathbf{w} \cdot \boldsymbol{\Psi}_w \cdot \mathbf{w}.
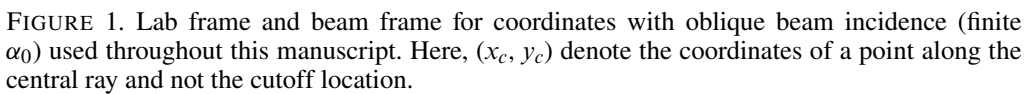\tag{2.2}
$$

Here, $s = s(\tau) = \int^{\tau} \mathbf{K}(\tau') \cdot \mathbf{g}(\tau') \, d\tau' = \int^{\tau} K_g g \, d\tau'$ is the large phase Eikonal term measuring the variation of the electric field along the central ray. The phase given by s scales as $s \sim L/\lambda \gg 1$, which follows from $\tau \sim L/\lambda$, $g \sim \lambda$ and $H \sim 1$ (see (2.1)). Note that the second term in (2.2) is ordered as $\mathbf{K}_w \cdot \mathbf{w} \sim W/\lambda \gg 1$, while the last term is $(1/2)\mathbf{w} \cdot \boldsymbol{\Psi}_w \cdot \mathbf{w} \sim 1$, since the components of $\boldsymbol{\Psi}_w$ are ordered as $\Psi_{w,ij} \sim 1/W^2$. The vector $\mathbf{K}_w = (\mathbf{I} - \hat{\mathbf{g}}\hat{\mathbf{g}}) \cdot \mathbf{K}$ in the phase (2.2) is the component of $\mathbf{K}$ perpendicular to $\hat{\mathbf{g}}$. The matrix $\boldsymbol{\Psi}_w$ is a singular 3×3 matrix and only has non-zero components along the two directions perpendicular to $\hat{\mathbf{g}}$. The matrix $\boldsymbol{\Psi}_w$ contains information about the phase-front curvature of the Gaussian beam (through the non-zero eigenvalues of its real part $= K^3/(K_g^2 R_{b,i})$, where $K = |\mathbf{K}|$ and $K_g = \mathbf{K} \cdot \hat{\mathbf{g}}$) and beam width W_i (through the non-zero eigenvalues of its imaginary part $= 2/W_i^2$).

A general point in space is described by

$$
\mathbf{r} = \mathbf{q}(\tau) + \mathbf{w} = \mathbf{q}(\tau) + X\hat{\mathbf{X}}(\tau) + Y\hat{\mathbf{Y}}(\tau).
\tag{2.3}
$$

We define the (orthonormal) beam-frame coordinate system $\{\hat{\mathbf{Y}}, \hat{\mathbf{g}}, \hat{\mathbf{X}}\}$ as follows:

$$
\hat{\mathbf{Y}} = \frac{\hat{\mathbf{b}} \times \hat{\mathbf{g}}}{|\hat{\mathbf{b}} \times \hat{\mathbf{g}}|}, \qquad \hat{\mathbf{g}} = \frac{\mathbf{g}}{g}, \qquad \hat{\mathbf{X}} = \frac{\hat{\mathbf{Y}} \times \hat{\mathbf{g}}}{|\hat{\mathbf{Y}} \times \hat{\mathbf{g}}|},
\tag{2.4}
$$

Lab frame $(\hat{\mathbf{x}}, \hat{\mathbf{y}}, \hat{\mathbf{z}})$, Beam frame $(\hat{\mathbf{Y}}, \hat{\mathbf{g}}, \hat{\mathbf{X}})$

FIGURE 1. Lab frame and beam frame for coordinates with oblique beam incidence (finite α_0) used throughout this manuscript. Here, (x_c, y_c) denote the coordinates of a point along the central ray and not the cutoff location.

where $\hat{\mathbf{b}} = \mathbf{B}/B$ is the unit vector along the background magnetic field. This is not to be confused with the Cartesian lab-frame system of coordinates $\{\hat{\mathbf{x}}, \hat{\mathbf{y}}, \hat{\mathbf{z}}\}$ (see figure 1 for a comparison between beam frame and lab frame in two dimensions). Using (2.3) and (2.4), a general point in space can be determined from the coordinate τ along the central ray and the two coordinates X and Y in the directions perpendicular to $\hat{\mathbf{g}}$.

In the beam-tracing formulation which we use in this manuscript, the beam-tracing matrix $\boldsymbol{\Psi}$ is a 3×3 matrix that is convenient to evolve along the central ray. From this matrix, we can obtain $\boldsymbol{\Psi}_w$ by projection $\boldsymbol{\Psi}_w = (\mathbf{I} - \hat{\mathbf{g}}\hat{\mathbf{g}}) \cdot \boldsymbol{\Psi} \cdot (\mathbf{I} - \hat{\mathbf{g}}\hat{\mathbf{g}})$. The beam matrix $\boldsymbol{\Psi}$ follows the beam-tracing evolution equations, a set of ordinary differential equations parametrised by τ, see Hall-Chen *et al.* (2022b) and Appendix A. Given $\boldsymbol{\Psi}$, the electric field $\mathbf{E}_b$ in Gaussian beam tracing is written as

$$
\begin{aligned}
\mathbf{E}_b = & A_{ant} \exp\left[i(\phi_G + \phi_P)\right] \left[\frac{\det\left(\Im[\boldsymbol{\Psi}_w]\right)}{\det\left(\Im[\boldsymbol{\Psi}_{w,ant}]\right)}\right]^{\frac{1}{4}} \left(\frac{g_{ant}}{g}\right)^{\frac{1}{2}} \\
& \times \exp\left(is + i\mathbf{K}_w \cdot \mathbf{w} + \frac{i}{2}\mathbf{w} \cdot \boldsymbol{\Psi}_w \cdot \mathbf{w}\right)\hat{\mathbf{e}} \; + \; c.c.,
\end{aligned}
\tag{2.5}
$$

where $\mathbf{E}_b = E_b\hat{\mathbf{e}}$ and $\Im$ denotes the imaginary part. The unit vector $\hat{\mathbf{e}}$ is the polarisation vector, ϕ_P and ϕ_G are respectively the polarisation and Gouy phases, which are of limited interest in this manuscript (see Hall-Chen *et al.* (2022b) for their evolution equations). The subscript $(.)_{ant}$ means that quantities are evaluated at the antenna launch location. As previously discussed, the prescription in (2.5) for the electric field shows that $E_b \sim 1/(gW_X W_Y)^{\frac{1}{2}} \propto 1/(KW_X W_Y)^{\frac{1}{2}}$. This is due to the terms $\det\left(\Im[\boldsymbol{\Psi}_w]\right)^{\frac{1}{4}} \propto 1/(W_X W_Y)^{\frac{1}{2}}$ and $1/g^{\frac{1}{2}} \propto 1/K^{\frac{1}{2}}$. For the purposes of this manuscript, in the 2-D linear layer, only the width W_Y in the direction $\hat{\mathbf{Y}}$ is relevant.

In the next section, we show numerical solutions to the beam-tracing equations (Appendix A) in real tokamak geometry, which exhibit the phenomenon of beam focusing. These will be compared with analytical solutions to beam tracing for the 2-D linear-layer problem. We will see how the analytical solution qualitatively captures the phenomenon of beam focusing.
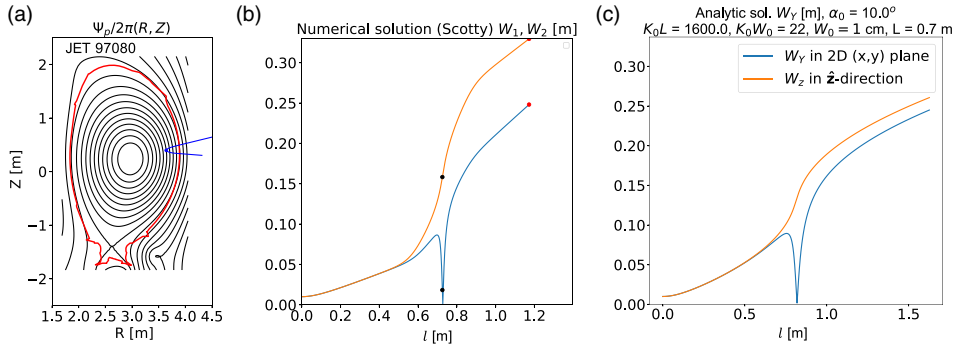
FIGURE 2. (*a*) Trajectory of the central ray of a DBS beam projected on the poloidal (R, Z) plane overlaid by contour lines of the poloidal flux function Ψ_p for JET discharge 97 080 (NBI-heated L-mode). (*b*) Numerical solution of the two principal widths perpendicular to the central ray propagation, noted here W_1 and W_2, using Scotty (Hall-Chen *et al.* 2025). The black dots correspond to the turning point in the trajectory (vanishing wavenumber component normal to the flux surface), while the red dots correspond to the plasma exit. (*c*) Analytic solution of the beam-tracing equations for the 2-D linear layer in slab geometry using experimental parameters corresponding to the case shown in panels (*a*) and (*b*): $K_0 L \approx 1600$, $K_0 W_0 \approx 22$, $\alpha_0 \approx 10°$, $R_{Y0} = \infty$ (launch at the waist). There is good qualitative agreement between the numerical and analytic solutions.

2.2. *Beam focusing in experimentally relevant conditions*

In this section, we will show that the beam-focusing phenomenon appears in numerical calculations of beam-tracing modelling of DBS experiments. We will see that the beam width has a tendency to focus as the beam moves towards higher density. A beam propagating in increasing density is routinely encountered in most DBS measurements.

We describe the phenomenon of beam focusing, that is, the decrease or compression of the beam width as the beam propagates near the turning point that characterises a cutoff. This phenomenon was previously observed in numerical simulations (Poli *et al.* 1999, 2001*c*; Yu. A. Kravtsov and Berczynski P. 2007; Conway *et al.* 2007, 2015, 2019) and in analytic solutions (Maj *et al.* 2009, 2010; Weber *et al.* 2018). To confirm the existence of the beam-focusing phenomenon and its relevance to real-life experimental conditions, in figure 2, we show the result of a numerical calculation with the Scotty code (Hall-Chen *et al.* 2025) for the DBS beam propagation with X-mode polarisation in the core of the tokamak JET for L-mode discharge 97 080 in a phase heated only by neutral-beam injection (NBI). Figure 2(*a*) shows the trajectory of the central ray projected on the 2-D (R, Z) plane overlaid by contour lines of the poloidal flux function Ψ_p. The turning point is at $\Psi_p/\Psi_{p0} \approx 0.7$, where Ψ_{p0} is the separatrix value. Figure 2(*b*) shows the perpendicular widths W_1 and W_2 that correspond to the non-zero eigenvalues of the imaginary part of the beam-tracing matrix $\Im[\boldsymbol{\Psi}_w]$. We approximate the overmoded waveguide launch by a beam with circular cross-section and initial conditions $W_0 \approx 1$ cm, $R_{Y0} = \infty$ (launch at the waist). The widths W_1 and W_2 are plotted against the path length $l = \int d\tau g$. The beam propagates in vacuum from $l \approx 0$ to $l \approx 0.4$ m, which roughly corresponds to the plasma edge. In vacuum, both principal beam widths follow the same behaviour: expansion following a launch from the waist. In the plasma, both widths initially

continue expanding, but one of them (blue) starts contracting and reaching a minimum at $l \approx 0.7$ m (beam focusing). Following the beam focusing, the contracted width starts to expand again. The behaviour observed in figure 2(*b*) consistently appears in beam-tracing numerical calculations near a turning point, and is confirmed by the beam-tracing code TORBEAM (Poli *et al.* 2001*a*, 2018) (not shown). This behaviour was also observed in simulations of DBS in other tokamaks (Conway *et al.* 2007, 2015, 2019). This motivates studying the beam-focusing phenomenon using a reduced model that is analytically tractable, the 2-D linear-layer model (Maj *et al.* 2009, 2010), which we present next.

2.3. *Beam focusing in the 2-D linear layer*

To understand the beam-focusing phenomenon observed in the Scotty numerical solution in toroidal geometry in figure 2*(b)*, we first solve the equations for ray tracing (2.1) using a simplified Cartesian-slab geometry in two dimensions (Maj *et al.* 2009, 2010). Following the ray-tracing solution, we will subsequently solve the beam-tracing equations.

We solve the 2-D linear-layer model in the lab frame, given by the unit vectors $\{\hat{\mathbf{x}}, \hat{\mathbf{y}}, \hat{\mathbf{z}}\}$ (figure 1). Using (2.4), the lab-frame unit vectors are related to the beam-frame $\{\hat{\mathbf{Y}}, \hat{\mathbf{g}}, \hat{\mathbf{X}}\}$ in two dimensions by a simple rotation

$$
\begin{aligned}
\hat{\mathbf{Y}} &= \sin \alpha \ \hat{\mathbf{x}} - \cos \alpha \ \hat{\mathbf{y}}, \\
\hat{\mathbf{g}} &= \cos \alpha \ \hat{\mathbf{x}} + \sin \alpha \ \hat{\mathbf{y}}, \\
\hat{\mathbf{X}} &= \hat{\mathbf{z}},
\end{aligned}
\tag{2.6}
$$

where we note that $\alpha = \alpha(\tau)$ is a function of τ. We will ignore the coordinate $\hat{\mathbf{z}}$, which points in the antiparallel direction to the magnetic field. These definitions will be needed in order to subsequently solve the beam-tracing equations. The 2-D linear-layer problem in slab geometry has O-mode polarisation, uniform $\mathbf{B}(\mathbf{r}) = B_0 \hat{\mathbf{b}} = -B_0 \hat{\mathbf{z}}$ and linear density profile $\omega_{pe}^2(x) = \Omega^2 x / L$. Here, x is our 'radial' coordinate, also Cartesian x in figure 1, Ω is the launch frequency, $\omega_{pe0} = \Omega \cos \alpha_0$ is the electron plasma frequency at the turning point location, $L_n = L \cos^2 \alpha_0$ is the turning point location[4] and L is the turning point location for zero incident angle ($\alpha_0 = 0$, see figure 1). The ray-tracing equations determine the trajectory of the central ray $\mathbf{q}$ and the wavevector of the central ray $\mathbf{K}$. In the 2-D linear layer, $\mathbf{q}$ and $\mathbf{K}$ have components

$$
\begin{aligned}
\mathbf{q}(\tau') &= \big(x_c(\tau'), y_c(\tau') \big), \\
\mathbf{K}(\tau') &= \big(K_x(\tau'), K_y(\tau') \big),
\end{aligned}
\tag{2.7}
$$

where $\tau' = \tau / K_0 L$ is the normalised parameter along the path and K_0 is the wavenumber magnitude at launch. Here, (x_c, y_c) denote the coordinates of an arbitrary point along the central ray and not the cutoff location. In this manuscript, we define the turning point, or cutoff, as the location where $K_x = 0$ (K_x is the Cartesian x-component of the beam wavevector $\mathbf{K}$, see (2.9)). We will make use

---

[4]L_n also corresponds to the density gradient scale length evaluated at the turning point.

of the dispersion relation $H = 0$, where H takes the form

$$H = \frac{K^2}{K_0^2} - 1 + \frac{\omega_{pe}^2}{\Omega^2} \tag{2.8}$$

for the O-mode. The form of H given by (2.8) ensures that the electric field is given by (2.5). Using (2.8), we have $\nabla_K H = \mathbf{g} = 2\mathbf{K}/K_0^2$ (initial condition $g_{ant} = 2/K_0$) and $\nabla H = \hat{\mathbf{x}}/L$. As can be seen from figure 1, the magnetic field is into the page and the angle α_0 measures the vertical incidence angle of the central ray at launch. In what follows, α will measure the vertical incidence angle along the central ray. The initial conditions are $(x_c, y_c)_0 = (0, y_0)$, $(K_x, K_y)_0 = K_0(\cos\alpha_0, \sin\alpha_0)$. The ray-tracing (2.1) can be readily solved in the 2-D linear layer, giving the following components of $\mathbf{q}$ and $\mathbf{K}$ in (2.7):

$$
\begin{aligned}
x_c(\tau') &= L\left(\cos^2\alpha_0 - (\cos\alpha_0 - \tau')^2\right) = L\left(\cos^2\alpha_0 - K_x^2/K_0^2\right), \\
y_c(\tau') &= y_0 + 2L\sin\alpha_0\ \tau', \\
K_x(\tau') &= K_0(\cos\alpha_0 - \tau') = K_0(\cos^2\alpha_0 - x_c/L)^{\frac{1}{2}}, \\
K_y(\tau') &= K_0\sin\alpha_0.
\end{aligned}
\tag{2.9}
$$

Equations (2.9) describe a parabolic trajectory in (x, y). We will find it useful to parametrise the ray trajectory by the radial wavenumber of the central ray K_x, instead of τ. We will also parametrise the beam-tracing solution by K_x.

The 2-D linear-layer problem with finite incident angle α_0 is also analytically solvable in Gaussian beam tracing, as was previously shown by Maj *et al.* (2009, 2010). For details of the derivation, we refer the reader to Appendix A. The beam-tracing equations for the linear-layer problem reduce to $\mathrm{d}\boldsymbol{\Psi}/\mathrm{d}\tau = -(2/K_0^2)\boldsymbol{\Psi}^2$, which is a nonlinear matrix equation for $\boldsymbol{\Psi}$. This equation belongs to a class of ODEs known as Ricatti equations. The main component of the beam matrix $\boldsymbol{\Psi}$ of interest in this manuscript is the $\hat{Y}\hat{Y}$ component Ψ_{YY}, which captures the beam-focusing phenomenon through the perpendicular beam width $W_Y = (2/\Im[\Psi_{YY}])^{\frac{1}{2}}$. The solution for Ψ_{YY} is

$$
\Psi_{YY}(K_x) = \frac{-\frac{1}{2}\sin^2\alpha_0 + \Psi'_{yy0}\left[\frac{K_x^3}{K_0^3} + 3\sin^2\alpha_0\frac{K_x}{K_0} - \frac{\sin^2\alpha_0}{\cos\alpha_0}\left(\cos^2\alpha_0 - \sin^2\alpha_0\right)\right]}{\left[\sin^2\alpha_0 + \frac{K_x^2}{K_0^2}\right]\left[\frac{K_x}{K_0} + 2\Psi'_{yy0}\left(\frac{\cos^2\alpha_0 - \sin^2\alpha_0}{\cos\alpha_0}\frac{K_x}{K_0} + \sin^2\alpha_0 - \frac{K_x^2}{K_0^2}\right)\right]}\frac{K_0}{L},
\tag{2.10}
$$

where $\Psi'_{yy0} = \Psi_{yy0}(L/K_0)$ is the initial condition for the beam Ψ_{yy} component in the lab-frame direction $\hat{\mathbf{y}}$ (vertical direction in figure 1) that contains information about the initial beam width and radius of curvature of the phase front (normalised to K_0/L, see Appendix A for details). Equation (2.10) is the basis for most of the analysis in this manuscript. The reader is referred to Appendix A for details in the calculation of Ψ_{YY}. The analytic solution of Ψ_{YY} contains the beam-focusing phenomenon for the 2-D linear-layer problem and is used to characterise the Doppler backscattering power contributions along the beam trajectory through the filter function $|F_{x\mu}|^2$ (§ 3).

We wish to compare the analytic beam-tracing solution for W_Y, computed using (2.10), with the numerical solution in toroidal geometry shown in figures 2(*a*) and

2(*b*). To do so, we extract the physical values of K_0, L and the initial width W_0 from experimental conditions in the JET discharge 97080: $K_0 \approx 2200$ m^{-1}, $W_0 \approx 1$ cm and $L \approx 0.7$ m. Knowing that, in reality, the beam propagates in a plasma with a varying density gradient, we choose the value of L to be the average value of the density gradient experienced by the beam as it propagates through the plasma, yielding $L \approx 0.7$ m. We use the experimental values of K_0, L and W_0 to normalise the initial conditions in the analytic beam-tracing solution, giving $K_0 W_0 \approx 22$, $K_0 L \approx 1600$. The width W_Y that is perpendicular to the central ray propagation and in the (x, y) plane is plotted in blue in figure 2(*c*), as a function of the beam path length *l*. The vacuum solution is plotted in orange (absence of plasma),[5] which is also the same solution as the $\hat{\mathbf{z}}$-component of the width for the linear layer in the $\hat{\mathbf{z}}$-direction W_z. Despite the limitations of the model (linear density profile, 2-D slab) and the difference in polarisation (X-mode versus O-mode), a qualitative comparison between figures 2(*c*) and 2(*b*) clearly shows that the analytic solution for the 2-D linear layer is able to recover the focusing behaviour observed in the numerical solution in toroidal geometry. This confirms that the beam focusing is not a numerical artefact. The beam focusing behaviour in the vicinity of the turning point is physical within the beam-tracing approximation[6] and motivates studying the beam-focusing phenomenon using the analytic solution to the beam-tracing equations in the 2-D linear-layer problem. In what follows, we describe the dependence of the analytic beam-tracing solution for Ψ_{YY} on the initial conditions for the width W_0, the radius of curvature R_{Y0} and the vertical launch angle α_0. The initial condition is at $\tau = 0$, which corresponds to the plasma edge $x = 0$.

We start by considering the analytic beam-tracing solution for $\Psi_{YY} = K/R_Y + i2/W_Y^2$ (Appendix A). In this beam-tracing solution, the dimensional quantities $K_0 = 2\pi/\lambda$, W_0 and L enter the equations through the beam parameter $W_0/(\lambda L)^{\frac{1}{2}}$. Therefore, in the rest of the manuscript, only the beam parameter $W_0/(\lambda L)^{\frac{1}{2}}$ will be specified since it is the only parameter needed to determine the normalised solution $\Psi_{YY}(L/K_0)$. The beam width W_Y is shown in figure 3 as a function of τ for different initial conditions of the incident angle $\alpha_0 = 10°$, $30°$, $50°$ and $80°$, and the initial radius of curvature R_{Y0} (coloured curves). In this slab model, we assume that plasma is only present for $x > 0$ and the vacuum exists for $x < 0$. Therefore, one needs to calculate the range of τ for which the central ray trajectory has positive x_c. According to (2.9), for initial conditions at $\tau' = 0$, the plasma exit corresponds to $\tau' = 2 \cos \alpha_0$. The initial width W_0 is kept fixed at $W_0 = 0.40(\lambda L)^{\frac{1}{2}}$. The coloured dashed lines are the vacuum solutions (absence of plasma) with initial conditions corresponding to the respective W_Y of the same colour in the 2-D linear-layer problem. The vacuum solution initially follows the plasma solution until the beam approaches the turning point. The initial value of $R_{Y0}/L = -2\cos \alpha_0/\sin^2 \alpha_0$ corresponds to the particular initial condition employed by Gusakov *et al.* (2014, 2017) (see discussion

---

[5]The solution for W_z in figure 2(*c*) corresponds to the vacuum solution. In figure 2(*c*), the widths are plotted versus the path length *l*, which introduces an apparent acceleration of the width in the $\hat{\mathbf{z}}$-direction in the vicinity of the turning point, whereas in figures 3 and 4, the vacuum widths are plotted versus τ, which shows that they evolve nearly in a straight line as a function of τ. This is because, although one can transform continuously from *l* to τ and *vice versa*, the transformation is not a simple linear one.

[6]In some cases, particularly for small incidence angles α_0, the beam-tracing approximation breaks down, and the focusing predicted by beam tracing could be unphysical. One needs more advanced models to quantify the amount of focusing in those conditions (Lopez *et al.* 2023).
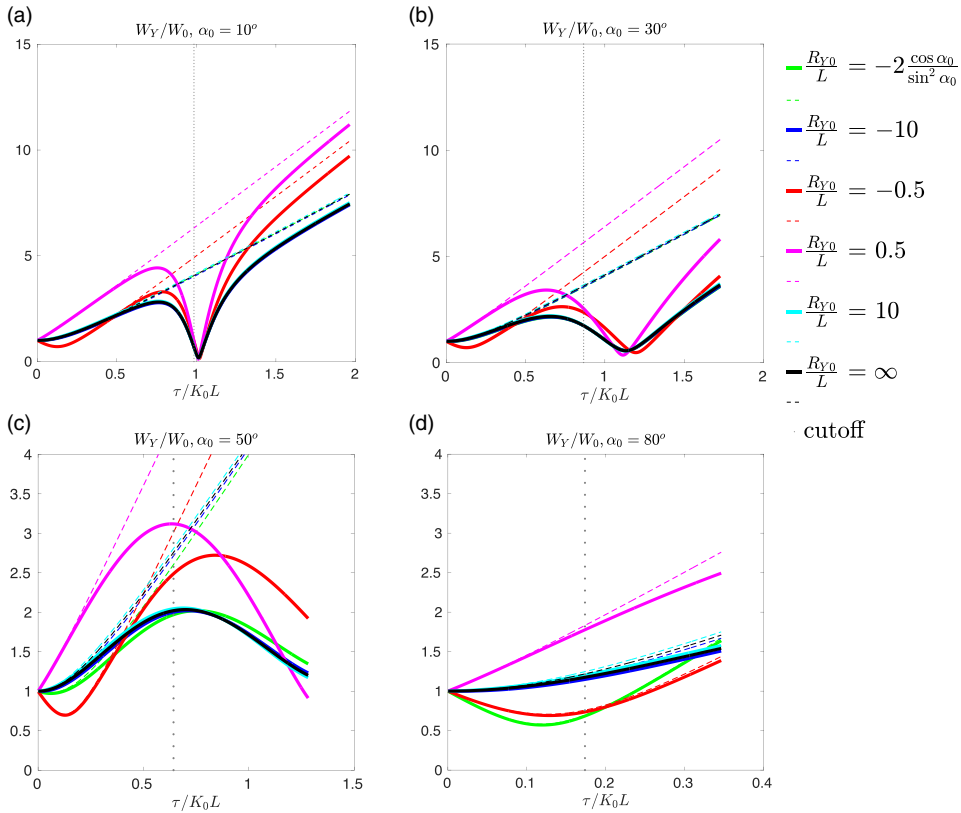
FIGURE 3. Thick coloured curves indicate values of the width W_Y for varying initial incident angle $\alpha_0 = 10°$, $30°$, $50°$ and $80°$, and different initial R_{Y0} (see legend) and fixed initial $W_0 = 0.40(\lambda L)^{\frac{1}{2}}$. Corresponding dashed lines of same colour indicate vacuum values of W_Y for same initial conditions as the thick coloured curves. The initial value of $R_{Y0}/L = -2\cos\alpha_0/\sin^2\alpha_0$ (green) corresponds to the particular initial condition employed by Gusakov *et al.* (2014, 2017). The vertical dotted points in grey indicate the location of the turning point, or cutoff (location where $K_x = 0$).

in Appendix A). For that particular case, the initial radius of curvature takes the values $R_{Y0}/L = -65.32$, -6.93, -2.19 and -0.3581 respectively for $\alpha_0 = 10°$, $30°$, $50°$ and $80°$. Here, R_{Y0} has little effect on the beam focusing around $\tau' \approx 1$ for small angles, but has a non-negligible effect in the vicinity of the initial launch and after the turning point for the outgoing beam. These differences appear for small initial $|R_{Y0}|/L \lesssim 1$, that is, for strongly focusing or diverging beams (see red and magenta curves in figure 3). The initial radius of curvature R_{Y0} becomes more important in the vicinity of the turning point for increasing incident angles, where the beam focusing location is shifted (see $\alpha_0 = 30°$). For $\alpha_0 = 50°$, $80°$, the beam focusing does not take place inside the plasma. The only focusing region corresponds to the beam waist that is captured by the vacuum solution. Note how the initial condition of $R_{Y0}/L = -2\cos\alpha_0/\sin^2\alpha_0$ from Gusakov, Irzak & Popov (2014) and Gusakov *et al.* (2017) strongly depends on the launch angle α_0: it defines a beam that is closer to a launch at the waist ($R_{Y0}/L = \infty$) for small incident angles, but becomes strongly focusing (smaller, negative R_{Y0}) for larger α_0.
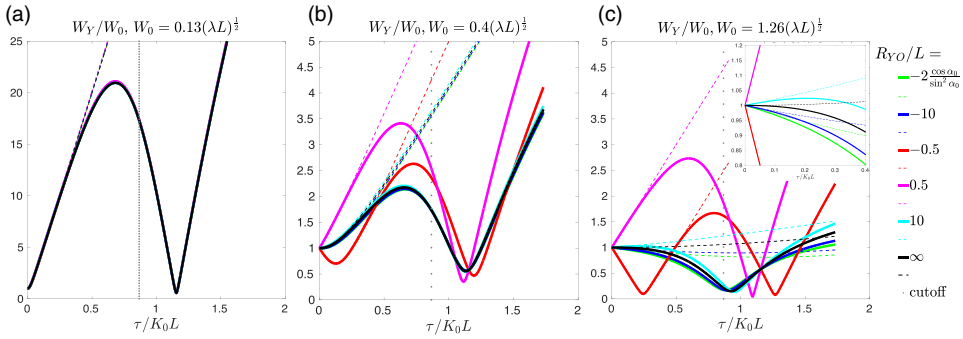
FIGURE 4. Similar to figure 3 for varying initial width $W_0/(\lambda L)^{\frac{1}{2}} = 0.13, 0.40, 1.26$ and fixed $\alpha_0 = 30°$. For small W_0, the beam is initially strongly focused and experiences a large expansion (due to diffraction) that follows the vacuum solution before focusing slightly past the turning point (for all of R_{Y0}). For increasing W_0, the initial growth is less severe and the beam focusing depends on the initial R_{Y0}. The beam even focuses twice along the path for particular initial conditions $R_{Y0}/L = -0.5, \alpha_0 = 30°, W_0/(\lambda L)^{\frac{1}{2}} = 0.4$ (red in panel *b*), and $1.26(\lambda L)^{\frac{1}{2}}$ (for the same $R_{Y0}/L, \alpha_0$, red in panel *c*), where the first focusing region is the waist captured by the vacuum solution. Varying the initial width W_0 affects the initial expansion of the beam, from a pronounced initial expansion in panel (*a,b*) to no initial expansion for some R_{Y0}/L in panel (*c*). The inset in panel (*c*) focuses on the initial propagation region, which exhibits converging or diverging beams depending on the initial conditions.

Figure 4 shows the beam width for different initial conditions $W_0/(\lambda L)^{\frac{1}{2}} = 0.13, 0.4, 1.26$, and the same scan in R_{Y0}/L as in figure 3, all while keeping a fixed initial incident angle $\alpha_0 = 30°$. For small $W_0 = 0.13(\lambda L)^{\frac{1}{2}}$, the beam width W_Y initially follows closely the vacuum solution (dashed line), independent of the initial conditions W_0 and R_{Y0}. Small $W_0/(\lambda L)^{\frac{1}{2}}$ corresponds to a highly focused beam. Diffraction produces a strong initial expansion of the beam width W_Y, which is followed by strong focusing slightly past the turning point (for all of R_{Y0}). For $W_0 = 0.40(\lambda L)^{\frac{1}{2}}$, the initial growth is less severe and the beam focusing (value and location) exhibits a noticeable dependence on the initial R_{Y0}. The dependence on the initial R_{Y0} is even more noticeable for $W_0 = 1.26(\lambda L)^{\frac{1}{2}}$, especially for the focus location: the beam even focuses twice along the beam for $R_{Y0}/L = -0.5$ (red curve), which is an initially focusing beam at the plasma edge (the first focusing region is the waist captured by the vacuum solution). The double focusing happens for both $W_0 = 0.4(\lambda L)^{\frac{1}{2}}$ and $W_0 = 1.26(\lambda L)^{\frac{1}{2}}$. Comparing the same initial condition $R_{Y0} = \infty$ (launch at waist, black curve) between the different initial W_0, we see that the beam focusing location takes place after the turning point for small initial $W_0 = 0.13, 0.40(\lambda L)^{\frac{1}{2}}$ and approaches the turning point for large $W_0 = 1.26(\lambda L)^{\frac{1}{2}}$ (the turning point location is given by the vertical dotted lines). This discussion has important consequences for interpreting the regions in the plasma with predominant contributions to backscattering in DBS measurements, as will be discussed in § 4.

In this section, we have seen how the 2-D linear-layer model exhibits focusing of the beam width around the cutoff. This focusing is separate from the focusing caused at the beam waist in vacuum. The beam focusing depends on the initial conditions

for the incident angle α_0, normalised beam parameter $W_0/(\lambda L)^{\frac{1}{2}}$ and radius of curvature R_{Y0}/L. Beam focusing tends to be enhanced for small α_0, while it tends to disappear for large α_0. For small $W_0/(\lambda L)^{\frac{1}{2}}$, strong initial growth precedes strong focusing. For large $W_0/(\lambda L)^{\frac{1}{2}}$, the beam focuses from the initial condition towards the focusing region, and the initial growth disappears for some initial conditions. These phenomena are not captured by the vacuum solution.

Having gained an understanding of the phenomenon of beam focusing, in what follows, we will use the analytical 2-D model solution to assess the impact of beam focusing on Doppler backscattering measurements.

3. Beam-tracing model for DBS in the 2-D linear layer

In the previous section, we have shown the behaviour of the width W_Y of a microwave beam propagating in a 2-D linear layer. In this section, we will use that solution to find the backscattered signal amplitude and power in DBS measurements. This will allow us to study how the phenomenon of beam focusing impacts the scattered power measured by DBS. We will see how the scattered power can be written as the integral over k-space of a filter function $|F_{xy}|^2$ multiplied by the Fourier transform of the turbulence correlation function, which corresponds to the density-fluctuation power spectrum. We will also see how the dependence of the filter function on k_x and k_y is not trivial, and we will show how $|F_{xy}|^2$ can be enhanced in the vicinity of the focusing region, where W_Y reaches a minimum. The formulae that we obtain using a beam-tracing model for DBS recover previous analytic work based on a 2-D Cartesian slab by Gusakov *et al.* (2014, 2017) and connect it with more recent work based on a beam-tracing model of DBS in full toroidal geometry (Hall-Chen *et al.* 2022b). To do so, we use a representation of the density fluctuations in 2-D Cartesian coordinates, as done by Gusakov *et al.* (2014, 2017). A representation aligned along the beam trajectory, or beam-aligned representation (Hall-Chen *et al.* 2022b), is not used in the main body of this manuscript. In Appendices C and D, we use the beam-aligned representation of the density to show the equivalence between the beam model by Hall-Chen *et al.* (2022b) and the 2-D DBS model by Gusakov *et al.* (2014, 2017). For the purposes of calculating the scattered power contributions along the beam path, we show in Appendices C and D that both representations of the density are related to each other by a rotation. With respect to the wavenumber resolution, the situation is more subtle and one cannot simply assume that both representations of the density are related by a rotation. This will be the subject of an upcoming publication.

We start by defining the Cartesian representation of the density fluctuations, or lab-frame density-fluctuation amplitude. We expand the density fluctuations in $\mathbf{r} = (x, y, z)$ as follows

$$\delta n(x, y, z, t) = \int \mathrm{d}k_x \mathrm{d}k_y \, \delta\hat{n}(k_x, k_y, z, t) \exp(ik_x x + ik_y y), \quad (3.1)$$

where x and y are the directions perpendicular to the magnetic field, and z is along the magnetic field (see figure 1 for the 2-D linear layer). In the 2-D linear layer, the density fluctuations in (3.1) are evaluated at $z = 0$. A point (x, y) in the 2-D plane is given by

$$\begin{aligned}
x &= x_c(\tau) + Y \sin\alpha(\tau), \\
y &= y_c(\tau) - Y \cos\alpha(\tau),
\end{aligned} \quad (3.2)$$

where $\big(x_c(\tau), y_c(\tau)\big)$ in (3.2) are the coordinates along the central ray (figure 1 and Appendix A), and α is the angle between the central ray tangent vector $\hat{\mathbf{g}}$ and the horizontal ($\sin\alpha$ and $\cos\alpha$ are given by (A.9)). The wavevector of the turbulence is written in its Cartesian components $\mathbf{k}_\perp = k_x\hat{\mathbf{x}} + k_y\hat{\mathbf{y}}$ (figure 1). Here, the Cartesian k_x naturally corresponds to the radial direction, or normal to the flux surface, and k_y corresponds to the binormal component, that is, the component in the flux surface and perpendicular to the magnetic field. This is a useful frame in which to express turbulent fluctuations perpendicular to the background magnetic field (Catto 1978; Frieman & Chen 1982).

Having introduced the representation of the density fluctuations, we calculate the backscattered amplitude and power. To do so, we use a theoretical beam-tracing model of DBS (Hall-Chen *et al.* 2022*b*) that gives an analytical relationship between the beam electric field and the scattered amplitude. As shown in Appendix B, the scattered amplitude takes an analogous form to (153) from Hall-Chen *et al.* (2022*b*),

$$A_r(t) = A_{ant} \int \mathrm{d}k_x \mathrm{d}k_y \, F_{xy,\mu}(k_x, k_y) \, \delta\hat{n}(k_x, k_y) \exp\left[i\big(2s_\mu + k_x x_{c\mu} + k_y y_{c\mu}\big)\right], \quad (3.3)$$

where $(x_{c\mu}, y_{c\mu}) = \big(x_c(\tau_\mu), y_c(\tau_\mu)\big)$ denote the point along the central ray trajectory evaluated at a particular $\tau = \tau_\mu$, and x_c and y_c are given by (2.9). The subscript $(.)_\mu$ means that functions are evaluated at a point along the trajectory $\tau = \tau_\mu$ that satisfies the Bragg condition for backscattering (3.4). In (3.3), the phase in the argument of the exponent is equivalent to the phase $2s_\mu + k_1 l_\mu$ of Hall-Chen *et al.* (2022*b*) (where k_1 is written as $k_{\perp,1}$), and it is ordered large $\sim L/\lambda$. The filter function $F_{xy,\mu}(k_x, k_y)$ is the Cartesian equivalent to $F_\mu(k_1, k_2)$ of Hall-Chen *et al.* (2022*b*). The expression for $F_{xy,\mu}$ is given in Appendix B. For the rest of the manuscript, we will only need the magnitude of $F_{xy,\mu}$, given in (3.8). Note that the expression for $A_r(t)$ is related to the spectral amplitude $\tilde{A}_r(\omega)$ by the Fourier transform $\mathscr{F}$ in time, $\tilde{A}_r(\omega) = \mathscr{F}\big[A_r(t)\big](\omega) = (2\pi)^{-1}\int A_r(t)\exp(i\omega t)\mathrm{d}t$ (only δn is assumed to depend on time). In this manuscript, we will preferentially work with $A_r(t)$.

As we announced above, the location τ_μ is defined by the condition of stationary phase (Bender & Orszag 1978), given to lowest order by

$$2K_\mu g_\mu + k_x \frac{\mathrm{d}x_c}{\mathrm{d}\tau}\bigg|_\mu + k_y \frac{\mathrm{d}y_c}{\mathrm{d}\tau}\bigg|_\mu = 0. \quad (3.4)$$

Equation (3.4) can be rewritten as $2K_\mu + \mathbf{k}_\perp \cdot \hat{\mathbf{g}}_\mu = 0$, where $\hat{\mathbf{g}} = \cos\alpha \, \hat{\mathbf{x}} + \sin\alpha \, \hat{\mathbf{y}}$ from (2.6). The components $\cos\alpha$ and $\sin\alpha$ can be calculated explicitly using the ray trajectory from (2.9), and the fact that $\cos\alpha = \mathrm{d}x_c/\mathrm{d}l$, $\sin\alpha = \mathrm{d}y_c/\mathrm{d}l$ and the element of path length is $\mathrm{d}l = g\mathrm{d}\tau$, which recovers (A.9). It will be useful to introduce the projections of the turbulence wavevector $\mathbf{k}_\perp$ along $\hat{\mathbf{g}}$ and $\hat{\mathbf{Y}}$,

$$\begin{aligned}
\mathbf{k}_\perp \cdot \hat{\mathbf{g}} &= k_x \cos\alpha + k_y \sin\alpha, \\
\mathbf{k}_\perp \cdot \hat{\mathbf{Y}} &= -k_y \cos\alpha + k_x \sin\alpha,
\end{aligned} \quad (3.5)$$

which defines a rotation in the 2-D (x, y) plane for every point along the beam path denoted by τ (note that α depends on τ through the trajectory in (2.9)).

To solve (3.4), we notice that $k_y + 2K_0 \sin \alpha_0 \sim 1/W \ll 1/\lambda$ (see Appendix B). The equation for τ_μ is then

$$K_x(\tau_\mu) \approx -\frac{k_x}{2} + \sin \alpha_0 (k_y + 2K_0 \sin \alpha_0) \frac{K_0}{k_x} \approx -\frac{k_x}{2}. \tag{3.6}$$

Note that (3.6) defines a τ_μ that fails near the turning point $k_x \approx 0$, but this divergence will not cause problems. More details are given in Appendix B.

From (3.3), we calculate the scattered power, which takes an analogous form to (177) of Hall-Chen *et al.* (2022*b*),

$$\frac{p_r}{P_{ant}} = \int dk_x dk_y |F_{xy,\mu}|^2 \langle |\delta \hat{n}(k_x, k_y)|^2 \rangle_T, \tag{3.7}$$

where the slowly varying filter $|F_{xy,\mu}|^2(k_x, k_y)$ is

$$|F_{xy,\mu}|^2(k_x, k_y) = 2\pi \frac{e^4}{m_e^2 \epsilon_0^2 \Omega^4} \frac{\Im[\Psi_{YY}]_\mu}{|\Psi_{YY}|_\mu} \frac{\exp\left[-\frac{\left(2\frac{dK}{d\tau}\right)_\mu^2 g_\mu^2}{\left|2\frac{dK}{d\tau}g - \frac{2K^2}{\Psi_{YY}}\left(\frac{d\alpha}{d\tau}\right)^2\right|_\mu^2} - \frac{2\left(\mathbf{k}_\perp \cdot \hat{\mathbf{Y}}_\mu\right)^2}{\Delta k_{\mu 2}^2} \right]}{\left|2\frac{dK}{d\tau}g - \frac{2K^2}{\Psi_{YY}}\left(\frac{d\alpha}{d\tau}\right)^2\right|_\mu}. \tag{3.8}$$

Here, m_e is the electron mass, e the electron charge, ϵ_0 is the vacuum permittivity and $\langle . \rangle_T$ is an ensemble average, which we compute as a time average over a period of length T. The Gaussian exponential term in $\mathbf{k}_\perp \cdot \hat{\mathbf{Y}}$ in (3.7), entering through $|F_{xy,\mu}|^2$ in (3.8), is to be considered as a Gaussian exponential in k_y, where $\mathbf{k}_\perp \cdot \hat{\mathbf{Y}}$ is defined in terms of k_x and k_y by (3.5). Note that all functions of τ in (3.8) are evaluated at $\tau = \tau_\mu$. Here, $\alpha_\mu = \alpha(\tau_\mu)$ is the vertical incidence angle at $\tau = \tau_\mu$, figure 1. The functions of τ_μ in $|F_{xy,\mu}(k_x, k_y)|^2$ in (3.8) are functions of (k_x, k_y) through the Bragg condition relating τ_μ to k_x and k_y ((3.4), (3.6)).

In (3.8), we have introduced the wavenumber resolution, given by $\Delta k_{\mu 2}^2 = 4|\Psi_{YY\mu}|^2/\Im[\Psi_{YY\mu}]$ (Hall-Chen *et al.* 2022*b*). In the context of the 2-D linear layer, the quantity $\Delta k_{\mu 2}$ is a measure of the resolution in the wavenumber component that is perpendicular to $\hat{\mathbf{g}}$. This is because $\mathbf{k}_\perp \cdot \hat{\mathbf{Y}}_\mu$ is the component of $\mathbf{k}_\perp$ in the perpendicular direction to $\hat{\mathbf{g}}$ (see (3.5)). The dependence of (3.8) on $\mathbf{k}_\perp \cdot \hat{\mathbf{Y}}_\mu$ therefore implies $\mathbf{k}_\perp \cdot \hat{\mathbf{Y}}_\mu \sim 1/W$, that is, $k_x \approx k_y \cos \alpha_\mu / \sin \alpha_\mu$, because $\Delta k_{\mu 2} \sim 1/W \ll 1/\lambda$. The resolution $\Delta k_{\mu 2}$ is of limited interest in this manuscript, beyond the fact that it is of order $\sim 1/W$.

The Gaussian exponential term in k_y from (3.8) allows us to calculate the wavenumber resolution in the lab frame, or DBS k_y-resolution Δk_y (see Appendix B). The final expression for the scattered power, expressed in terms of k_x and k_y, is

$$\begin{aligned}
\frac{p_r}{P_{ant}} &\approx 2^{\frac{1}{2}} \pi \frac{e^4}{m_e^2 \epsilon_0^2 \Omega^4} \frac{K_0^2 L}{\Delta k_y} \int dk_x dk_y \frac{\exp\left[-2(k_y + 2K_0 \sin \alpha_0)^2 / \Delta k_y^2\right]}{K_\mu W_{Y\mu}} \langle |\delta \hat{n}(k_x, k_y)|^2 \rangle_T \\
&\approx \pi^{\frac{3}{2}} K_0^2 L \frac{e^4}{m_e^2 \epsilon_0^2 \Omega^4} \int dk_x \frac{\langle |\delta \hat{n}(k_x, -2K_0 \sin \alpha_0)|^2 \rangle_T}{K_\mu W_{Y\mu}},
\end{aligned} \tag{3.9}$$

where we have defined the k_y resolution of the DBS diagnostic as

$$\Delta k_y^2 = 4\frac{|\Psi_{yy0}|^2}{\Im[\Psi_{yy0}]}. \tag{3.10}$$

Equation (3.9) defines a one-dimensional filter $|F_{x\mu}|^2$, given by

$$|F_{x\mu}|^2 = \pi^{\frac{3}{2}} K_0^2 L \frac{e^4}{m_e^2 \epsilon_0^2 \Omega^4} \frac{1}{K_\mu W_{Y\mu}}, \tag{3.11}$$

where the product $K_\mu W_{Y\mu}$ is given by

$$K_\mu W_{Y\mu} = \frac{K_0}{\left(2\Im[\Psi_{yy0}]\right)^{\frac{1}{2}}} \left| -\frac{k_x}{K_0} \right.$$
$$\left. + \Psi'_{yy0}\left(-2\frac{\cos^2\alpha_0 - \sin^2\alpha_0}{\cos\alpha_0}\frac{k_x}{K_0} + 4\sin^2\alpha_0 - \frac{k_x^2}{K_0^2} \right) \right|. \tag{3.12}$$

In (3.12), we used the beam-tracing analytic solution for $W_Y = W_Y(\tau)$ ((2.10), Appendix A) as well as the expression for $K = K(\tau)$ in the 2-D linear-layer problem.

The first approximately equal sign in (3.9) recovers the expected Gaussian exponential dependence of the power with k_y. Note how the exponential term in (3.8) has explicit dependence on k_x and k_y through $\mathbf{k}_\perp \cdot \hat{\mathbf{Y}}_\mu$. In addition, there is an additional dependence on k_x and k_y that appears through τ_μ, given by (3.6). Equation (3.9) is the lowest-order contribution to the Gaussian exponential term in (3.8), and shows that the selected wavenumber k_y is given approximately by $k_y \approx -2K_0 \sin\alpha_0 \sim 1/\lambda$, and the correction to that is ordered $\sim 1/W$. This justifies the first approximately equal sign in (3.9). The second approximately equal sign in (3.9) can be justified by the separation of scales in the integral in k_y: on the one hand, the spectrum $\langle|\delta\hat{n}(k_x, k_y)|^2\rangle_T$ depends on $k_y \sim 1/\lambda$; on the other hand, the resolution in (3.10) scales as $\Delta k_y \sim 1/W$, which means that the exponential term in (3.9) scales as $\sim \exp[-W^2/\lambda^2]$ if one assumes that $k_y + 2K_0\sin\alpha_0 \sim 1/\lambda$. The integral in k_y can therefore be calculated via Laplace's method, which results in the second approximately equal sign in (3.9). More details can be found in Appendix B.

Importantly, (3.9), (3.10) and (3.12) recover (16) of Gusakov *et al.* (2014), which was extended to (14) and (15) of Gusakov *et al.* (2017) for the cross-correlation function CCF. Gusakov *et al.* carry their analysis for radial correlation Doppler reflectometry (RCDR), and not for standard DBS, as done in this manuscript. In RCDR, one is interested in the cross-correlation function CCF(Δx), which depends on the radial separation Δx between DBS scattering locations. The scattered power calculated in this work can be recovered by setting $\Delta x = 0$ in the work by Gusakov *et al.* (2014, 2017) (power is auto correlation). Gusakov *et al.* (2014, 2017) also use a particular initial condition $\Psi'_{yy0} = iK_0L/(K_0\rho)^2$, where ρ is related to the launched beam width. One can see that setting the particular initial condition for $\Psi'_{yy0} = iK_0L/(K_0\rho)^2$ in (3.12) recovers (14) and (15) of Gusakov *et al.* (2017) for $\Delta x = 0$.

The backscattered power can be written as an integral along the path l ((196) of Hall-Chen *et al.* 2022*b*). This can be achieved by realising that the Bragg condition and the fact that $\mathbf{k}_\perp \cdot \hat{\mathbf{Y}} \approx 0$ imply $k_x \approx -2K_{x\mu}$ (3.5). Having integrated in k_y, the

scattered k_x along the Cartesian x-direction can parametrise the location along the path. To express the k_x-integral (3.9) in terms of l, change the integration variable using $\mathrm{d}k_x = 2K_\mu |\mathrm{d}K_\mu/\mathrm{d}\tau| \mathrm{d}l/|g_\mu K_{x\mu}| = 2\mathrm{d}l/(gL)$, where we used (B.25). Then, the denominator under the integral sign $\int \mathrm{d}k_x$ can be explicitly expressed as a function of the path length l. Additional details on the calculation are given in Appendices A and B. We find

$$\frac{p_r}{P_{ant}} \approx 4\pi^{\frac{3}{2}} \frac{e^4}{m_e^2 \epsilon_0^2 \Omega^4} \int \frac{\mathrm{d}l}{g^2 W_Y} \langle \left| \delta\hat{n}\left(k_x(l), -2K_0 \sin\alpha_0\right) \right|^2 \rangle_T. \qquad (3.13)$$

Equation (3.13) closely connects to the expression for the scattered power in (196) of Hall-Chen *et al.* (2022b). In that case, $1/g^2$ is the ray piece, while the beam piece can still be written as $1/W_Y$. We see that W_Y plays an explicit role in the k_x wavenumber resolution (see (3.9)) and equivalently in the spatial localisation of the power along the beam path (see (3.13)). Finally, (3.13) may seem to contradict our prediction that the scattered power scales as $\sim 1/g$. Note that in (3.13), one of the factors of g comes from the change of integration variable from k_x to l.

Next, we discuss the filter function $|F_{x\mu}|^2 \propto 1/K_\mu W_{Y\mu}$ in (3.11). Gusakov *et al.* (2014, 2017) argue that non-local forward-scattering events produced by large-radial-scale fluctuations cause the denominator of $|F_{xy,\mu}|^2$ to approach zero. This happens for specific k_x and should cause an enhancement in the DBS signal. Gusakov *et al.* (2014, 2017) state that this enhancement is due to forward-scattering events taking place all along the beam path through the plasma, making the DBS measurement spatially non-local. They argue that this effect should preferentially enhance the DBS signal for small incidence angles α_0, which they observe as an enhancement in the CCF. In our work, forward scattering is absent by design. Our model only includes contributions from backscattering events, which are selected through the Bragg condition in (3.4) and (3.6). Equation (3.9) shows that all the contributions to the so-called forward scattering can be explained by the filter function, which is the term $\propto 1/K W_Y$ in (3.9), or equivalently $\propto 1/g^2 W_Y$ when written as an integral in l. Importantly, in §4, we will see how the focusing effect due to W_Y can be far greater than the decrease of K near the turning point. It is therefore crucial to understand the behaviour of W_Y to understand its effect on the backscattered signal. In this work, we interpret (3.9) and the signal enhancement produced for specific k_x as a consequence of beam focusing in the vicinity of a turning point, and not as due to forward scattering. The more the beam is focused (small W_Y), the more the signal is localised around the focusing region due to the local increase in the wave intensity, which takes place at a finite k_x (in the vicinity of, but not exactly at the turning point). This effect preferentially happens for small incident angles α_0, as was shown in §2. The fact that the width W_Y does not focus exactly at the turning point (see figures 3 and 4) results in the filter function peaking at a finite k_x (recall that $k_x = 0$ corresponds to the turning point location).

With respect to the wavenumber resolution, (3.9) recovers previous calculations of the DBS wavenumber resolution (Lin *et al.* 2001; Hirsch *et al.* 2001; Hillesheim *et al.* 2012), which is derived here in the context of a beam-tracing model. Note the difference between Δk_y in the lab frame, which is constant along the path in the particular case of the 2-D linear layer, and $\Delta k_{\mu 2}$ of Hall-Chen *et al.* (2022b), which is perpendicular to the central ray propagation and depends strongly on the distance along the path. Equation (3.10) simplifies to $\Delta k_y = 2/\rho$ for the choice of Ψ_{yy0} made by Gusakov *et al.* (2014, 2017). Note how the value $2/\rho$ is a lower limit to

the diagnostic k_y-wavenumber resolution. Interestingly, the wavenumber resolution Δk_y depends on the incidence angle α_0 for a given initial W_0, R_{Y0} and a given L. Inspecting (3.10) and using the expression for Ψ_{yy0} in terms of W_0 and R_{Y0} (Appendix A), we find that

$$\Delta k_y^2 = 2\cos^2\alpha_0 \frac{K_0^2 W_0^2}{K_0 L} \left[\left(\frac{L}{R_{Y0}} + \frac{\sin^2\alpha_0}{2\cos\alpha_0} \right)^2 + 4 \left(\frac{K_0 L}{K_0^2 W_0^2} \right)^2 \right] \frac{K_0}{L}. \qquad (3.14)$$

Equation (3.14) shows how Δk_y can have a non-trivial dependence on α_0, which should be taken into consideration when comparing the scattered power in DBS measurements and in numerical turbulence simulations via synthetic diagnostics.

Equations (3.9), (3.10) and (3.12) are the bases for synthetic DBS diagnostics that can be readily applied to direct nonlinear gyrokinetic simulations of plasma turbulence. In that context, and borrowing notation from previous work (Ruiz *et al.* 2022), k_x and k_y can be directly identified to the physical normal and binormal wavenumbers k_n and k_b. The Cartesian k_x employed here corresponds to the normal wavenumber component of the gyrokinetic simulation $k_x = k_n = \mathbf{k}_\perp \cdot \hat{\mathbf{e}}_n$, where $\hat{\mathbf{e}}_n = \nabla r/|\nabla r|$ is the unit vector normal to the flux surface identified by minor radius r. The Cartesian k_y corresponds to the binormal wavenumber of gyrokinetic simulations $k_y = k_b = \mathbf{k}_\perp \cdot \hat{\mathbf{e}}_b$, where $\hat{\mathbf{e}}_b = \hat{\mathbf{e}}_n \times \hat{\mathbf{b}}$ is the binormal wavevector, perpendicular to the unit vector of the magnetic field $\hat{\mathbf{b}}$ and to $\hat{\mathbf{e}}_n$. Depending on the gyrokinetic code used, k_n and k_b might need to be mapped from internal code wavenumber definitions, examples of which are given by Ruiz *et al.* (2022).

4. Consequences of beam focusing for DBS measurements

The phenomenon of beam focusing affects the DBS signal localisation and wavenumber resolution, and it enhances the DBS signal in the vicinity of the beam focusing region, as shown by the filter function $|F_{x\mu}|^2 \propto 1/K_\mu W_{Y\mu}$ for the 2-D linear-layer problem in (3.11). This challenges the interpretation of 'forward scattering' provided by Gusakov & Surkov (2004), Gusakov *et al.* (2014) and Gusakov *et al.* (2017) as the responsible mechanism for the DBS signal enhancement for decreasing launch angle α_0. In this section, we characterise the consequences of beam focusing on the DBS signal through the filter function $|F_{x\mu}|^2$ for the 2-D linear-layer problem. We scan the possible initial conditions: incident angle α_0, initial width W_0 and initial radius of curvature R_{Y0}. In what follows, K_μ and $W_{Y\mu}$ are normalised to the initial conditions K_0 and W_0, respectively.

4.1. *The 1-D filter function* $|F_{x\mu}|^2$

The filter function $|F_{x\mu}|^2$ in (3.11) provides the k_x-selectivity of the DBS power. This is tied to the localisation along the path: the scattering turbulent k_x can be thought of as a parameter determining the location of scattering along the path τ_μ, as τ_μ is related to the turbulent scattering k_x via the Bragg condition for backscattering in (3.6), which is used to arrive at (3.13). The radial component $K_{x\mu} = K_0(\cos\alpha_0 - \tau_\mu')$ from (2.9) is a decreasing function of τ_μ' from the launch, becoming negative after the turning point ($K_{x\mu} = 0$, i.e. $\tau_\mu' = \cos\alpha_0$). The vertical component K_y is constant, since the system is homogeneous in y. This means that K_μ reaches its minimum at the turning point, which should enhance the DBS signal contribution at that location. As we saw in the previous section, the perpendicular beam width
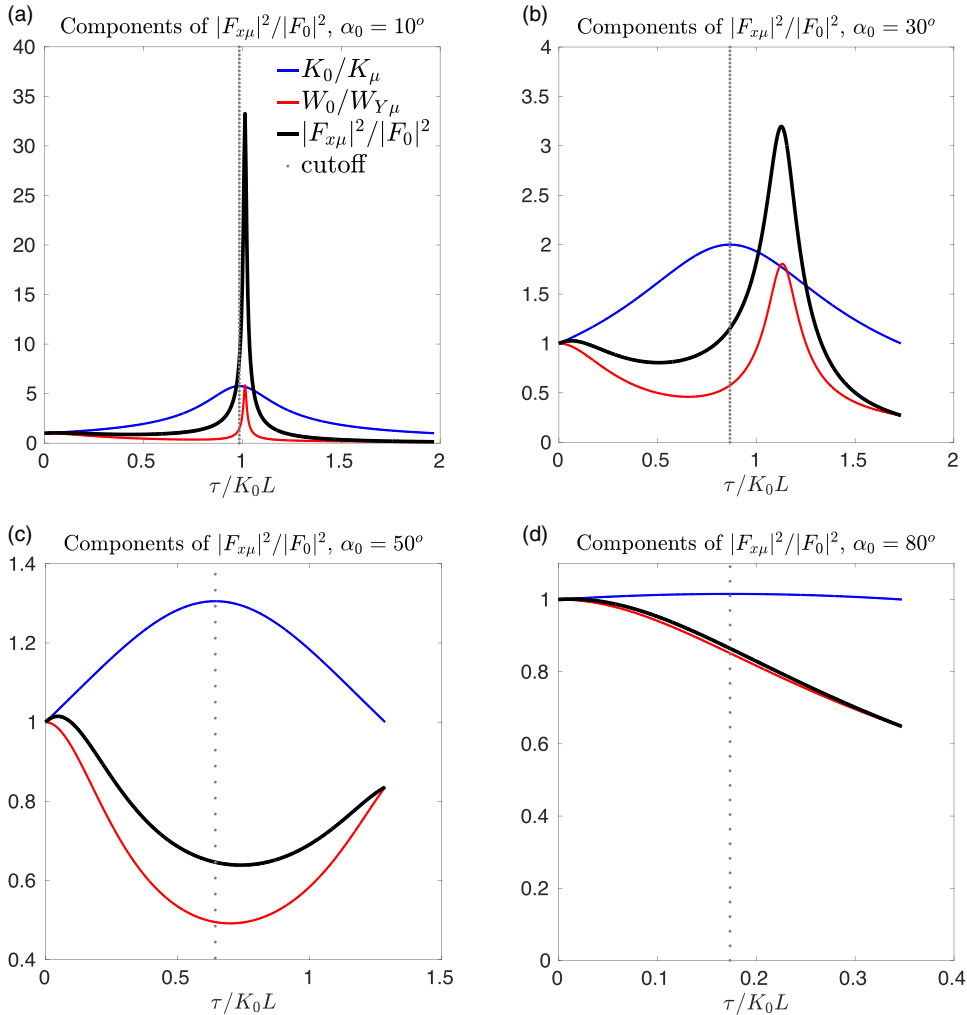
FIGURE 5. Filter function $|F_{x\mu}|^2(\tau)/|F_0|^2 = K_0 W_0 / K_\mu W_{Y\mu}$ and the corresponding ray component K_0/K_μ and beam component $W_0/W_{Y\mu}$ for varying values of the incident launch angle α_0, and fixed $R_{Y0} = \infty$ and $W_0 = 0.40(\lambda L)^{\frac{1}{2}}$. Note that in all cases, the filter function is predominantly affected by the beam term $1/W_{Y\mu}$ which represents the focusing.

$W_{Y\mu}$ has a tendency to focus, which should further enhance the DBS signal power. In this section, we separate the enhancement due to ray and the beam contributions in the filter function.

Figure 5 shows the ray (blue) and beam (red) components of $|F_{x\mu}|^2$ for varying incident angles $\alpha_0 = 10°$, $30°$, $50°$ and $80°$, and fixed $W_0 = 0.40(\lambda L)^{\frac{1}{2}}$ and $R_{Y0} = \infty$ (launch at the waist). For convenience, we normalise the filter function to its value at $\tau = 0$, $|F_0|^2$. The filter functions correspond to some of the beam solutions in figure 3. For $\alpha_0 = 10°$, the filter function $|F_{x\mu}|^2$ is strongly localised at the focus location, which almost matches the location of the turning point, or cutoff (maximum of the ray term in blue). The turning point, or cutoff, is represented in each figure by
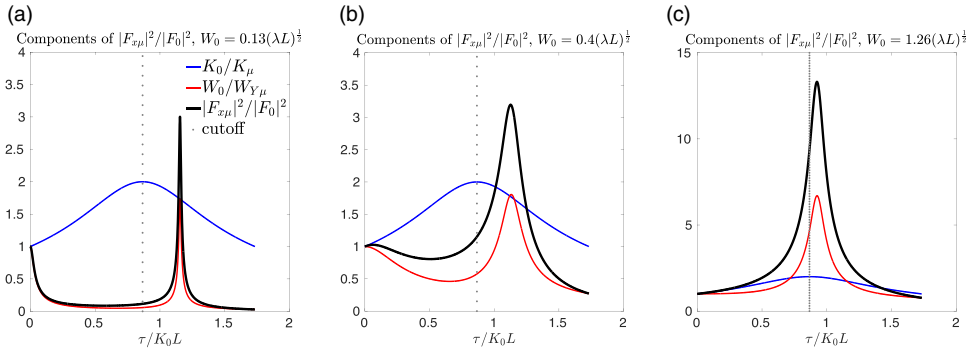
FIGURE 6. Filter function $|F_{x\mu}|^2(\tau)/|F_0|^2 = K_0 W_0/K_\mu W_{Y\mu}$ and the corresponding ray component K_0/K_μ and beam component $W_0/W_{Y\mu}$ for varying values of the initial width $W_0 = 0.13, 0.40, 1.26(\lambda L)^{\frac{1}{2}}$, and fixed $R_{Y0} = \infty$ and $\alpha_0 = 30°$. Note that in all cases, the filter function is predominantly affected by the beam term $1/W_{Y\mu}$ which represents the focusing.

a vertical grey dotted line. Careful inspection shows that the focus location takes place in the vicinity but after the turning point $\tau'_\mu = \cos\alpha_0$ for $\alpha_0 = 10°$, consistent with beam focusing taking place after the turning point in figure 3. This shows that the contributions to the DBS power are predominantly from the vicinity (but after) the turning point for these initial conditions.

For larger incident angles, the turning point takes place for smaller $\tau'_\mu = \cos\alpha_0$, while the beam term peaks at larger τ'_μ (beam focus takes place at larger τ'_μ): the ray and beam terms compete to yield a filter function that is less peaked and less localised around the focus location for increasing α_0. The ray term (blue) decreases in amplitude for larger α_0, but less than the beam term (red), which decreases more. The beam term becomes broader in τ'_μ for larger angles. These effects make the signal more delocalised along the path. This can be clearly seen in figure 5(*c*). The localisation becomes broad for $\alpha_0 = 50°$, where beam focusing becomes less important in favour of contributions from $\tau'_\mu = 0$. In figure 5, the initial condition is chosen to be at the waist $W_Y(\tau = 0) = W_0$. In figure 7, we show the effect of the initial radius of curvature R_{Y0} on the filter function. An initially expanding beam (positive and finite R_{Y0}/L) is shown in figure 7 not to make a dramatic difference on $|F_{x\mu}|^2$. For larger incident angles ($\alpha_0 = 80°$), the filter peaks around $\tau = 0$, corresponding to the waist initial condition of figure 5 (figure 7 shows that the behaviour is qualitatively similar for different initial R_{Y0}). Therefore, for large incident angles, the DBS signal becomes delocalised with predominant contributions before and after the turning point (figures 5 and 7).

Figure 6 shows the ray (blue) and beam (red) components of $|F_{x\mu}|^2$ for different values of the initial width $W_0/(\lambda L)^{\frac{1}{2}} = 0.13$, 0.40 and 1.26, and fixed incident angle $\alpha_0 = 30°$ and $R_{Y0} = \infty$ (launch at the waist). The filter functions in figure 6 correspond to some of the beam solutions in figure 4. In this case, the ray term remains constant. The beam term is narrowest around the initial launch (waist) and around the focusing point for small initial width $W_0 = 0.13(\lambda L)^{\frac{1}{2}}$. This is because a small initial width produces rapid expansion of the beam (see figure 4), which gives negligible contributions to the beam term outside the waist and focus point. This suggests a very localised contribution to the DBS power from the vicinity of
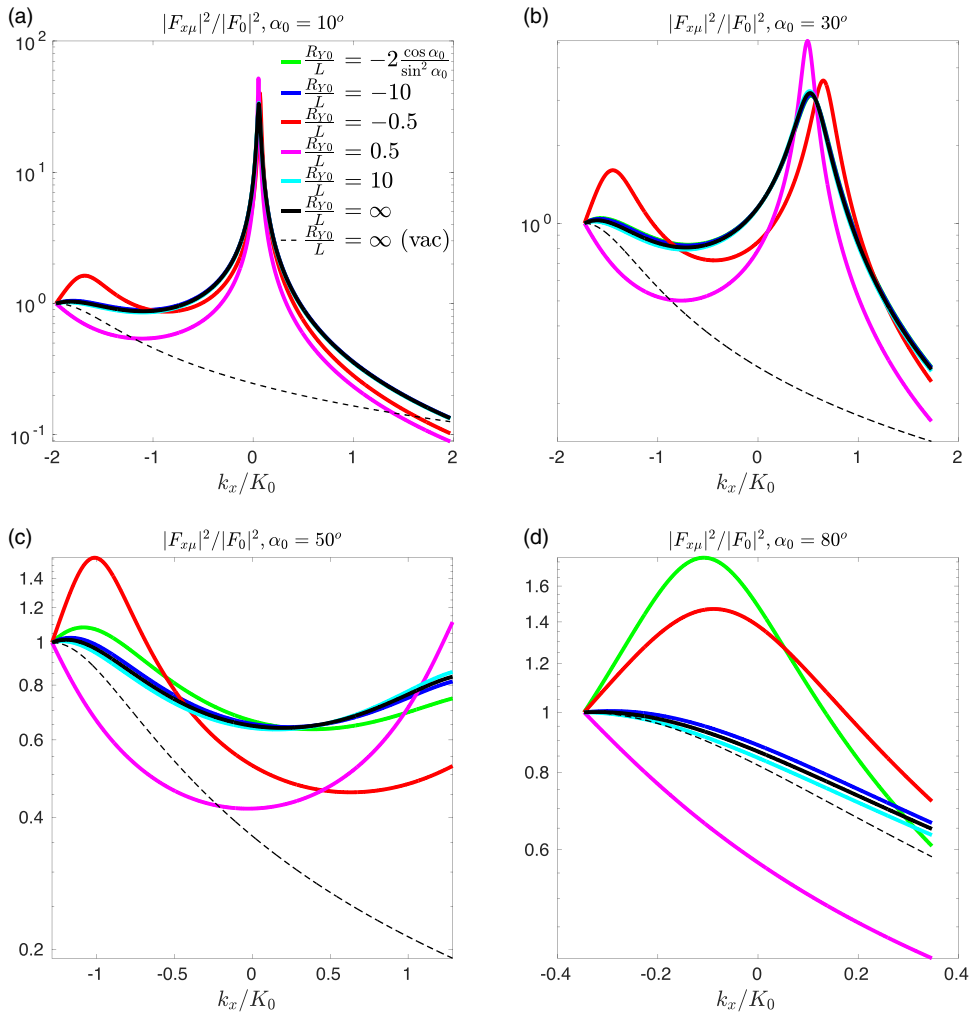
FIGURE 7. Values of the filter function $|F_{x\mu}|^2/|F_0|^2$ for varying incident angles α_0 and fixed initial $W_0 = 0.40(\lambda L)^{\frac{1}{2}}$ as a function of the turbulent, selected k_x component. For small incident angle $\alpha_0 = 10°$, the filter is strongly peaked near $k_x = 0$, consistent with the signal being strongly localised near the turning point region. The signal is in fact sensitive to slightly positive $k_x > 0$, which corresponds to a focusing slightly after the turning point. For $\alpha_0 = 30°$, the peak near $k_x = 0$ decreases and shifts to larger k_x values, meaning that the signal starts getting important contributions from finite k_x turbulent fluctuations away from the turning point. For $\alpha_0 = 50°$, the peak has almost disappeared and the signal receives close-to-uniform contributions in the range of $-1 \lesssim k_x/K_0 \lesssim 2$, corresponding to a highly delocalised signal along the beam path. For $\alpha_0 = 80°$, the beam expands for most of its path and the filter function approaches the vacuum solution.

the focus point as well as the plasma edge (if enough fluctuations are present). For initial width $W_0 = 0.40(\lambda L)^{\frac{1}{2}}$, the location of the peak in $|F_{x\mu}|^2$ is similar to that for $W_0 = 0.13(\lambda L)^{\frac{1}{2}}$, but the filter function becomes broader, suggesting that the beam focusing is slower and takes place over a larger region, as shown in figure 4. For

$W_0 = 1.26(\lambda L)^{\frac{1}{2}}$, the filter function maximum has increased in value (beam focuses more) and has a peak as broad as the filter function for $W_0 = 0.4(\lambda L)^{\frac{1}{2}}$. Interestingly, in this case, the filter function $|F_{x\mu}|^2$ does not exhibit an initial decrease after the launch. This is because, in this condition, the beam does not initially expand following the launch, but only contracts from launch to the focus location (see black line in figure 4c). Moreover, the beam focuses closer to the turning point than for $W_0/(\lambda L)^{\frac{1}{2}} = 0.13, 0.4$.

Figures 3–7 show that the beam focusing in W_Y tends to take place close to but after the turning point ($K_{x\mu} = 0$, $\tau'_\mu = \cos \alpha_0$) depending on the initial conditions for the incident angle α_0, width $W_0/(\lambda L)^{\frac{1}{2}}$ and especially on the phase front radius of curvature R_{Y0}. This challenges the common belief that the DBS signal is always most sensitive at the turning point and has important consequences for interpreting the DBS scattered power.

It is equally instructive to characterise the filter function in terms of the turbulent scattered k_x. Note that negative k_x corresponds to scattering from the beam in its first pass from launch towards the turning point, and positive k_x to scattering from the beam in its return journey away from the turning point. Figure 7 shows the variation of the filter function $|F_{x\mu}|^2$ for different incident angles α_0, different initial radii of curvature R_{Y0} and $W_0 = 0.40(\lambda L)^{\frac{1}{2}}$ as a function of the turbulent scattered k_x. For $\alpha_0 = 10°$, $|F_{x\mu}|^2$ is strongly peaked at $k_x = 0$. This means that the DBS signal is strongly localised near the turning point region and predominantly sensitive to fluctuations with $k_x \approx 0$. For $\alpha_0 = 30°$, the filter peak shifts towards larger k_x. For even larger $\alpha_0 = 50°$, the filter is sensitive almost uniformly to $-1 \lesssim k_x/K_0 \lesssim 2$, with peaks of the filter function at both positive and negative k_x, and surprisingly a dip in the vicinity of $k_x = 0$. This suggests that the DBS power is sensitive predominantly to specific values of k_x, with a subdominant contribution from $k_x = 0$. For $\alpha_0 = 80°$, the beam follows closely vacuum propagation and the filter has contributions from small k_x/K_0 near 0, but this time originating near $\tau = 0$ (near the vacuum beamwaist, or edge of the plasma in a real experiment) and decays for larger k_x. The beam expands for most of its path and the filter function approaches the vacuum solution (black dashed line).

Figure 8 shows the corresponding filter function for varying $W_0/(\lambda L)^{\frac{1}{2}} = 0.13, 0.40$ and 1.26, different radii of curvature and fixed initial angle $\alpha_0 = 30°$. The behaviour of the filter function for small W_0 can be understood from figure 4. For small initial W_0, the filter is strongly peaked at two different values of k_x and is independent of the initial condition R_{Y0}, consistent with the signal being strongly localised at the plasma entrance and near the turning point region. For $W_0 = 0.40(\lambda L)^{\frac{1}{2}}$, the filter is dominated by a peak with amplitude and location similar to those of the peak due to focusing for small W_0, but broader, and hence the signal gets enhanced contributions from turbulent fluctuations away from the focusing region, depending on the initial condition R_{Y0}. For $W_0 = 1.26(\lambda L)^{\frac{1}{2}}$, the peak in k_x stays broad and shifts towards $k_x = 0$ for launch near the waist (large $|R_{Y0}/L|$). The small $|R_{Y0}/L|$ cases are different, exhibiting distinctive narrow peaks that even appear twice for $R_{Y0}/L = -0.5$, consistent with two consecutive focusing regions, as in figure 4.
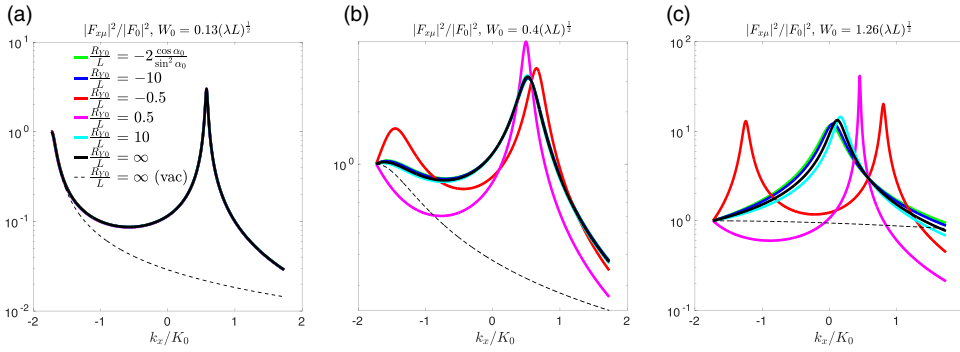
FIGURE 8. Values of the filter function $|F_{x\mu}|^2/|F_0|^2$ for varying initial width $W_0/(\lambda L)^{\frac{1}{2}} = 0.13, 0.40, 1.26$ and fixed $\alpha_0 = 30°$ as a function of the turbulent, selected k_x. For small initial W_0, the filter is strongly peaked at two values of k_x: one negative that corresponds to the entrance to the plasma, and one positive from the beam focusing. For small W_0, the filter is also independent of the initial condition R_{Y0}. For $W_0 = 0.40(\lambda L)^{\frac{1}{2}}$, the filter is dominated by a peak of amplitude and location similar to those of the peak due to focusing for small W_0, but broader. For $W_0 = 1.26(\lambda L)^{\frac{1}{2}}$, the peak in k_x stays broad and shifts towards $k_x = 0$ for launch near the waist (large $|R_{Y0}/L|$).

4.2. *Predictions of the measured turbulent spectra*

Throughout this manuscript, we have focused on describing the dependence of the filter function $|F_{x\mu}|^2$ on experimentally relevant initial values for α_0, W_0 and R_{Y0}. We should note, however, that the intrinsic power spectrum of the turbulence itself has a direct impact on the measurement. The turbulent spectrum is generally a decreasing function of k_x, as demonstrated by direct numerical gyrokinetic turbulence simulations. In conditions where the filter function predominantly selects large k_x (finite to large α_0), the turbulence spectrum in k_x should be taken into account to understand the dominant k_x contributing to the backscattering signal. In this section, we apply what we have learned about the filter function $|F_{x\mu}|^2$ in the beam-tracing model and use it to understand its effect on the DBS backscattered power from a realistic density-fluctuation spectrum.

We use the electron-density-fluctuation wavenumber power spectrum $\langle|\delta\hat{n}(k_x, k_y)|^2\rangle_T$ obtained from nonlinear gyrokinetic simulations resolving strongly developed ETG turbulence in NSTX, which was examined by Ruiz *et al.* (2015, 2019, 2020*a,b*); Ren *et al.* (2020); Ruiz *et al.* (2022); Guttenfelder *et al.* (2022). The turbulent spectrum can be approximated by the following shape:

$$\frac{\langle|\delta\hat{n}(k_x, k_y)|^2\rangle_T}{n^2} \sim \frac{A}{1 + \left|\frac{k_x}{w_{k_x}}\right|^{\zeta} + \left|\frac{k_y - k_{y*}}{w_{k_y}}\right|^{\eta}}. \tag{4.1}$$

This expression is fitted to the specific strongly driven ETG simulations that we have mentioned above (Ruiz *et al.* 2022) to find: $\zeta \approx 3.14$, $\eta \approx 3.19$, $w_{k_x}\rho_s \approx 0.89$, $w_{k_y}\rho_s \approx 4.09$, $k_{y*}\rho_s \approx 6.53$, $A \approx 1.18 \ 10^{-6}$ (here ρ_s is evaluated at the cutoff of the hypothetical DBS experiment). Ruiz *et al.* (2022) represented the fluctuation spectra in terms of the normal and binormal wavenumber components k_n and k_b perpendicular to the magnetic field, which can be easily calculated from the internal wavenumber
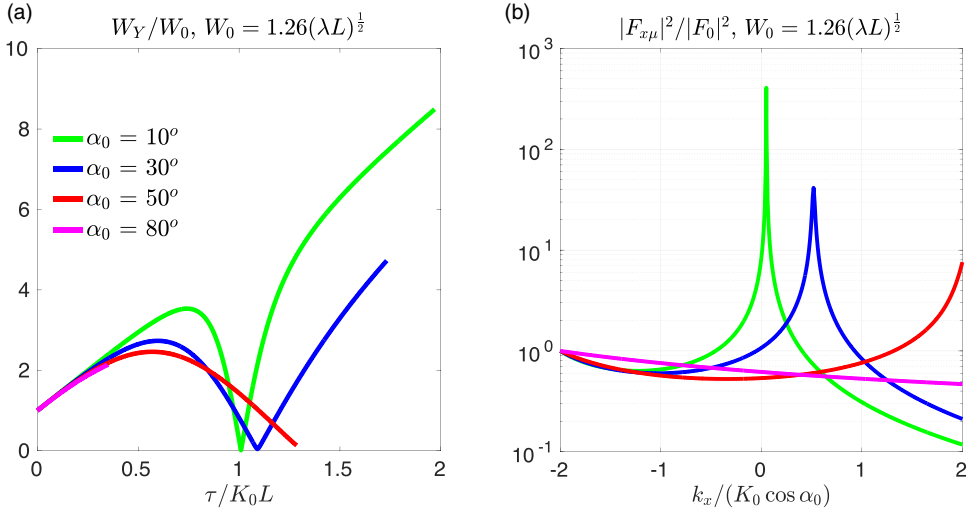
FIGURE 9. (*a*) Values of the normalised beam width W_Y/W_0 along the path τ for varying values of the incident angle α_0, $W_0 \approx 1.26(\lambda L)^{\frac{1}{2}}$ and $R_{Y0}/L = 0.5$. The curves are plotted for the values of τ in which the beam is traversing the plasma slab, $x > 0$. We assume vacuum for $x < 0$ and the beam is launched at $x = 0$. (*b*) Corresponding filter function $|F_{x\mu}|^2/|F_0|^2 = K_0 W_0/K_\mu W_{Y\mu}$ plotted as a function of the scattered turbulent k_x within the plasma slab, that is, for $|k_x/K_0 \cos \alpha_0| < 2$.

components in a gyrokinetic code. The normal and binormal components correspond to the Cartesian k_x and k_y employed throughout this manuscript, as we have explained at the end of § 3. Importantly, from here on, we assume that the turbulent spectrum is uniform in space, that is, the parameters A, ζ, η, w_{k_x}, w_{k_y} and k_{y*} are assumed to be constant throughout the whole plasma volume through which the beam propagates.

DBS experiments routinely vary the angle of incidence α_0 to select different wavenumbers from the turbulence spectrum. In what follows, we show how the beam width W_Y, the filter function $|F_{x\mu}|^2$ and ultimately the measured turbulence spectrum are impacted by varying α_0.

Figure 9(*a*) shows the normalised beam width W_Y/W_0 from the beam-tracing equations as a function of τ for a range of incident angles $\alpha_0 = (10°, 30°, 50°, 80°)$, $W_0 = 1.26(\lambda L)^{\frac{1}{2}}$ and $R_{Y0}/L = 0.5$. The beams in figure 9 have the same initial frequency Ω and reach a turning point location at $x = L_n = L \cos^2 \alpha_0$ (see figure 1). Figure 9(*a*) exhibits beam focusing for $\alpha_0 = 10°$, $30°$ within the plasma while the beam focusing takes place outside the plasma for $\alpha_0 = 50°$. Both the value of the minimum beam width and the focusing location increase with α_0 in this particular case.

Figure 9(*b*) shows the DBS filter function $|F_{x\mu}|^2$ corresponding to figure 9(*a*) plotted as a function of the turbulent scattered k_x normalised to $K_0 \cos \alpha_0$. The scattered k_x at every τ location is computed using the Bragg condition for backscattering written in Cartesian coordinates, $k_x = -2K_{x\mu} = -2K_0(\cos \alpha_0 - \tau'_\mu)$ (see § 3 and Appendix B). The turning point takes place where $K_{x\mu} = 0$, i.e. $\tau'_\mu = \cos \alpha_0$.

Note how the filter function peaks closer to $k_x = 0$ for decreasing α_0, corresponding to the beam focusing location approaching the turning point for small angles. The intensity of the enhancement decreases for increasing α_0. The dominant k_x contributing to scattering is always positive $k_x > 0$ in this situation, which means that the signal is predominantly originating from plasma locations after the turning point. Note how this depends on the initial condition: figure 4(*c*) shows how the beam focusing can take place arbitrarily close to the turning point for the same $\alpha_0 = 30°$ and $W_0 = 1.26(\lambda L)^{\frac{1}{2}}$ values but different R_{Y0}. Increasing values of α_0 will move the filter function localisation of the DBS signal further and further away from the turning point, reaching the plasma exit for $\alpha_0 \approx 50°$ in these conditions (see red line in figures 9*a* and 9*b*).

Next, we quantify the combined effect of the filter function and its dependence on k_x, in conjunction with a realistic, power-law turbulence spectrum. In figures 10 and 11, we normalise k_x, k_y and the initial wavenumber magnitude K_0 to the local ion sound gyroradius at the cutoff $\rho_s = c_s/\Omega_D$, where $c_s = (T_e/m_D)^{1/2}$ is the local ion sound speed, m_D the deuterium mass and $\Omega_D = eB/m_D$ is the deuterium gyro-frequency. Using the relation $\Omega = \omega_{pe0}/\cos\alpha_0$ between Ω and the local value of the electron plasma frequency at the cutoff ω_{pe0} (see §2.3), we have $K_0\rho_s = (\beta_e m_D/2m_e)^{1/2}/\cos\alpha_0 \approx 4.26/\cos\alpha_0$, where $\beta_e \approx 1\%$ is the electron beta using the local magnetic field, electron density and temperature of the NSTX experiment analysed by Ruiz *et al.* (2015, 2019, 2020*a,b*); Ren *et al.* (2020); Ruiz *et al.* (2022); Guttenfelder *et al.* (2022).

Figure 10 shows the radial-wavenumber dependence of the density-fluctuation power spectrum (blue lines) that would be sampled as the microwave beam propagates through the plasma. The product of the filter function $|F_{x\mu}|^2$ and the density-fluctuation power is shown in red. These quantities are plotted as a function of the turbulent k_x normalised by ρ_s using $k_x\rho_s = (k_x/K_0)(K_0\rho_s)$. The solid lines correspond to k_x scattered after the turning point ($k_x > 0$ in figure 9*b*), while the dashed lines correspond to k_x scattered before the turning point ($k_x < 0$ in figure 9*b*). As expected, the filter function has an important effect on the DBS signal power for smaller incidence angles $\alpha_0 = 10°, 30°$, while it becomes unimportant for larger α_0, at which point, the spectral falloff of the density spectrum becomes the dominant effect determining the k_x selection in the DBS measurement. Note, for example, that the peaking of the filter function near the plasma exit for $\alpha_0 = 50°$ becomes negligible because it occurs at large k_x. Importantly, figure 10 contains both information about the radial localisation of the DBS power (if plotted as a function of τ) as well as the k_x-selectivity of the power spectrum in the DBS measurement (plotted as a function of k_x) through the combined effect of the filter function and the turbulent spectrum. We stress again that, in this discussion, we are neglecting the spatial dependence of the turbulence intensity and spectrum, $\langle|\delta\hat{n}|^2\rangle_T$, which is assumed not to vary along the path.

Ultimately, one of the main purposes of DBS diagnostics as a turbulence measurement is to obtain the density-fluctuation power spectrum in the binormal wavenumber of the turbulence, known as $k_\perp$ in the DBS jargon. In the context of this manuscript, $k_\perp$ is k_y. To understand the impact of the filter function in such a measurement, in figure 11(*a*), we plot the integrated filter function $|F_{x\mu}|^2$ over the relevant k_x which would be sampled as the beam propagates through the plasma as a function of the selected wavenumber $k_y = 2K_0\sin\alpha_0$. Since $|F_{x\mu}|^2$ multiplies the density-fluctuation spectrum $\langle|\delta\hat{n}|^2\rangle_T$, a constant $\int dk_x\rho_s|F_{x\mu}|^2/|F_0|^2$ as a function
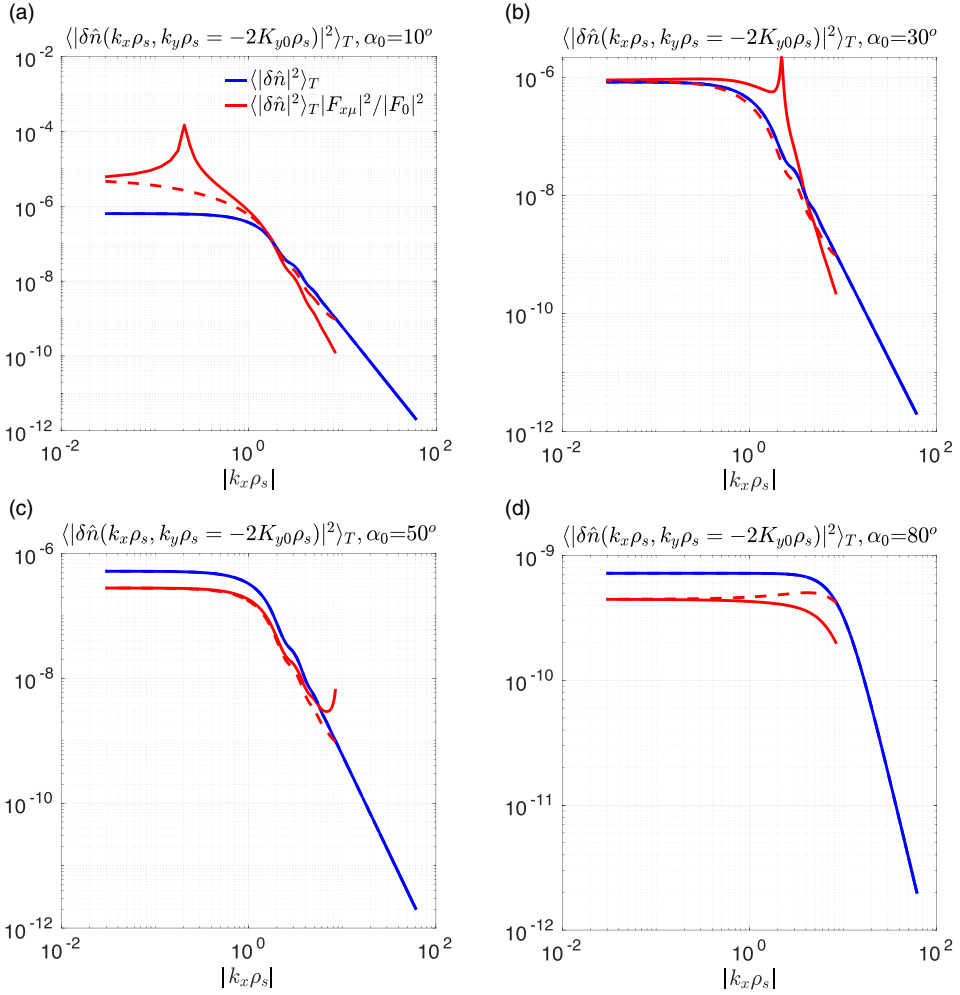
FIGURE 10. Density-fluctuation power $\langle|\delta\hat{n}|^2\rangle_T$ and the product of the density-fluctuation power and the filter function $\langle|\delta\hat{n}|^2\rangle_T|F_{x\mu}|^2/|F_0|^2$ as a function of the normalised scattered turbulent radial wavenumber $k_x\rho_s$ for different values of the scattered turbulence $k_{y0}\rho_s = -2K_0\rho_s \sin\alpha_0$. The different $\alpha_0 = (10°, 30°, 50°, 80°)$ correspond to scattered wavenumbers $k_{y0}\rho_s = -(1.50, 4.92, 10.15, 48.29)$. Solid lines correspond to $k_x > 0$, while dashed lines correspond to $k_x < 0$. The red curve shows that the beam focusing has a strong effect in the measurement k_x selection for $\alpha_0 \lesssim 30°-40°$, while the effect becomes negligible for $\alpha_0 \gtrsim 40°$.

of k_y would suggest that the DBS measurement is able to reproduce the true shape of the density-fluctuation wavenumber power spectrum $\int dk_x\rho_s\langle|\delta\hat{n}|^2(k_x, k_y)\rangle_T$. Figure 11(*a*) shows that the k_y dependence of $\int dk_x\rho_s|F_{x\mu}|^2/|F_0|^2$ varies by a factor ~ 3 for $k_y\rho_s \sim 0.4-40$ ($\alpha_0 \sim 3°-80°$). The red dots correspond to the values of the integral of the filter function for $\alpha_0 = 10°, 30°, 50°$ and $80°$. For small k_y (small α_0), the filter function is a decreasing function of k_y. This is due to the fact that for small α_0, the beam width focuses and produces an overall enhancement upon integration over the sampled k_x. In fact, $W_Y \sim \alpha_0$ for small α_0 (Belrhali *et al.* 2025), that is,
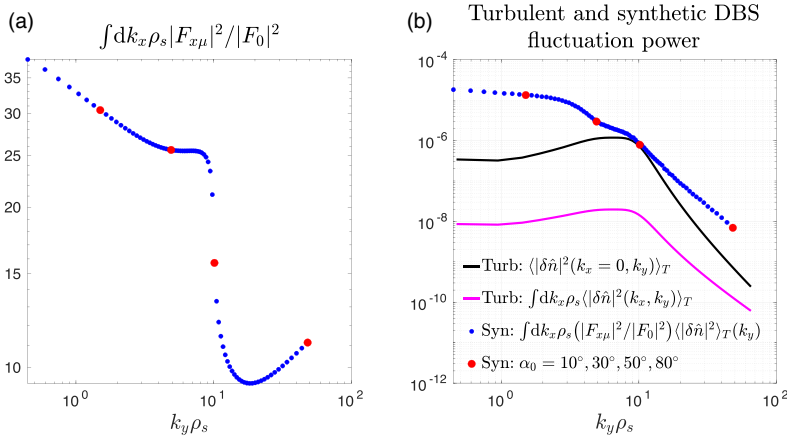
FIGURE 11. (*a*) Integrated filter function $\int \mathrm{d}k_x \rho_s |F_{x\mu}|^2/|F_0|^2$ for the scattered k_x within the plasma ($|k_x/K_0| < 2\cos\alpha_0$). Note how the integrated weight $\int \mathrm{d}k_x \rho_s |F_{x\mu}|^2/|F_0|^2$ is not constant, meaning that the filter function can affect the measured DBS k_y spectrum. (*b*) Turbulent spectrum $\langle|\delta\hat{n}|^2(k_x = 0, k_y)\rangle_T$ (black), k_x-integrated spectrum $\int \mathrm{d}k_x \rho_s \langle|\delta\hat{n}(k_x, k_y)|^2\rangle_T$ (magenta) and synthetic DBS spectrum $\int \mathrm{d}k_x \rho_s (|F_{x\mu}|^2/|F_0|^2)\langle|\delta\hat{n}|^2\rangle_T(k_x, k_y)$ (blue) as a function of k_y of the turbulence. The turbulence spectrum has been fitted to a gyrokinetic simulation (Ruiz *et al.* 2022). Note how the predicted DBS measurement is not able to capture the spectral peak of the turbulent spectrum (injection scale), but it is able to quantitatively reproduce the spectral exponent of the k_x-integrated spectrum. The red dots indicate the specific angles $\alpha_0 = 10°, 30°, 50°, 80°$ given for reference.

$|F_{x\mu}|^2 \sim 1/\alpha_0^2$ ($K_\mu \sim \alpha_0$). Since beam tracing assumes $W_Y \gg \lambda$, the decrease of W_Y at small α_0 means that, for small enough angles, beam tracing is bound to break down: the prediction of a signal enhancement for small angles might overestimate the true enhancement in reality, as discussed in detail by Maj *et al.* (2009, 2010). The precise angles for which this might happen and corrections to the beam-tracing model for small angles will be the subject of future publications.

For $k_y\rho_s \approx 4-5$ ($\alpha_0 \approx 30°$), the integrated filter function plateaus before abruptly decreasing for $\alpha_0 \approx 50°$. A similar plateau behaviour is observed in detailed measurements of the scattered power in DIII-D, reported in a recent publication by Pratt *et al.* (2023). In our case, this is due to the fact that for such large angles, beam focusing has started to take place close to the plasma exit (see figure 9*b*). This eliminates the signal enhancement due to the beam focusing inside the plasma (the k_x integration is only performed inside the plasma), therefore decreasing the value of the integrated filter function. For larger k_y ($\alpha_0 \gtrsim 60°$), the integrated filter increases. This last increase is due to the fact that the launch condition at the plasma edge starts to become important. For such large incidence angles, the beam is practically glancing and can be treated as a high-k backscattering system (Rhodes *et al.* 2006; Hillesheim *et al.* 2015). Figure 11(*a*) shows that the range of sampled radial wavenumbers in the density-fluctuation spectrum can have an important effect on the measured DBS power spectrum.

Figure 11(*b*) shows the turbulence binormal-wavenumber power spectrum $\langle|\delta\hat{n}|^2(k_x = 0, k_y)\rangle_T$ (black) corresponding to $k_x = 0$. This follows the traditional interpretation that dominant contributions to the DBS signal originate from

the cutoff. The magenta line shows the k_x-integrated wavenumber spectrum $\int \mathrm{d}k_x \rho_s \langle |\delta\hat{n}|^2(k_x, k_y)\rangle_T$. This could be interpreted as a line-integrated measurement of the density-fluctuation spectrum. The DBS system can be interpreted as a line-integrated measurement for large angles α_0, since for large α_0, $|F_{x\mu}|^2$ varies slowly and is not strongly peaked (see figure 7d). The extent to which it can be interpreted as a line integral rather than a localised measurement is quantified by the filter function $|F_{x\mu}|^2$, which we discuss next.

The blue dots in figure 11(b) show expected synthetic scattered power spectrum in a DBS measurement, given by the quantity $\int \mathrm{d}k_x \rho_s \left(|F_{x\mu}|^2/|F_0|^2\right) \langle |\delta\hat{n}|^2\rangle_T(k_x, k_y)$ in this beam-tracing model (see (3.9)). For each incidence angle α_0 (each k_y), the synthetic DBS scattered power includes the effect of the filter function and the radial wavenumber dependence of the density-fluctuation spectrum. As expected from the non-monotonic nature of $\int \mathrm{d}k_x \rho_s |F_{x\mu}|^2/|F_0|^2$ from figure 11(a), the synthetic scattered power does not reproduce the true density-fluctuation wavenumber spectrum for $k_x = 0$ nor the k_x-integrated spectrum. The peak in the density-fluctuation power spectrum ($k_y \rho_s \approx 6-8$), which is the driving scale of the turbulence, cannot be identified in the synthetic power spectrum. The peak should be visible for $\alpha_0 \approx 30°-40°$, where the beam model is expected to be quantitatively accurate (Maj *et al.* 2009, 2010). The enhancement of the synthetic scattered power with respect to the true turbulence spectrum for low k_y (small incidence angles $\alpha_0 \lesssim 20°$) is due to the enhancement of the signal by beam focusing. For larger $k_y \rho_s \gtrsim 10$ ($\alpha_0 \gtrsim 40°$), the synthetic spectrum exhibits a power-law spectral decay $\propto k_y^{-3.05}$, which is different from that of the true turbulent spectrum for $k_x = 0$ ($\propto k_y^{-4.16}$). The spectral decay is shown to quantitatively agree with the k_x-integrated spectrum, for which $\propto k_y^{-2.84}$. This suggests that DBS scattered power measurements could accurately capture the spectral exponent of the k_x-integrated spectrum, in contrast to the traditional belief that DBS measurements only select the $k_x = 0$ component (Hillesheim *et al.* 2012; Holland *et al.* 2012). For this particular NSTX-inspired case, the DBS scattered power measurements can quantitatively reproduce the true spectral exponent of the k_x-integrated, density-fluctuation power spectrum.

5. Conclusions and discussion

In this manuscript, we have discussed the phenomenon of beam focusing in the vicinity of a turning point. This phenomenon is not new and was already observed in numerical simulations for the 2-D linear-layer problem (Poli *et al.* 1999, 2001c; Yu. A. Kravtsov and Berczynski P., 2007), analytical calculations (Maj *et al.* 2009, 2010), as well as in numerical simulations in realistic tokamak geometry (Conway *et al.* 2007, 2015, 2019). These results were confirmed in this work by numerical simulations using the Scotty code for an NBI-heated L-mode plasma in the JET tokamak. The analytic solution derived from a 2-D linear-layer problem adjusted to fit the experimental conditions of JET discharge 97 080 showed encouraging agreement with the Scotty simulations for realistic 3-D tokamak geometry. This motivated us to study the phenomenon of beam focusing in the linear-layer problem. We have characterised the beam focusing in terms of the initial incident angle α_0, initial width W_0 and initial radius of curvature R_{Y0}. In particular, we have seen that beam focusing tends to be enhanced for decreasing angles, independently of R_{Y0}. For small enough α_0, the beam-tracing approximation becomes quantitatively inaccurate near the turning point, as discussed by Maj *et al.* (2009, 2010). Beam focusing also exhibits a clear dependence on the initial width W_0: initial widths small

with respect to $(\lambda L)^{\frac{1}{2}}$ lead to pronounced initial expansion due to diffraction of the electromagnetic waves as captured by the beam-tracing equations. Following the initial beam expansion for small W_0, the beam exhibits focusing in the vicinity of the turning point. For initial widths large with respect to $(\lambda L)^{\frac{1}{2}}$, the initial expansion can completely disappear to yield only an initial contraction towards a maximum focusing location in the vicinity of the turning point. The value and location of the beam focusing is shown to depend on the initial conditions α_0, W_0 and R_{Y0}.

We have used the analytical beam-tracing solution and applied it to the beam-tracing model for DBS (Hall-Chen *et al.*, 2022*b*). We have found an analytic expression for the filter function $|F_{x\mu}|^2/|F_0|^2 = K_0 W_0 / K_\mu W_{Y\mu}$ that characterises the scattering intensity along the beam path through the plasma, and we have studied it as a function of the beam initial conditions. This shows that W_Y is a critical parameter affecting the DBS scattering intensity along the path. We apply the lessons learned from our beam focusing formula to study the DBS filter function $|F_{x\mu}|^2$. When the beam focuses most (W_Y is minimal), the filter function is enhanced. This means that DBS is most sensitive to enhanced contributions from the vicinity of the focusing point, and as a consequence, it is most sensitive for small angles α_0 for which the focusing is large.

The filter function $|F_{xy,\mu}|^2$ in terms of k_x and k_y in Cartesian coordinates opens the door to implementing synthetic diagnostics for DBS perfomed previously (White *et al.* 2008; Holland *et al.* 2009; Leerink *et al.* 2010; Hillesheim *et al.* 2012; Holland *et al.* 2012; Leerink *et al.* 2012; Gusakov *et al.* 2013; Krutkin *et al.*, 2019*a*; Pratt *et al.* 2023; Patel *et al.* 2024). In the k_x direction, we recover formulae reported by Gusakov *et al.* (2017) when applied to the case of the auto-correlation (power) spectrum. In previous work, Gusakov *et al.* (2014, 2017) argued that a forward-scattering contribution to the DBS amplitude is responsible for the signal enhancement observed for decreasing incidence angle α_0, in DBS as well as in radial correlation Doppler reflectometry. The calculations by Gusakov *et al.* (2014, 2017) were based on the full-wave analytic solution to the Helmholtz equation, including the Airy-function behaviour near the turning point that is absent in our present description. Our work demonstrates that the enhancement of the DBS scattered power for decreasing incidence angles observed by Gusakov *et al.* (2014, 2017) can be completely explained via beam tracing, without the need of capturing the Airy behaviour in the vicinity of the turning point. We show that the underlying principle behind the enhancement of the DBS power is the beam focusing near the turning point and not forward scattering (in the form described by Gusakov *et al.* (2014, 2017). The formulae from §3 recover the k_y-resolution, or diagnostic wavenumber resolution Δk_y, that was already reported in previous work (Lin *et al.* 2001; Hirsch *et al.* 2001; Hillesheim *et al.* 2012). We find that Δk_y is dependent on the initial conditions α_0, W_0 and R_{Y0} and on L, and is constant along the path.

In addition to discussing the effect of the filter function $|F_{x\mu}|^2$ on the total DBS scattered power measurement, we have studied the effect of the turbulent wavenumber spectrum on the measured total scattered power. We have used a realistic representation of the turbulence spectrum based on gyrokinetic simulations, as done by Ruiz *et al.* (2022). We show the combined effect of the k_x dependence of the filter function and the k_x dependence of the turbulence spectrum. In an NSTX-inspired example, the filter function is shown to have a most dominant effect for small angles $\alpha_0 = 10°$, $30°$ since for these specific conditions, DBS is sensitive to

low-to-intermediate k_y and the spectrum is large. For larger angles, the filter function selects larger $k_y = -2K_0 \sin \alpha_0$. In the specific condition analysed, $\alpha_0 > 50°$ corresponded to wavenumbers k_y with small turbulent power in the spectrum. In those conditions, the filter function was shown to have little effect on the measurement and the dominant contributions to the scattered power could directly be assessed from the intrinsic turbulent spectrum itself. We also show that the filter function integrated over k_x is far from being constant and is strongly dependent on the k_y selected. The integrated filter function can be affected by the beam focusing inside or outside the plasma and the launch condition. This shows that one expects the total scattered power to depend on the incident angle of beam injection in the plasma, α_0. For the particular NSTX turbulent spectrum studied in this manuscript, we show that the measured DBS scattered power spectrum could not recover the peak in the true density-fluctuation spectrum. The power-law decay exponent of the synthetic DBS spectrum can reproduce the k_x-integrated turbulence spectrum, but not the spectrum for $k_x = 0$.

This work helps characterise and interpret the total scattered power measured by DBS. Little attention has been paid to the spectral frequency power spectrum and specific experimental analysis techniques that are usually employed to study it. For example, of particular importance is the dependence of the Doppler-shifted DBS frequency spectrum on the diagnostic wavenumber resolution, as well as the effect of the $k_x = 0$ component (which is directly related to the beam focusing). The impact on the measured frequency spectrum remains an open question, but could be easily tackled using the reduced filter function developed in this work. This will require further analysis of the model and comparisons to experiments, which could be the subject of future publications.

To our knowledge, the beam focusing discussed in this manuscript has never been experimentally observed and future experiments should seek to experimentally confirm it. One option could be to set up scattering experiments from plasma fluctuations which exhibit a density gradient (not necessarily in magnetic confinement devices). Arranging different viewing channels that are sensitive to different parts of the beam trajectory along the path and assuming that the intensity of the plasma fluctuations is similar between the different regions in the plasma that each channel is sensitive to, one should expect enhanced scattering contributions from channels that are aimed at regions where the beam is focused, since the beam intensity is enhanced.

Lastly, the model presented here has limitations for small enough incident angles α_0, that is, for close to normal incidence beams. One can show that the filter function $|F_{x\mu}|^2 \propto 1/\alpha_0^2$ for small angles. That explains the highly peaked behaviour of the filter function in figures 5(*a*) and 7(*a*) near the focusing region. This behaviour has its origin in the beam-tracing solution for the electric field, for which one can show that $E_b \propto 1/\alpha_0$ for small angles (Belrhali *et al.* 2025). This was studied by Maj *et al.* (2009, 2010). However, as pointed out in Maj's work, the validity of the beam-tracing approximation is questionable for small enough incident angles. The beam-tracing solution for E_b might be overpredicting the electric-field enhancement due to focusing. In the exact solution for the electric field, one expects Airy behaviour to become important through interference between the incident and returning beams in the vicinity of the turning point, especially in conditions in which the beam width W_Y approaches the Airy length $l_{Ai} = (L/K_0^2)^{\frac{1}{3}}$. This behaviour is absent in the beam-tracing model, which expands the Airy behaviour asymptotically far from the turning

point. Although the beam-tracing solution might be overpredicting the electric-field enhancement in the vicinity of the focusing region, we are confident that the phenomenon of beam focusing is physical, as confirmed by Maj *et al.* (2009, 2010) and by our recent work. Future work will seek to employ more sophisticated models than beam tracing that capture Airy behaviour (as done in recent publications, such as Lopez, Kur & Strozzi 2023) to quantify how accurate the total integrated power enhancement predicted by beam tracing is for small incidence angles.

Declaration of interests

The authors report no conflict of interest.

Appendix A. Analytic beam-tracing solution for the linear-layer problem.

We solve the beam-tracing equations in a 2-D slab for the O-mode with a constant density gradient ($\omega_{pe}^2(x) = \Omega^2 x/L$, where x is our Cartesian coordinate in figure 1) and launch frequency Ω. We will make use of the dispersion relation $H = 0$, which takes the form $H = K^2/K_0^2 - 1 + \omega_{pe}^2/\Omega^2 = 0$ for the O-mode. The general beam-tracing evolution equation for $\boldsymbol{\Psi}$ is calculated along the central ray path and reads (Hall-Chen *et al.* 2022*b*)

$$\frac{\mathrm{d}\boldsymbol{\Psi}}{\mathrm{d}\tau} = -\left(\boldsymbol{\Psi} \cdot \nabla_K \nabla_K H \cdot \boldsymbol{\Psi} + \boldsymbol{\Psi} \cdot \nabla_K \nabla H + \nabla \nabla_K H \cdot \boldsymbol{\Psi} + \nabla \nabla H\right). \quad \text{(A.1)}$$

The analytic solution to the Gaussian beam-tracing equations was already obtained by Pereverzev (1998) and Poli *et al.* (1999) for the 2-D linear-layer problem and normal incidence ($\alpha_0 = 0$). The solution for the oblique incidence angle was obtained by Maj *et al.* (2009, 2010). The beam-tracing equation (A.1) in the linear-layer problem reduces to $\mathrm{d}\boldsymbol{\Psi}/\mathrm{d}\tau = -(2/K_0^2)\boldsymbol{\Psi}^2$ since we have $\nabla \nabla H = 0$, $\nabla_K \nabla H = \nabla \nabla_K H = 0$ and $\nabla_K \nabla_K H = (2/K_0^2)\mathbf{I}$, where $\mathbf{I}$ is the identity matrix. Normalising $\boldsymbol{\Psi}$ by K_0/L and τ by

$K_0 L$, the corresponding solution for $\boldsymbol{\Psi}' = \boldsymbol{\Psi}(L/K_0)$ is

$$\boldsymbol{\Psi}'^{-1}(\tau') = 2\tau' \mathbf{I} + \boldsymbol{\Psi}'^{-1}(0). \tag{A.2}$$

The matrix $\boldsymbol{\Psi}'$ must also satisfy the constraint

$$\nabla_K H \cdot \boldsymbol{\Psi}' + \nabla H \frac{L}{K_0} = 0. \tag{A.3}$$

At $\tau = 0$, (A.3) gives

$$\boldsymbol{\Psi}'(0) = \begin{pmatrix} \Psi'_{xx0} & \Psi'_{xy0} & \Psi'_{xz0} \\ \Psi'_{xy0} & \Psi'_{yy0} & \Psi'_{yz0} \\ \Psi'_{xz0} & \Psi'_{yz0} & \Psi'_{zz0} \end{pmatrix} = \begin{pmatrix} \Psi'_{yy0} \tan^2 \alpha_0 - \frac{1}{2\cos\alpha_0} & -\Psi'_{yy0} \tan\alpha_0 & 0 \\ -\Psi'_{yy0} \tan\alpha_0 & \Psi'_{yy0} & 0 \\ 0 & 0 & \Psi'_{zz0} \end{pmatrix}, \tag{A.4}$$

where the zeros along the third row and column are a particular choice of initial condition. With this choice, one only needs Ψ'_{yy0} and α_0 to specify the initial conditions for the beam in the 2-D linear-layer problem.

The beam-tracing equations are more easily solved in the lab frame $\{\hat{\mathbf{x}}, \hat{\mathbf{y}}, \hat{\mathbf{z}}\}$ (figure 1), but to interpret the results, it is useful to use the beam frame. Noting that $\mathbf{r} = \mathbf{q} + Y\hat{\mathbf{Y}} + X\hat{\mathbf{X}}$, we find that $(\mathbf{r} - \mathbf{q}(\tau)) \cdot \boldsymbol{\Psi} \cdot (\mathbf{r} - \mathbf{q}(\tau)) = \Psi_{YY} Y^2 + 2\Psi_{XY} XY + \Psi_{XX} X^2$, where $\Psi_{YY} = \hat{\mathbf{Y}} \cdot \boldsymbol{\Psi} \cdot \hat{\mathbf{Y}}$, $\Psi_{XY} = \hat{\mathbf{X}} \cdot \boldsymbol{\Psi} \cdot \hat{\mathbf{Y}}$ and $\Psi_{XX} = \hat{\mathbf{X}} \cdot \boldsymbol{\Psi} \cdot \hat{\mathbf{X}}$. The other components of $\boldsymbol{\Psi}$ are defined by $\Psi_{Yg} = \hat{\mathbf{Y}} \cdot \boldsymbol{\Psi} \cdot \hat{\mathbf{g}}$, $\Psi_{Xg} = \hat{\mathbf{X}} \cdot \boldsymbol{\Psi} \cdot \hat{\mathbf{g}}$ and $\Psi_{gg} = \hat{\mathbf{g}} \cdot \boldsymbol{\Psi} \cdot \hat{\mathbf{g}}$. They are determined from (A.3) and given by

$$\begin{aligned} \hat{\mathbf{Y}} \cdot \boldsymbol{\Psi}' \cdot \hat{\mathbf{g}} &= -\frac{1}{g} (\nabla H \cdot \hat{\mathbf{Y}}) \frac{L}{K_0}, \\ \hat{\mathbf{g}} \cdot \boldsymbol{\Psi}' \cdot \hat{\mathbf{g}} &= -\frac{1}{g} (\nabla H \cdot \hat{\mathbf{g}}) \frac{L}{K_0}, \\ \hat{\mathbf{X}} \cdot \boldsymbol{\Psi}' \cdot \hat{\mathbf{g}} &= -\frac{1}{g} (\nabla H \cdot \hat{\mathbf{X}}) \frac{L}{K_0} = 0. \end{aligned} \tag{A.5}$$

Evaluating (A.5) at $\tau = 0$, we have

$$\begin{pmatrix} \Psi'_{YY0} & \Psi'_{Yg0} & \Psi'_{YX0} \\ \Psi'_{Yg0} & \Psi'_{gg0} & \Psi'_{Xg0} \\ \Psi'_{YX0} & \Psi'_{Xg0} & \Psi'_{XX0} \end{pmatrix} = \begin{pmatrix} \Psi'_{YY0} & -\frac{1}{2}\sin\alpha_0 & 0 \\ -\frac{1}{2}\sin\alpha_0 & -\frac{1}{2}\cos\alpha_0 & 0 \\ 0 & 0 & \Psi'_{zz0} \end{pmatrix}, \tag{A.6}$$

where Ψ'_{YY0} is the beam-frame initial condition. In (A.6), the initial condition $\Psi'_{YX0} = 0$ is a choice that is consistent with (A.4), and the component Ψ'_{YY0} in (A.6) is related to Ψ'_{yy0} in (A.4). We proceed to discuss how.

According to our discussion above, the matrix $\boldsymbol{\Psi}$ is given by

$$\begin{pmatrix} \Psi_{YY} & \Psi_{Yg} & \Psi_{YX} \\ \Psi_{Yg} & \Psi_{gg} & \Psi_{Xg} \\ \Psi_{YX} & \Psi_{Xg} & \Psi_{XX} \end{pmatrix} = \mathbf{R}_\alpha^{\mathrm{T}}(\tau) \begin{pmatrix} \Psi_{xx} & \Psi_{xy} & \Psi_{xz} \\ \Psi_{xy} & \Psi_{yy} & \Psi_{yz} \\ \Psi_{xz} & \Psi_{yz} & \Psi_{zz} \end{pmatrix} \mathbf{R}_\alpha(\tau), \tag{A.7}$$

where

$$\mathbf{R}_\alpha(\tau) = \begin{pmatrix} \sin\alpha(\tau) & \cos\alpha(\tau) & 0 \\ -\cos\alpha(\tau) & \sin\alpha(\tau) & 0 \\ 0 & 0 & 1 \end{pmatrix}. \tag{A.8}$$

Equations (A.7) and (A.8) show that the components of Ψ in the lab frame are related to those in the beam frame by a change of basis that corresponds to a simple rotation of angle $\pi/2 - \alpha$ along $\hat{z} = \hat{X}$ (figure 1). Note that $\Psi_{YX} = 0$ implies $\Psi_{xz} = \Psi_{yz} = 0$, which gives an easy interpretation to our choice of initial conditions in (A.4): the cross-section of the beam is not tilted in the $\{\hat{X}, \hat{Y}\}$ plane.

The evolution of the angle α along the path can be easily computed from the trajectory of the central ray (see (2.9)). It is given by

$$
\begin{aligned}
\tan \alpha &= \frac{\tan \alpha_0}{1 - \tau'/\cos \alpha_0} = \sin \alpha_0 \frac{K_0}{K_x}, \\
\sin \alpha &= \frac{\sin \alpha_0}{(1 - 2\tau' \cos \alpha_0 + \tau'^2)^{1/2}} = \sin \alpha_0 \frac{K_0}{K}, \\
\cos \alpha &= \frac{\cos \alpha_0 - \tau'}{(1 - 2\tau' \cos \alpha_0 + \tau'^2)^{1/2}} = \frac{K_x}{K}.
\end{aligned}
\tag{A.9}
$$

Using (A.7) and (A.8), one can relate the beam-frame initial condition $\Psi_{YY0} = K_0/R_{Y0} + i2/W_0^2$ to the lab-frame initial condition Ψ'_{yy0}, yielding $\Psi'_{YY0} = -\sin^2 \alpha_0/(2 \cos \alpha_0) + \Psi'_{yy0}/\cos^2 \alpha_0$. The change of basis in (A.7) also gives the following relations between all the beam-frame and lab-frame components:

$$
\begin{aligned}
\Psi_{YY}(\tau') &= \Psi_{xx} \sin^2 \alpha - 2\Psi_{xy} \sin \alpha \cos \alpha + \Psi_{yy} \cos^2 \alpha, \\
\Psi_{Yg}(\tau') &= \left(\Psi_{xx} - \Psi_{yy} \right) \sin \alpha \cos \alpha + \Psi_{xy} \left(\sin^2 \alpha - \cos^2 \alpha \right), \\
\Psi_{gg}(\tau') &= \Psi_{xx} \cos^2 \alpha + 2\Psi_{xy} \sin \alpha \cos \alpha + \Psi_{yy} \sin^2 \alpha, \\
\Psi_{XX}(\tau') &= \Psi_{zz}.
\end{aligned}
\tag{A.10}
$$

We now provide the lab-frame solution, derived from (A.2),

$$
\begin{aligned}
\Psi'_{xx}(\tau') &= \frac{\Psi'_{xx0} + 2\Delta_0 \tau'}{D(\tau')}, \\
\Psi'_{xy}(\tau') &= \frac{\Psi'_{xy0}}{D(\tau')}, \\
\Psi'_{yy}(\tau') &= \frac{\Psi'_{yy0} + 2\Delta_0 \tau'}{D(\tau')}.
\end{aligned}
\tag{A.11}
$$

Here, the denominator $D(\tau')$ can be readily expressed in terms of the lab-frame $\hat{x}$ component of the central ray $\mathbf{K}$, K_x, yielding

$$
\begin{aligned}
D(\tau') &= 1 + 2\tau' \mathrm{Tr}_0 + 4\Delta_0 \tau'^2 \\
&= \frac{1}{\cos \alpha_0} \frac{K_x}{K_0} + 2\frac{\Psi'_{yy0}}{\cos \alpha_0} \left(\frac{\cos^2 \alpha_0 - \sin^2 \alpha_0}{\cos \alpha_0} \frac{K_x}{K_0} + \sin^2 \alpha_0 - \frac{K_x^2}{K_0^2} \right),
\end{aligned}
\tag{A.12}
$$

with

$$
\begin{aligned}
\Delta_0 &= (\Psi'_{yy} \Psi'_{xx} - \Psi'^2_{xy})_0 = (\Psi'_{YY} \Psi'_{gg} - \Psi'^2_{Yg})_0 = -\frac{\Psi'_{yy0}}{2 \cos \alpha_0}, \\
\mathrm{Tr}_0 &= (\Psi'_{yy} + \Psi'_{xx})_0 = (\Psi'_{gg} + \Psi'_{YY})_0 = -\frac{1}{2 \cos \alpha_0} + \frac{\Psi'_{yy0}}{\cos^2 \alpha_0},
\end{aligned}
\tag{A.13}
$$

where we used $\tau' = \cos\alpha_0 - K_x/K_0$. It is convenient to express (A.11) in terms of K_x and the initial conditions α_0, Ψ'_{yy0} and K_0. We have

$$
\begin{aligned}
\Psi'_{xx} &= \sin^2\alpha_0 \frac{K_0^2}{K_x^2}\Psi'_{yy} - \frac{1}{2}\frac{K_0}{K_x}, \\
\Psi'_{xy} &= -\sin\alpha_0 \frac{K_0}{K_x}\Psi'_{yy}, \\
\Psi'_{yy} &= \frac{\Psi'_{yy0}\frac{K_x}{K_0}}{\cos\alpha_0 D(K_x)}.
\end{aligned}
\tag{A.14}
$$

The denominator D in (A.14) is a function of K_x and is evaluated using the second line of (A.12).

Using the evolution of the angle α along the path in (A.9), and $\Psi_{YY}(\tau') = \Psi_{xx}\sin^2\alpha - 2\Psi_{xy}\sin\alpha\cos\alpha + \Psi_{yy}\cos^2\alpha$ (see (A.10)), we arrive at the final solution for Ψ'_{YY} given in (2.10). Equation (2.10) contains the beam-focusing phenomenon for the 2-D linear-layer problem through $W_Y = (2/\Im[\Psi_{YY}])^{\frac{1}{2}}$. Expressing Ψ_{YY} as a function of the central ray K_x is convenient, since it readily allows us to express W_Y as a function of the turbulent scattered k_x, as done in this manuscript. We simply substitute $k_x = -2K_x$ (Bragg condition).

At this point, it is worth relating the beam-tracing solution to previous work. Gusakov *et al.* (2014, 2017) employ particular initial conditions for the beam-tracing equations. Gusakov *et al.* (2014, 2017) perform their calculations in the lab frame, setting the initial conditions to

$$
\begin{aligned}
\Psi'_{yy0} &\equiv i\gamma, \\
\Psi'_{xx0} &= i\gamma\tan^2\alpha_0 - \frac{1}{2\cos\alpha_0}, \\
\Psi'_{xy0} &= -i\gamma\tan\alpha_0,
\end{aligned}
\tag{A.15}
$$

where $\gamma = L/(K_0\rho^2)$ is purely real. Equations (A.15) are very particular initial conditions since they define a purely imaginary Ψ_{yy0} in the lab frame, but not in the beam frame. This means that this initial condition does not correspond to the beam waist at launch, but has a specific initial value for the radius of curvature in the beam frame. Using the relation between Ψ_{YY0} and Ψ_{yy0} in (A.10), we have $R_{Y0}/L = -2\cos\alpha_0/\sin^2\alpha_0$, $W_0 = \sqrt{2}\rho\cos\alpha_0$. Note that we can recover expressions by Gusakov *et al.* (2017) by setting $\Psi'_{yy0} \to i\gamma$. In the work of Gusakov *et al.* (2014, 2017), (A.11), (A.12) and (A.13) show that Ψ'_{yy} can be explicitly written as

$$
\begin{aligned}
\Psi'_{yy}(K_x) &= \frac{2\gamma^2\left(\frac{\cos^2\alpha_0 - \sin^2\alpha_0}{\cos\alpha_0} + \frac{K_0}{K_x}\sin^2\alpha_0 - \frac{K_x}{K_0}\right)}{1 + 4\gamma^2\left(\frac{\cos^2\alpha_0 - \sin^2\alpha_0}{\cos\alpha_0} + \frac{K_0}{K_x}\sin^2\alpha_0 - \frac{K_x}{K_0}\right)^2} \\
&+ \frac{i\gamma}{1 + 4\gamma^2\left(\frac{\cos^2\alpha_0 - \sin^2\alpha_0}{\cos\alpha_0} + \frac{K_0}{K_x}\sin^2\alpha_0 - \frac{K_x}{K_0}\right)^2}.
\end{aligned}
\tag{A.16}
$$

The particular initial conditions from Gusakov *et al.* (2014, 2017) finally yield

$$\Psi'_{YY}(K_x) = \frac{-\frac{1}{2}\sin^2\alpha_0 + i\gamma\left[\frac{K_x^3}{K_0^3} + 3\sin^2\alpha_0\frac{K_x}{K_0} - \frac{\sin^2\alpha_0}{\cos\alpha_0}\left(\cos^2\alpha_0 - \sin^2\alpha_0\right)\right]}{\left[\sin^2\alpha_0 + \frac{K_x^2}{K_0^2}\right]\left[\frac{K_x}{K_0} + 2i\gamma\left(\frac{\cos^2\alpha_0 - \sin^2\alpha_0}{\cos\alpha_0}\frac{K_x}{K_0} + \sin^2\alpha_0 - \frac{K_x^2}{K_0^2}\right)\right]}.$$

$$(A.17)$$

Using W_Y computed from (A.17) and $|F_{x\mu}|^2/|F_0|^2 = K_0 W_0/K_\mu W_{Y\mu}$ recovers (14) and (15) from Gusakov *et al.* (2017).

Appendix B. Details of the scattered power calculations

In this appendix, we provide details of the scattered-power calculations in the 2-D linear-layer problem from § 3. We follow a derivation analogous to that of Hall-Chen et al. (2022*b*), but using Cartesian coordinates instead of beam-aligned coordinates. The position (x, y) in Cartesian coordinates is related to the (τ, Y) coordinates by $x = x_c(\tau) + Y\sin\alpha(\tau)$, $y = y_c(\tau) - Y\cos\alpha(\tau)$ (see (3.2)), where (x_c, y_c) are the coordinates along the central ray (figure 1), and $\sin\alpha$ and $\cos\alpha$ are given by (A.9). The density fluctuations are expressed in terms of (x, y) and the conjugate turbulent wavevector is expressed in its Cartesian components $\mathbf{k}_\perp = k_x\hat{\mathbf{x}} + k_y\hat{\mathbf{y}}$, that is, we have $\delta n(x, y, t) = \int \mathrm{d}k_x\mathrm{d}k_y\,\delta\hat{n}(k_x, k_y)\exp(ik_x x + ik_y y)$ (see (3.1)). Starting from (100) of Hall-Chen *et al.* (2022*b*), the scattered amplitude can be written as

$$A_r(t) = \frac{i\Omega A_{ant}}{2\pi c}\int \mathrm{d}V\,\mathrm{d}k_x\,\mathrm{d}k_y\,\Im[\Psi_{YY}]^{\frac{1}{2}}\Im[\Psi_{XX}]^{\frac{1}{2}}\frac{g_{ant}}{g}\exp(i2\phi_G)\frac{\delta\hat{n}}{n}\left[\hat{\mathbf{e}}^*\cdot(\boldsymbol{\epsilon}_{eq} - \mathbf{1})\cdot\hat{\mathbf{e}}\right]$$
$$\times \exp\left[i\left(2s + k_x(x_c(\tau) + Y\sin\alpha) + k_y(y_c(\tau) - Y\cos\alpha)\right.\right.$$
$$\left.\left. + X^2\Psi_{XX} + Y^2\Psi_{YY}\right)\right],$$

$$(B.1)$$

where the differential volume element is $\mathrm{d}V \approx g\mathrm{d}\tau\,\mathrm{d}X\,\mathrm{d}Y$ (see (114) of Hall-Chen *et al.* 2022*b*) and $\boldsymbol{\epsilon}_{eq}$ is the equilibrium part of the cold-plasma dielectric tensor (note the approximately equal sign, since $\mathrm{d}V$ has corrections of order $\sim \lambda/W$ due to the fact that $\hat{\mathbf{X}}$ and $\hat{\mathbf{Y}}$ depend on τ). In (B.1), the integrals in X and Y are integrals of a complex Gaussian and give

$$A_r(t) = \frac{-\Omega A_{ant}g_{ant}}{2c}\int \mathrm{d}k_x\mathrm{d}k_y\frac{\delta\hat{n}}{n}\int \mathrm{d}\tau\left[\frac{\Im[\Psi_{YY}]}{\Psi_{YY}}\right]^{\frac{1}{2}}\left[\hat{\mathbf{e}}^*\cdot(\boldsymbol{\epsilon}_{eq} - \mathbf{1})\cdot\hat{\mathbf{e}}\right]$$
$$\times \exp(i2\phi_G)\exp[if(\tau)],$$

$$(B.2)$$

where we set $\Im[\Psi_{XX}]/\Psi_{XX} = 1$ (to be able to ignore the variation along the field line direction X). Here, $f(\tau)$ is

$$f(\tau) = 2s + k_x x_c(\tau) + k_y y_c(\tau) - (\mathbf{k}_\perp \cdot \hat{\mathbf{Y}})^2/4\Psi_{YY},$$

$$(B.3)$$

where $\mathbf{k}_\perp \cdot \hat{\mathbf{Y}} = k_x\sin\alpha - k_y\cos\alpha$ from (3.5). The largest piece in f is given by

$$f_0 = 2s + k_x x_c + k_y y_c,$$

$$(B.4)$$

where $f_0 \sim L/\lambda$. The last term in (B.3) is order ~ 1, since $\mathbf{k}_\perp \cdot \hat{\mathbf{Y}} \sim 1/W$. Naively, this would suggest calculating the integral in τ from (B.2) via the method of stationary phase using $\mathrm{d}f_0/\mathrm{d}\tau = 0$. This results in a point of stationary phase $\tau_\mu \sim L/\lambda$ that is

real, but yields an error of order ~ 1 in the result, as we shall see. The reason for this is subtle. While the exponent $\exp[if(\tau)]$ from the τ integral in (B.2) appears to be imaginary at first sight, it is not quite imaginary due to the term $\exp[-i(\mathbf{k}_\perp \cdot \hat{\mathbf{Y}})^2/4\Psi_{YY}]$. Even though this term is order ~ 1, it ends up giving rise to an order ~ 1 error in the result. This is because, despite being order ~ 1, its first and second derivatives are not.

We start by calculating the τ integral in (B.2) using the traditional stationary phase from the largest part $\exp[if_0]$, while keeping the term $\exp[-i(\mathbf{k}_\perp \cdot \hat{\mathbf{Y}})^2/4\Psi_{YY}] \sim 1$ constant. We call τ_μ the solution to $\mathrm{d}f_0/\mathrm{d}\tau|_\mu = 0$, which defines a point along the trajectory of the central ray where, for a given $\mathbf{k}_\perp$, we have the resonant Bragg condition $2K_\mu + \mathbf{k}_\perp \cdot \hat{\mathbf{g}}_\mu = 0$. Now, consider a point situated at a distance $\Delta\tau \sim W/\lambda \ll \tau_\mu$ from τ_μ. At that point, the phase f_0 gives the following contribution:

$$f_0(\tau_\mu + \Delta\tau) = f_0(\tau_\mu) + \frac{\mathrm{d}^2 f_0}{\mathrm{d}\tau^2}\bigg|_\mu \frac{(\Delta\tau)^2}{2} + O\left(\frac{\lambda}{W}\right), \tag{B.5}$$

where $(\mathrm{d}^2 f_0/\mathrm{d}\tau^2)|_\mu (\Delta\tau)^2/2 \sim 1$. Next, we calculate the contributions from $\exp[-i(\mathbf{k}_\perp \cdot \hat{\mathbf{Y}})^2/4\Psi_{YY}]$ at $\tau_\mu + \Delta\tau$. We find

$$\begin{aligned} -\frac{(\mathbf{k}_\perp \cdot \hat{\mathbf{Y}})^2}{4\Psi_{YY}}\bigg|_{\tau_\mu + \Delta\tau} = &-\frac{(\mathbf{k}_\perp \cdot \hat{\mathbf{Y}}_\mu)^2}{4\Psi_{YY\mu}} - \frac{(\mathbf{k}_\perp \cdot \hat{\mathbf{g}}_\mu)(\mathbf{k}_\perp \cdot \hat{\mathbf{Y}}_\mu)}{2\Psi_{YY\mu}}\frac{\mathrm{d}\alpha}{\mathrm{d}\tau}\bigg|_\mu \Delta\tau \\ &-\frac{(\mathbf{k}_\perp \cdot \hat{\mathbf{g}}_\mu)^2}{2\Psi_{YY\mu}}\left(\frac{\mathrm{d}\alpha}{\mathrm{d}\tau}\right)^2\bigg|_\mu \frac{(\Delta\tau)^2}{2} + O\left(\frac{\lambda}{W}\right), \end{aligned} \tag{B.6}$$

where we used the following relation between the unit vectors:

$$\begin{aligned} \frac{\mathrm{d}\hat{\mathbf{g}}}{\mathrm{d}\tau} &= -\hat{\mathbf{Y}}\frac{\mathrm{d}\alpha}{\mathrm{d}\tau}, \\ \frac{\mathrm{d}\hat{\mathbf{Y}}}{\mathrm{d}\tau} &= \hat{\mathbf{g}}\frac{\mathrm{d}\alpha}{\mathrm{d}\tau}. \end{aligned} \tag{B.7}$$

Equation (B.7) can be easily proven by taking the derivative of the unit vectors in (2.6). Using the fact that $\mathbf{k}_\perp \cdot \hat{\mathbf{g}} \sim 1/\lambda$ and $\mathbf{k}_\perp \cdot \hat{\mathbf{Y}} \sim 1/W$, we note that all terms in (B.6) are ~ 1. This is contradictory, because the term $-i(\mathbf{k}_\perp \cdot \hat{\mathbf{Y}})^2/4\Psi_{YY}|_{\tau_\mu + \Delta\tau}$ in (B.6) should be approximately $-i(\mathbf{k}_\perp \cdot \hat{\mathbf{Y}})^2/4\Psi_{YY}|_\mu$ for the method of stationary phase to work. The corrections to that term from small deviations $\Delta\tau$ should have been $\sim \lambda/W$ or smaller. They are not smaller because, despite being ~ 1 at $\tau = \tau_\mu$, the term $-(\mathbf{k}_\perp \cdot \hat{\mathbf{Y}})^2/4\Psi_{YY}$ is not ~ 1 for $\tau - \tau_\mu \sim W/\lambda$. The fact that we find that the corrections to that term from a small deviation $\Delta\tau$ to τ_μ are important suggests that, in fact, the term $-i(\mathbf{k}_\perp \cdot \hat{\mathbf{Y}})^2/4\Psi_{YY}$ has to be taken into account in the stationary phase calculation, alongside f_0, despite the fact that it is, at first sight, order ~ 1 for $\tau = \tau_\mu$ and $f_0 \sim L/\lambda$. Having shown this, we proceed to calculate the dominant contribution to the τ integral in (B.2) by a method related to the steepest descent (Bender & Orszag 1978), but not exactly the steepest descent method.

The τ integral in (B.2) is dominated by the region around $\mathrm{d}f/\mathrm{d}\tau = 0$, where

$$\frac{\mathrm{d}f}{\mathrm{d}\tau} = 2Kg + k_x\frac{\mathrm{d}x_c}{\mathrm{d}\tau} + k_y\frac{\mathrm{d}y_c}{\mathrm{d}\tau} - \frac{(\mathbf{k}_\perp \cdot \hat{\mathbf{g}})(\mathbf{k}_\perp \cdot \hat{\mathbf{Y}})}{2\Psi_{YY}}\frac{\mathrm{d}\alpha}{\mathrm{d}\tau} - \frac{(\mathbf{k}_\perp \cdot \hat{\mathbf{Y}})^2}{4}\frac{\mathrm{d}}{\mathrm{d}\tau}\left(\frac{1}{\Psi_{YY}}\right), \tag{B.8}$$

where the first three terms on the right-hand side are order ~ 1, the fourth term is order $\sim \lambda/W$ and the last term is $\sim \lambda/L$. Note that directly setting $df/d\tau = 0$ (steepest descent) will give a complex value for τ_μ. One option to calculate the exact steepest descent point is to solve $df/d\tau = 0$ for τ in (B.8), as a function of $k_x, k_y, K_0 L, \alpha_0$ and Ψ_{yy0}, by using the exact expression for Ψ_{YY} in (2.10), as well as (A.9). This leads to a high-order polynomial in τ that does not admit an analytic solution in the general case. Instead, here we choose to solve $df/d\tau = 0$ perturbatively for τ in (B.8). We will find that the τ that satisfies (B.8) can be written as $\tau_\mu + \Delta\tau$, where τ_μ is the real solution to $df_0/d\tau = 0$ (using (B.5)). We will find that $\Delta\tau$ is complex. This appears to pose a problem, since the functions $s, x_c, y_c, \hat{Y}$ and Ψ_{YY} in f are functions of a real τ. This means that we have to analytically continue them to the complex plane. One can wonder how much one can extended these functions away from real τ. That turns out not to be very important because we are going to prove that one only needs to modify the path by a very small amount: the saddle point will only be a small distance $\Delta\tau \sim (W/L)\tau_\mu$ away from the original real path. Since W/L is an asymptotically small number, the deviation from the original path into the complex plane will be sufficiently small that no pole, branch point or fundamental singularity will be crossed.

Having established the validity of the analytic continuation into the complex plane by distances of order W/L from the original path, we now calculate that distance $\Delta\tau$ and how it contributes to the τ integral in (B.2). We note that (B.3) implies that $\mathbf{k}_\perp \cdot \hat{\mathbf{Y}} \sim 1/W$, and hence the term proportional to $(\mathbf{k}_\perp \cdot \hat{\mathbf{g}})(\mathbf{k}_\perp \cdot \hat{\mathbf{Y}})$ in (B.8) is small in λ/W. This motivates splitting the root into two pieces $\tau_\mu + \Delta\tau$, where τ_μ is real and $\Delta\tau \sim (\lambda/W)\tau_\mu$ is complex, and expanding the Bragg condition order by order in λ/W. We denote quantities evaluated at τ_μ with the subscript μ (e.g. $K(\tau_\mu) = K_\mu$). At the lowest order, we have

$$\left.\frac{df}{d\tau}\right|_{\tau_\mu} \approx \left.\frac{df_0}{d\tau}\right|_{\tau_\mu} = 2K_\mu g_\mu + k_x \left.\frac{dx_c}{d\tau}\right|_{\tau_\mu} + k_y \left.\frac{dy_c}{d\tau}\right|_{\tau_\mu} = 0, \tag{B.9}$$

where f_0 is given by (B.4). The zeroth-order Bragg condition in (B.9) can be explicitly written in terms of $K_{x\mu}$ as follows:

$$2\frac{K_{x\mu}^2}{K_0^2} + \frac{k_x}{K_0}\frac{K_{x\mu}}{K_0} + \sin\alpha_0\left(\frac{k_y}{K_0} + 2\sin\alpha_0\right) = 0, \tag{B.10}$$

where we used (2.9) and the expression $g_\mu = 2K_\mu/K_0^2$. Using the fact that $\mathbf{k}_\perp \cdot \hat{\mathbf{Y}} \sim 1/W$ and employing (A.9) gives $k_x \approx k_y/\tan\alpha_\mu$ and hence

$$k_y + 2K_0 \sin\alpha_0 \sim 1/W. \tag{B.11}$$

Note that (B.10) exhibits two solutions for $K_{x\mu}$. Following (B.11), we expand the two solutions for small $k_y + 2K_0 \sin\alpha_0$. We find

$$K_{x\mu} \approx \begin{cases} -\sin\alpha_0(k_y + 2K_0 \sin\alpha_0)K_0/k_x \\ -k_x/2 + \sin\alpha_0(k_y + 2K_0 \sin\alpha_0)K_0/k_x \end{cases}, \tag{B.12}$$

where only the second solution $\sim 1/\lambda$ is physically relevant. This shows that $K_{x\mu} = -k_x/2 + O(1/W)$. As we anticipated, the Bragg condition calculated to zeroth-order

is not sufficient to calculate the terms that are order ~ 1 in the phase or in the amplitude.

Next, we use the fact that $\mathbf{k}_\perp \cdot \hat{\mathbf{g}} \sim 1/\lambda$ and $\mathbf{k}_\perp \cdot \hat{\mathbf{Y}} \sim 1/W$ to find the Bragg condition to next order in λ/W. This is done by finding the solution to (B.9) at $\tau_\mu + \Delta\tau$, by setting

$$\frac{\mathrm{d}f}{\mathrm{d}\tau}\Big|_{\tau_\mu + \Delta\tau} = \left(2Kg + k_x\frac{\mathrm{d}x_c}{\mathrm{d}\tau} + k_y\frac{\mathrm{d}y_c}{\mathrm{d}\tau} - \frac{(\mathbf{k}_\perp \cdot \hat{\mathbf{g}})(\mathbf{k}_\perp \cdot \hat{\mathbf{Y}})}{2\Psi_{YY}}\frac{\mathrm{d}\alpha}{\mathrm{d}\tau}\right)_{\tau_\mu + \Delta\tau} = 0. \quad (B.13)$$

Note that the last term in (B.8) was dropped, since it contributes an order smaller. Equation (B.13) determines the value of $\Delta\tau$, which is given by

$$\Delta\tau \approx \frac{\frac{(\mathbf{k}_\perp \cdot \hat{\mathbf{g}}_\mu)(\mathbf{k}_\perp \cdot \hat{\mathbf{Y}}_\mu)}{2\Psi_{YY\mu}}\left(\frac{\mathrm{d}\alpha}{\mathrm{d}\tau}\right)_\mu}{2\frac{\mathrm{d}K}{\mathrm{d}\tau}\big|_\mu g_\mu - \frac{(\mathbf{k}_\perp \cdot \hat{\mathbf{g}}_\mu)^2}{2\Psi_{YY\mu}}\left(\frac{\mathrm{d}\alpha}{\mathrm{d}\tau}\right)^2_\mu}, \quad (B.14)$$

where we can easily verify that $\Delta\tau \sim W/\lambda$ as anticipated. Having calculated the value of τ_μ and $\Delta\tau$ that satisfy the Bragg condition order by order in (B.9), (B.13) and (B.14), next, we approximate $f(\tau) \approx f(\tau_\mu + \Delta\tau) + \mathrm{d}^2f/\mathrm{d}\tau^2\big|_{\tau_\mu + \Delta\tau}(\tau - \tau_\mu - \Delta\tau)^2/2$. We find

$$f(\tau_\mu + \Delta\tau) \approx f(\tau_\mu) + \Delta\tau\frac{\mathrm{d}f}{\mathrm{d}\tau}\Big|_{\tau_\mu} + \frac{1}{2}\Delta\tau^2\frac{\mathrm{d}^2f}{\mathrm{d}\tau^2}\Big|_{\tau_\mu} \approx f_0(\tau_\mu) - \frac{\frac{\mathrm{d}K}{\mathrm{d}\tau}\big|_\mu g_\mu \frac{\left(\mathbf{k}_\perp \cdot \hat{\mathbf{Y}}_\mu\right)^2}{2\Psi_{YY\mu}}}{2\frac{\mathrm{d}K}{\mathrm{d}\tau}\big|_\mu g_\mu - \frac{2K^2_\mu}{\Psi_{YY\mu}}\left(\frac{\mathrm{d}\alpha}{\mathrm{d}\tau}\right)^2_\mu}, \quad (B.15)$$

where f_0 is given by (B.4) and the second derivative term in (B.15) is given by

$$\frac{\mathrm{d}^2f}{\mathrm{d}\tau^2}\Big|_{\tau_\mu + \Delta\tau} \approx \frac{\mathrm{d}^2f}{\mathrm{d}\tau^2}\Big|_{\tau_\mu} = 2\frac{\mathrm{d}K}{\mathrm{d}\tau}\Big|_\mu g_\mu - \frac{2K^2_\mu}{\Psi_{YY\mu}}\left(\frac{\mathrm{d}\alpha}{\mathrm{d}\tau}\right)^2_\mu. \quad (B.16)$$

Note that the phase in (B.15) contains terms ~ 1 that cannot be recovered by restricting the stationary phase calculation to zeroth-order, that is, by calculating $\mathrm{d}f_0/\mathrm{d}\tau = 0$ and keeping the term $-(\mathbf{k}_\perp \cdot \hat{\mathbf{Y}})^2/4\Psi_{YY}$ in (B.3) constant.

We are now in a position to perform the steepest-descent integral in (B.2). We find the following expression for the scattered amplitude in Cartesian coordinates:

$$A_r(t) = A_{ant}\int \mathrm{d}k_x\mathrm{d}k_y\, F_{xy,\mu}(k_x, k_y)\delta\hat{n}(k_x, k_y)\exp\left[i\left(2s_\mu(k_x, k_y) + k_x x_{c\mu} + k_y y_{c\mu}\right)\right], \quad (B.17)$$

where the slowly varying function (filter) $F_{xy,\mu}(k_x, k_y)$ takes the form

$$F_{xy,\mu}(k_x, k_y) = -\frac{\Omega g_{ant}}{2c} \left[\frac{\Im[\Psi_{YY\mu}]}{\Psi_{YY\mu}} \right]^{\frac{1}{2}} \frac{\left[\hat{\mathbf{e}}^* \cdot (\boldsymbol{\epsilon}_{eq} - \mathbf{1}) \cdot \hat{\mathbf{e}} \right]_{\tau_\mu}}{n_\mu} \exp\left(i2\phi_{G\mu} \right)$$

$$\times \left(\frac{2i\pi}{2\frac{dK}{d\tau}\big|_\mu g_\mu - \frac{2K_\mu^2}{\Psi_{YY\mu}} \left(\frac{d\alpha}{d\tau}\right)^2_{\tau_\mu}} \right)^{\frac{1}{2}} \exp\left[-i \frac{\frac{dK}{d\tau}\big|_\mu g_\mu \frac{\left(\mathbf{k}_\perp \cdot \hat{\mathbf{Y}}_\mu\right)^2}{2\Psi_{YY\mu}}}{2\frac{dK}{d\tau}\big|_\mu g_\mu - \frac{2K_\mu^2}{\Psi_{YY\mu}} \left(\frac{d\alpha}{d\tau}\right)^2_\mu} \right].$$

(B.18)

Next, we calculate the scattered power following the same procedure as Hall-Chen *et al.* (2022*b*). For this calculation, we need the turbulence correlation function C, defined as the Fourier transform of the density-fluctuation wavenumber power spectrum in Cartesian (k_x, k_y) coordinates,

$$C(\mathbf{r}, t, \Delta\mathbf{r}, \Delta t) = \frac{\langle \delta n(\mathbf{r} + \Delta\mathbf{r}, t + \Delta t) \delta n(\mathbf{r}, t) \rangle_T}{\langle \delta n^2 \rangle_T}$$

$$= \int dk_x dk_y \, \hat{C}(\mathbf{r}, t, k_x, k_y, z = 0, \Delta t) \exp\left[i(k_x \Delta x + k_y \Delta y) \right].$$

(B.19)

Here, $\langle \delta n^2 \rangle_T$ is the root-mean-square value of the density-fluctuation power. The function $\hat{C}$ is given by

$$\hat{C}(\mathbf{r}, t, k_x, k_y) = \frac{1}{\langle \delta n^2 \rangle_T} \int dk'_x dk'_y \langle \delta\hat{n}(k_x, k_y) \delta\hat{n}^*(k'_x, k'_y) \rangle_T$$

$$\times \exp\left[i(k_x - k'_x)x + i(k_y - k'_y)y \right].$$

(B.20)

We order $k_x - k'_x \sim k_y - k'_y \sim 1/L$. We use (B.20) for $\hat{C}$ to calculate the scattered power. We start by calculating the product $\langle |A_r|^2 \rangle_T$, which is given by

$$\langle |A_r(t)|^2 \rangle_T = |A_{ant}|^2 \int dk_x dk_y \, F_{xy,\mu}(k_x, k_y) \exp\left[if_0(\tau_\mu) \right]$$

$$\times \int dk'_x dk'_y \, F^*_{xy,\mu'}(k'_x, k'_y) \exp\left[-if_0(\tau_{\mu'}) \right]$$

$$\times \langle \delta\hat{n}(k_x, k_y) \delta\hat{n}^*(k'_x, k'_y) \rangle_T,$$

(B.21)

where μ' is the scattering position corresponding to (k'_x, k'_y), different from (k_x, k_y). Note that $F_{xy,\mu}$ does not change significantly if k_x or k_y change by a small amount of order $\sim 1/L$. This means that we can neglect the differences $k_x - k'_x \sim k_y - k'_y \sim 1/L$ between $F_{xy,\mu}(k_x, k_y)$ and $F^*_{xy,\mu'}(k'_x, k'_y)$, so that $F^*_{xy,\mu'}(k'_x, k'_y) \approx F^*_{xy,\mu}(k_x, k_y)$. The last step to calculate $\langle |A_r(t)|^2 \rangle_T$ is to compute the difference in the large phase $f_0(\tau_\mu) - f_0(\tau_{\mu'})$. Since $f_0 \sim L/\lambda$, it is important to keep the differences $k_x - k'_x \sim k_y - k'_y \sim 1/L$; these differences will provide an order unity contribution to the phase. Straightforward calculations lead to

$$2s_\mu - 2s_{\mu'} + k_x x_{c\mu} - k'_x x_{c\mu'} + k_y y_{c\mu} - k'_y y_{c\mu'} \approx (k_x - k'_x)x_{c\mu} + (k_y - k'_y)y_{c\mu},$$

(B.22)

where we used the Bragg condition (B.10) and the definition of $s = \int K\,\mathrm{d}l$ in Cartesian coordinates (see (2.5)). Using (B.22) and $F_{xy,\mu'}^*(k_x', k_y') \approx F_{xy,\mu}^*(k_x, k_y)$, we can relate the expression for $\langle |A_r(t)|^2\rangle_T$ to the correlation function in (B.20). Defining $p_r = \langle |A_r(t)|^2\rangle_T$, we find

$$\frac{p_r}{P_{ant}} = \int \mathrm{d}k_x \mathrm{d}k_y \, |F_{xy,\mu}|^2 \langle \delta n^2\rangle_T \hat{C}(\mathbf{r}_{c\mu}, t, k_x, k_y), \tag{B.23}$$

where $\mathbf{r}_{c\mu} = (x_{c\mu}, y_{c\mu}, z = 0)$. The correlation function is related to the 2-D wavenumber power spectrum via $\langle |\delta\hat{n}(k_x, k_y)|^2\rangle_T = \langle \delta n^2\rangle_T \hat{C}(\mathbf{r}, t, k_x, k_y, z = 0, \Delta t = 0)$. The Cartesian filter function $|F_{xy,\mu}|^2$ in (B.23) can be calculated directly using (B.18) and is given by

$$
\begin{aligned}
|F_{xy,\mu}|^2 = {} & 2\pi \left(\frac{\Omega g_{ant}}{2c}\right)^2 \frac{\left|\hat{\mathbf{e}}^* \cdot (\boldsymbol{\epsilon}_{eq} - \mathbf{1}) \cdot \hat{\mathbf{e}}\right|_{\tau_\mu}^2}{n_\mu^2} \\
& \times \frac{\Im[\Psi_{YY}]_\mu}{|\Psi_{YY}|_\mu} \frac{\exp\left[-\dfrac{\left(2\frac{\mathrm{d}K}{\mathrm{d}\tau}\right)_\mu^2 g_\mu^2}{\left|2\frac{\mathrm{d}K}{\mathrm{d}\tau}g - \frac{2K^2}{\Psi_{YY}}\left(\frac{\mathrm{d}\alpha}{\mathrm{d}\tau}\right)^2\right|_\mu^2} \dfrac{2\left(\mathbf{k}_\perp \cdot \hat{\mathbf{Y}}\right)^2}{\Delta k_{\mu2}^2} \right]}{\left|2\frac{\mathrm{d}K}{\mathrm{d}\tau}g - \frac{2K^2}{\Psi_{YY}}\left(\frac{\mathrm{d}\alpha}{\mathrm{d}\tau}\right)^2\right|_\mu},
\end{aligned}
\tag{B.24}
$$

where $\mathbf{k}_\perp \cdot \hat{\mathbf{Y}} = k_x \sin\alpha_\mu - k_y \cos\alpha_\mu$ (see (3.5)), and we have introduced the wavenumber resolution $\Delta k_{\mu2} = 2\left(-1/\Im[1/\Psi_{YY\mu}]\right)^{\frac{1}{2}} = 2|\Psi_{YY\mu}|/\Im[\Psi_{YY\mu}]^{\frac{1}{2}} \sim 1/W$ as defined by Hall-Chen *et al.* (2022*b*). Note that the polarisation piece for the O-mode can be written as $\left|\hat{\mathbf{e}}^* \cdot (\boldsymbol{\epsilon}_{eq} - \mathbf{1}) \cdot \hat{\mathbf{e}}\right|^2 = \omega_{pe}^4/\Omega^4$.

Equation (B.24) for $|F_{xy,\mu}|^2$ is (3.8) in the main text. We note that (B.23) does not exactly recover the expressions of Gusakov *et al.* (2014, 2017). Equation (B.23) can be further simplified by using the Bragg condition and the analytic beam-tracing solution, which we describe next. We will recover (3.9) in the main text. This result is valid for general beam initial conditions. By using Gusakov's initial conditions in (A.15), we will recover the expressions for the scattered power (auto-correlation) derived by Gusakov *et al.* (2014, 2017).

We want to express $|F_{xy,\mu}|^2$ as a function of its variables k_x and k_y. The function $|F_{xy,\mu}(k_x, k_y)|^2$ in (B.23) is a function of (k_x, k_y) through the Bragg condition relating τ_μ to k_x and k_y (see (B.9)). We proceed to calculate the different terms in (B.23). Using the Bragg condition $k_x \approx -2K_{x\mu}$, the ray-tracing solution for the central ray and the analytic expression for Ψ_{YY} (see (2.10)), we proceed to simplify the terms outside of the exponential in (B.23). Using the formulae

$$\frac{\mathrm{d}K}{\mathrm{d}\tau}\bigg|_\mu g_\mu = -\frac{2}{K_0 L}\frac{K_{x\mu}}{K_0}, \tag{B.25}$$

and

$$\left(\frac{\mathrm{d}\alpha}{\mathrm{d}\tau}\right)_\mu = \frac{\sin\alpha_0}{K_0 L}\frac{K_0^2}{K_\mu^2}, \tag{B.26}$$

we find

$$
2\frac{\mathrm{d}K}{\mathrm{d}\tau}\Big|_\mu g_\mu - 2\frac{K_\mu^2}{\Psi_{YY\mu}}\left(\frac{\mathrm{d}\alpha}{\mathrm{d}\tau}\right)_\mu^2 =
$$
$$
-\frac{4\Psi'_{yy0}}{K_0 L}\frac{K_\mu^4/K_0^4}{-\frac{1}{2}\sin^2\alpha_0 + \Psi'_{yy0}\left(\frac{K_x^3}{K_0^3} + 3\sin^2\alpha_0\frac{K_x}{K_0} - \frac{\sin^2\alpha_0}{\cos\alpha_0}(\cos^2\alpha_0 - \sin^2\alpha_0)\right)}.
$$
(B.27)

We then obtain

$$
\frac{\Im[\Psi_{YY}]_\mu}{|\Psi_{YY}|_\mu\left|2\frac{\mathrm{d}K}{\mathrm{d}\tau}g - 2\frac{K^2}{\Psi_{YY}}\left(\frac{\mathrm{d}\alpha}{\mathrm{d}\tau}\right)^2\right|_\mu} = \frac{K_0^2 L}{4K_\mu}\frac{\sqrt{2\Im[\Psi_{yy0}]}}{|\Psi_{yy0}|W_{Y\mu}},
$$
(B.28)

where we have used $W_{Y\mu} = (2/\Im[\Psi_{YY\mu}])^{\frac{1}{2}}$ and

$$
\Im[\Psi_{YY\mu}] = \frac{\Im[\Psi_{yy0}]\frac{K_\mu^2}{K_0^2}}{\left|\frac{K_{x\mu}}{K_0} + 2\Psi'_{yy0}\left(\frac{\cos^2\alpha_0 - \sin^2\alpha_0}{\cos\alpha_0}\frac{K_{x\mu}}{K_0} + \sin^2\alpha_0 - \frac{K_{x\mu}^2}{K_0^2}\right)\right|^2}.
$$
(B.29)

With respect to the terms inside the exponential in (B.23), the k_2-wavenumber resolution $\Delta k_{\mu 2}$ takes the following form:

$$
\Delta k_{\mu 2}^2 = \frac{4|\Psi_{YY\mu}|^2}{\Im[\Psi_{YY\mu}]} =
$$
(B.30)
$$
\frac{4}{\Im[\Psi'_{yy0}]}\frac{\left|-\frac{1}{2}\sin^2\alpha_0 + \Psi'_{yy0}\left(\frac{K_x^3}{K_0^3} + 3\sin^2\alpha_0\frac{K_x}{K_0} - \frac{\sin^2\alpha_0}{\cos\alpha_0}(\cos^2\alpha_0 - \sin^2\alpha_0)\right)\right|^2}{K_\mu^6/K_0^6}\frac{K_0}{L}.
$$
(B.30)

Using (B.30) for $\Delta k_{\mu 2}$ and employing (B.25) and (B.27), the argument of the exponential in $|F_{xy,\mu}|^2$ (see (B.23)) can be written as $\exp[-h(k_x, k_y)]$, where

$$
h(k_x, k_y) = \frac{2\left(2\frac{\mathrm{d}K}{\mathrm{d}\tau}\big|_\mu g_\mu\right)^2}{\left|\frac{\mathrm{d}K}{\mathrm{d}\tau}g - 2\frac{K^2}{\Psi_{YY}}\left(\frac{\mathrm{d}\alpha}{\mathrm{d}\tau}\right)^2\right|_\mu^2}\frac{\left(\mathbf{k}_\perp \cdot \hat{\mathbf{Y}}_\mu\right)^2}{\Delta k_{\mu 2}^2}
$$
$$
= \frac{K_0 L}{2}\frac{\Im[\Psi'_{yy0}]}{|\Psi'_{yy0}|^2}\frac{K_{x\mu}^4}{K_\mu^4}\left(\frac{k_y}{K_0} - \frac{k_x\sin\alpha_\mu}{K_0\cos\alpha_\mu}\right)^2.
$$
(B.31)

We express h in normalised quantities to emphasise that h is large, $h \sim K_0 L \gg 1$, unless $k_y \approx k_x\tan\alpha_\mu$. The k_y dependence of the integrand in (B.23) is through the exponential term (via h) and through the turbulence spectrum $\langle|\delta\hat{n}(k_x, k_y)|^2\rangle_T$. Given the assumption of large h, we can further simplify the expression for $|F_{xy,\mu}|^2$

by performing the k_y integral using Laplace's method (Bender & Orszag 1978). This leads to (3.9), which can be proven as follows. The Gaussian integral in k_y is dominated by contributions where $\partial h/\partial k_y \approx 0$, which takes place for a given $k_{y\star}$. This suggests expanding h around $k_{y\star}$, giving $h(k_x, k_y) \approx h(k_x, k_{y\star}) + (1/2)(k_y - k_{y\star})^2 \partial^2 h/\partial k_y^2 |_{k_{y\star}}$. To calculate $\partial h/\partial k_y$ and $\partial^2 h/\partial k_y^2$, we first use (A.9) to express $\sin \alpha_\mu / \cos \alpha_\mu$ as a function of $K_{x\mu}$, giving $\sin \alpha_\mu / \cos \alpha_\mu = K_0 \sin \alpha_0 / K_{x\mu}$. Then, we employ the expression $K_{x\mu} \approx -k_x/2 + \sin \alpha_0 (k_y + 2K_0 \sin \alpha_0) K_0/k_x$ in (B.12), giving $\partial K_{x\mu}/\partial k_y \approx \sin \alpha_0 K_0/k_x$. Using this, we find

$$\frac{\partial h}{\partial k_y}\bigg|_{k_x, k_y} \approx L \frac{\Im[\Psi'_{yy0}]}{|\Psi'_{yy0}|^2} \frac{K_{x\mu}^4}{K_\mu^4} \left(\frac{k_y}{K_0} - k_x \frac{\sin \alpha_0}{K_{x\mu}} \right) \left(1 + \frac{K_0^2 \sin^2 \alpha_0}{K_{x\mu}^2} \right), \qquad \text{(B.32)}$$

where we have neglected terms small in $(k_y - k_x \tan \alpha_\mu)$. The dominant contribution to the integral comes from k_y satisfying the extrema condition $\partial h/\partial k_y = 0$, which gives

$$k_{y\star} = k_x \sin \alpha_0 \frac{K_0}{K_{x\mu\star}} \approx -2K_0 \sin \alpha_0, \qquad \text{(B.33)}$$

where we used once more (B.12). Using (B.32), we calculate $\partial^2 h/\partial k_y^2$ and evaluate it at $k_{y\star}$, giving

$$\frac{\partial^2 h}{\partial k_y^2}\bigg|_{k_x, k_{y\star}} = \frac{L}{K_0} \frac{\Im[\Psi'_{yy0}]}{|\Psi'_{yy0}|^2} \frac{K_{x\mu\star}^4}{K_{\mu\star}^4} \left(1 + \frac{K_0^2 \sin^2 \alpha_0}{K_{x\mu\star}^2} \right)^2 \approx \frac{L}{K_0} \frac{\Im[\Psi'_{yy0}]}{|\Psi'_{yy0}|^2} = \frac{\Im[\Psi_{yy0}]}{|\Psi_{yy0}|^2}. \qquad \text{(B.34)}$$

Putting together (B.31) and (B.34), we find that the exponential term in (B.23), $\exp[-h(k_x, k_y)]$, is given approximately by

$$\exp[-h(k_y)] \approx \exp\left[-\frac{\Im[\Psi_{yy0}]}{2|\Psi_{yy0}|^2}(k_y + 2K_0 \sin \alpha_0)^2 \right] = \exp\left[\frac{-2(k_y + 2K_0 \sin \alpha_0)^2}{\Delta k_y^2} \right]. \qquad \text{(B.35)}$$

Equation (B.35) is the Gaussian exponential term in k_y in (3.9) and (3.10). In this expression, we recover the wavenumber resolution of the DBS diagnostic Δk_y in Cartesian coordinates. Note the difference between Δk_y in the lab frame, which is constant along the path and only depends on initial conditions, and $\Delta k_{\mu 2}$, which is the wavenumber resolution in the beam frame obtained by Hall-Chen *et al.* (2022*b*), which depends strongly on the position along the path (see (B.30)). For the resolution in k_y, we find $\Delta k_y^2 = 4|\Psi_{yy0}|^2/\Im[\Psi_{yy0}]$ (see (3.10)), which simplifies to the particular case of $\Delta k_y = 2/\rho$ for the initial conditions chosen by Gusakov *et al.* (2014, 2017). Note that the value $2/\rho$ is simply a lower limit to the diagnostic wavenumber resolution. Putting (B.35) together with (B.28), we recover the full expression for $|F_{xy,\mu}|^2$ in (3.9), including the $1/K_\mu W_{Y\mu}$ dependence outside of the exponential. Performing the integral over k_y, we recover (3.8) for $|F_{x\mu}|^2(k_x) = \int dk_y |F_{xy,\mu}|^2(k_x, k_y)$.

Appendix C. Mapping the density between beam-aligned and Cartesian coordinates

In this appendix, we establish the relation between the beam-aligned representation of the density, as used by Hall-Chen *et al.* (2022*b*), and the Cartesian representation of the density that is employed by Gusakov *et al.* (2014, 2017). We note that the two representations are independent of beam-tracing or scattering physics, and are simply a manifestation of two different frames of reference in which to express the density fluctuations. The relation between the density expressed in both frames is used in Appendix D to state the equivalence between the Doppler backscattered amplitude of Hall-Chen *et al.* (2022*b*) and of Gusakov *et al.* (2014, 2017).

We start from the definition of the beam-aligned representation of the density, $\delta \hat{n}_b$, as given by (102) of Hall-Chen *et al.* (2022*b*). In the 2-D linear layer, it takes the following form:

$$\delta n(\mathbf{r}) = \int \mathrm{d}k_1 \mathrm{d}k_2 \ \delta \hat{n}_b(k_1, k_2) \exp\left[i(k_1 l + k_2 Y)\right]. \tag{C.1}$$

Here, l and Y are the two spatial dimensions that describe the small-scale fluctuations perpendicular to the background magnetic field and are aligned with the beam, k_1 and k_2 are the corresponding Fourier-conjugate wavenumber components, and we assume no variation in the direction parallel to the magnetic field ($u_{\parallel}$ of Hall-Chen *et al.* 2022*b*). The coordinate l is the arc length of the central ray, given by (2.9). To improve clarity and to provide physical intuition, in this appendix, we use l as the parameter that the different functions depend on along the path, such as $x_c(l)$, $\alpha(l)$, etc. instead of τ as we have used in the main body of this manuscript.

We now turn to the Cartesian density-fluctuation field δn given by (3.1), with $\mathbf{k}_{\perp} = k_x \hat{\mathbf{x}} + k_y \hat{\mathbf{y}}$. The coordinates (x, y) are related to (l, Y) in (C.1) by $x = x_c(l) + Y \sin \alpha(l)$, $y = y_c(l) - Y \cos \alpha(l)$ (see (3.2)). This gives the succinct form $(x, y) = \mathbf{q} + Y \hat{\mathbf{Y}}$, where $\mathbf{q} = (x_c, y_c)$ and $k_x x + k_y y = \mathbf{k}_{\perp} \cdot \left(\mathbf{q} + Y \hat{\mathbf{Y}}\right)$.

To relate the density-fluctuation spectra between beam-aligned and Cartesian coordinates in (C.1) and (3.1), we project one onto the other. We have

$$\delta \hat{n}_b(k_1, k_2) = \int \frac{\mathrm{d}Y \mathrm{d}l}{(2\pi)^2} \exp\left(-ik_1 l - ik_2 Y\right) \delta n(\mathbf{r})$$
$$= \int \frac{\mathrm{d}k_x \mathrm{d}k_y}{(2\pi)^2} \delta \hat{n}(k_x, k_y) \int \mathrm{d}Y \mathrm{d}l \exp\left[i f_{\mathbf{k}_{\perp}}(l, Y)\right], \tag{C.2}$$

where the function $f_{\mathbf{k}_{\perp}}(l, Y)$ is given by

$$f_{\mathbf{k}_{\perp}}(l, Y) = \mathbf{k}_{\perp} \cdot \left(\mathbf{q} + Y \hat{\mathbf{Y}}\right) - k_1 l - k_2 Y. \tag{C.3}$$

To find a useful relation between $\delta \hat{n}_b$ and $\delta \hat{n}$, we proceed to compute the integrals in l and Y in (C.8). We do so by calculating the point of stationary phase in the 2-D (l, Y) plane. We note that the unit vectors $\hat{\mathbf{g}}$ and $\hat{\mathbf{Y}}$ both depend on l, which needs to be taken into account when computing derivatives with respect to l (see (B.7)). The point of the stationary phase (l_b, Y_b) is given by the joint conditions $\partial f_{\mathbf{k}_{\perp}}/\partial l|_{l_b, Y_b} = \partial f_{\mathbf{k}_{\perp}}/\partial Y|_{l_b, Y_b} = 0$. Using (B.7), the derivatives of $f_{\mathbf{k}_{\perp}}$ with respect to l and Y are given by

$$\frac{\partial f_{\mathbf{k}_\perp}}{\partial l} = \mathbf{k}_\perp \cdot \hat{\mathbf{g}} \left(1 + Y \frac{d\alpha}{dl}\right) - k_1,$$
$$\frac{\partial f_{\mathbf{k}_\perp}}{\partial Y} = \mathbf{k}_\perp \cdot \hat{\mathbf{Y}} - k_2,$$
$$\text{(C.4)}$$

where we used the definition of $\mathbf{g} = d\mathbf{q}/d\tau$ and $dl = g d\tau$. The point of the stationary phase (l_b, Y_b) is determined by

$$k_1 = \mathbf{k}_\perp \cdot \hat{\mathbf{g}}_b \left(1 + Y_b \frac{d\alpha}{dl}\Big|_b\right),$$
$$k_2 = \mathbf{k}_\perp \cdot \hat{\mathbf{Y}}_b,$$
$$\text{(C.5)}$$

where the subscript $(.)_b$ means that functions are evaluated at (l_b, Y_b). It is worth commenting on the implications from (C.5). Given the dependence of $\hat{\mathbf{g}}$ and $\hat{\mathbf{Y}}$ on l, for a given $\mathbf{k}_\perp$, the second equation in (C.5) states that the value of k_2 determines the location l_b where (C.5) is satisfied. Equivalently, given $\mathbf{k}_\perp$, k_2 is determined uniquely by the location along the path l_b, independently of the coordinate Y_b. Having determined l_b, the value of k_1 then determines the location Y_b where (k_1, k_2) and $\mathbf{k}_\perp$ are resonant. Or yet equivalently, given $\mathbf{k}_\perp$ and l_b, k_1 is determined by the location perpendicular to the central ray Y_b.

Having calculated the location (l_b, Y_b) and the relation between $\mathbf{k}_\perp$ and (k_1, k_2), next we want to approximate $f_{\mathbf{k}_\perp}$ quadratically in $(l - l_b)$ and $(Y - Y_b)$. For that, we turn to compute the second derivatives of $f_{\mathbf{k}_\perp}$ with respect to l and Y, which are given by

$$\frac{\partial^2 f_{\mathbf{k}_\perp}}{\partial l^2} = -\mathbf{k}_\perp \cdot \hat{\mathbf{Y}} \frac{d\alpha}{dl} + Y \left(-\mathbf{k}_\perp \cdot \hat{\mathbf{Y}} \left(\frac{d\alpha}{dl}\right)^2 + \mathbf{k}_\perp \cdot \hat{\mathbf{g}} \frac{d^2\alpha}{dl^2}\right),$$
$$\frac{\partial^2 f_{\mathbf{k}_\perp}}{\partial l \partial Y} = \mathbf{k}_\perp \cdot \hat{\mathbf{g}} \frac{d\alpha}{dl},$$
$$\frac{\partial^2 f_{\mathbf{k}_\perp}}{\partial Y^2} = 0.$$
$$\text{(C.6)}$$

Using (C.6), we can write

$$f_{\mathbf{k}_\perp}(l, Y) \approx f_{\mathbf{k}_\perp}(l_b, Y_b) + \frac{(l - l_b)^2}{2} \frac{\partial^2 f_{\mathbf{k}_\perp}}{\partial l^2}\Big|_{l_b, Y_b} + (l - l_b)(Y - Y_b) \frac{\partial^2 f_{\mathbf{k}_\perp}}{\partial l \partial Y}\Big|_{l_b, Y_b}. \quad \text{(C.7)}$$

Computing the Gaussian integrals in l and Y using (C.7), we find the desired relation between $\delta\hat{n}(\mathbf{k}_\perp)$ and $\delta\hat{n}_b(k_1, k_2)$,

$$\delta\hat{n}_b(k_1, k_2) = \int \frac{dk_x dk_y}{2\pi} \frac{\delta\hat{n}(k_x, k_y)}{|\mathbf{k}_\perp \cdot \hat{\mathbf{g}} \, d\alpha/dl|_b} \exp\left[i\mathbf{k}_\perp \cdot \mathbf{q}_b - ik_1 l_b\right]. \quad \text{(C.8)}$$

This is the general relation between $\delta\hat{n}_b$ and $\delta\hat{n}$ in two dimensions. In the next section, we use (C.8) to prove the equivalence between the backscattering amplitude in two dimensions using a beam-aligned $\delta\hat{n}_b$, as done by Hall-Chen *et al.* (2022b), and using a Cartesian $\delta\hat{n}$, as done by Gusakov *et al.* (2014, 2017).

Appendix D. Relation of the scattered amplitude A_r between beam-aligned and Cartesian coordinates

In this appendix, we show the equivalence between the scattered amplitude A_r in beam-aligned coordinates, as used by Hall-Chen *et al.* (2022*b*), and Cartesian coordinates, as in (3.3) and used by Gusakov *et al.* (2014, 2017). This shows that both the beam-tracing model of Hall-Chen et al. (2022*b*) and the 2-D DBS model of Gusakov *et al.* (2014, 2017) are equivalent to each other: they are simply expressed in different frames of reference. A similar exercise for directly mapping the DBS power between both representations requires further work, which will be the subject of a future publication.

We start from the expression of the backscattered amplitude of (169) from Hall-Chen *et al.* (2022*b*), which in the 2-D linear layer takes the following form:

$$A_r(t) = A_{ant} \sum_\nu \int \mathrm{d}k_1 \mathrm{d}k_2 \; F_\nu(k_1, k_2) \; \delta\hat{n}_b(k_1, k_2, u_{||\nu}, t) \; \exp\left[i(2s_\nu + k_1 l_\nu)\right], \quad \text{(D.1)}$$

where F_ν is the effective filter function in beam-aligned coordinates and is given by

$$F_\nu(k_1, k_2) = -\left[\frac{i\pi}{\frac{\mathrm{d}K}{\mathrm{d}\tau}g} \frac{\Im[\Psi_{YY}]}{\Psi_{YY}}\right]_\nu^{\frac{1}{2}} \frac{\left[\hat{\mathbf{e}}^* \cdot (\boldsymbol{\epsilon}_{eq} - \mathbf{1}) \cdot \hat{\mathbf{e}}\right]_\nu}{n_\nu} \exp\left(i2\phi_{G\nu} - \frac{i}{4}\frac{k_2^2}{\Psi_{YY\nu}}\right). \quad \text{(D.2)}$$

The notation $[.]_\nu$ means that functions of τ have been evaluated at τ_ν, the location along the central-ray path where the Bragg condition for backscattering is satisfied. In beam-aligned coordinates, the Bragg condition is

$$k_1 \approx -2K(\tau_\nu). \quad \text{(D.3)}$$

Note that only the lowest-order contribution $\sim 1/\lambda$ to the Bragg condition has been kept here. For a given k_1, there can exist several τ_ν associated to it. This explains the sum $\sum_\nu$ in (D.1). The scattering amplitude in (D.1) only has contributions from backscattering events. Any forward scattering component is absent because of the Bragg condition.

We note that τ_ν differs from the τ_μ calculated using Cartesian coordinates throughout the manuscript by a correction of order $\sim W/\lambda$, which we calculate later in this appendix. This difference between τ_μ and τ_ν is of limited importance in the main text of this manuscript, but it is important to consider in order to show the equivalence of the scattered amplitude in both representations.

To show that the formulae for the scattered amplitude in Cartesian and beam-aligned coordinates are equivalent, we make use of (C.8) and insert it into (D.1) for the amplitude. By exchanging the order of integration, we have

$$A_r(t) = -A_{ant} \sum_\nu \int \frac{\mathrm{d}k_x \mathrm{d}k_y}{2\pi} \delta\hat{n}(k_x, k_y) \int \frac{\mathrm{d}k_1 \mathrm{d}k_2}{|\mathbf{k}_\perp \cdot \hat{\mathbf{g}} \, \mathrm{d}\alpha/\mathrm{d}l|_b} \left[\frac{i\pi}{\frac{\mathrm{d}K}{\mathrm{d}\tau}g} \frac{\Im[\Psi_{YY}]}{\Psi_{YY}}\right]_\nu^{\frac{1}{2}}$$
$$\times \frac{\left[\hat{\mathbf{e}}^* \cdot (\boldsymbol{\epsilon}_{eq} - \mathbf{1}) \cdot \hat{\mathbf{e}}\right]_\nu}{n_\nu} \exp\left(i2\phi_{G\nu}\right) \exp\left[if\right], \quad \text{(D.4)}$$

where the phase f is given by

$$f = 2s_v + \mathbf{k}_\perp \cdot \mathbf{q}_b + k_1(l_v - l_b) - \frac{k_2^2}{4\Psi_{YYv}}. \tag{D.5}$$

We recall from Appendix C that the subscript $(.)_b$ corresponds to the location (l_b, Y_b) where the resonance condition in (C.5) takes place. We proceed to calculate the integrals in k_1 and k_2 by the method of stationary phase (Bender & Orszag 1978).

The phase f in (D.5) is made of a large piece, $2s_v + \mathbf{k}_\perp \cdot \mathbf{q}_b + k_1(l_v - l_b) \sim L/\lambda$, and a small piece, $-k_2^2/4\Psi_{YYv} \sim 1$. The large piece forces $l_v - l_b \ll L$. One can see this by using the stationary-phase method. Indeed, $\partial f/\partial k_1 = 0$ and $\partial f/\partial k_2 = 0$ give $l_b = l_v$ to lowest order.

We proceed by assuming $l_v - l_b \sim W$. We can then find the distance between a nearby point l_v to l_b. We can expand $\hat{\mathbf{Y}}_v - \hat{\mathbf{Y}}_b$ as $\hat{\mathbf{Y}}_v - \hat{\mathbf{Y}}_b \approx (l_v - l_b)\mathrm{d}\hat{\mathbf{Y}}/\mathrm{d}l|_b$. Multiplying by $\mathbf{k}_\perp$ and using (B.7), (C.5) and $\mathrm{d}\hat{\mathbf{Y}}/\mathrm{d}l|_b \approx \mathrm{d}\hat{\mathbf{Y}}/\mathrm{d}l|_v$, we find

$$\mathbf{k}_\perp \cdot \hat{\mathbf{Y}}_v - k_2 = \mathbf{k}_\perp \cdot \hat{\mathbf{g}}_v \frac{\mathrm{d}\alpha}{\mathrm{d}l}\bigg|_v (l_v - l_b) + O\left(\frac{1}{L}\right), \tag{D.6}$$

which results in $l_v - l_b \sim W$ as we predicted above. Equation (D.6) also shows that, for a given $\mathbf{k}_\perp$, we can change k_2 by moving in l_b. A similar exercise can be done for $\hat{\mathbf{g}}_v$, which gives $\mathbf{k}_\perp \cdot \hat{\mathbf{g}}_v - \mathbf{k}_\perp \cdot \hat{\mathbf{g}}_b \approx -\mathbf{k}_\perp \cdot \hat{\mathbf{Y}}_b(\mathrm{d}\alpha/\mathrm{d}l)|_b(l_v - l_b) - \mathbf{k}_\perp \cdot \hat{\mathbf{g}}_b(\mathrm{d}\alpha/\mathrm{d}l)^2|_b(l_v - l_b)^2/2 \sim 1/L$. In this case, we can use $\mathbf{k}_\perp \cdot \hat{\mathbf{g}}_v \approx \mathbf{k}_\perp \cdot \hat{\mathbf{g}}_b$.

We now Taylor-expand $\mathbf{q}_b$ in (D.5) in powers of $l_b - l_v$. Using $\mathrm{d}\mathbf{q}/\mathrm{d}l = \hat{\mathbf{g}}$ and (B.7), we have

$$\mathbf{q}_b \approx \mathbf{q}_v + \hat{\mathbf{g}}_v(l_b - l_v) - \hat{\mathbf{Y}}_v \frac{\mathrm{d}\alpha}{\mathrm{d}l}\bigg|_v \frac{(l_b - l_v)^2}{2}. \tag{D.7}$$

Next, we use (D.6) and (D.7) to find a suitable expression of the phase in (D.5) in terms of powers of $l_b - l_v$, keeping terms up to ~ 1. We find

$$f \approx 2s_v + \mathbf{k}_\perp \cdot \mathbf{q}_v - \frac{(\mathbf{k}_\perp \cdot \hat{\mathbf{Y}}_v)^2}{4\Psi_{YYv}} - \left(k_1 - \mathbf{k}_\perp \cdot \hat{\mathbf{g}}_v + \frac{(\mathbf{k}_\perp \cdot \hat{\mathbf{Y}}_v)(\mathbf{k}_\perp \cdot \hat{\mathbf{g}}_v)(\mathrm{d}\alpha/\mathrm{d}l)_v}{2\Psi_{YYv}}\right)(l_b - l_v)$$
$$- \frac{(\mathbf{k}_\perp \cdot \hat{\mathbf{g}}_v)^2(\mathrm{d}\alpha/\mathrm{d}l)_v^2}{4\Psi_{YYv}}(l_b - l_v)^2. \tag{D.8}$$

Note that the dependence on k_2 in (D.4) is now hidden in l_b through (D.6).

We compute the k_2 integral in (D.4) by changing variables of integration from k_2 to l_b by $\mathrm{d}k_2 = |\mathbf{k}_\perp \cdot \hat{\mathbf{g}} \, \mathrm{d}\alpha/\mathrm{d}l|_b \mathrm{d}l_b$. The integral in l_b is a complex Gaussian. We find

$$\int \frac{\mathrm{d}k_2}{|\mathbf{k}_\perp \cdot \hat{\mathbf{g}} \, \mathrm{d}\alpha/\mathrm{d}l|_b} \exp\left[if\right] = \left(\frac{-4i\pi\Psi_{YYv}}{(\mathbf{k}_\perp \cdot \hat{\mathbf{g}}_v)^2(\mathrm{d}\alpha/\mathrm{d}l)_v^2}\right)^{\frac{1}{2}} \exp\left[ih_v(k_1)\right], \tag{D.9}$$

where the function $h_v(k_1)$ is given by

$$h_v(k_1) = 2s_v + \mathbf{k}_\perp \cdot \mathbf{q}_v + \frac{\mathbf{k}_\perp \cdot \hat{\mathbf{Y}}_v(k_1 - \mathbf{k}_\perp \cdot \hat{\mathbf{g}}_v)}{\mathbf{k}_\perp \cdot \hat{\mathbf{g}}_v \, (\mathrm{d}\alpha/\mathrm{d}l)_v} + \frac{\Psi_{YYv}\left(k_1 - \mathbf{k}_\perp \cdot \hat{\mathbf{g}}_v\right)^2}{(\mathbf{k}_\perp \cdot \hat{\mathbf{g}}_v)^2(\mathrm{d}\alpha/\mathrm{d}l)_v^2}. \tag{D.10}$$

Having completed the k_2 integral, (D.4) now takes the following form:

$$A_r(t) = -A_{ant} \sum_\nu \int \mathrm{d}k_x \mathrm{d}k_y \, \delta\hat{n}(k_x, k_y) \int \mathrm{d}k_1 \left[\frac{\Im[\Psi_{YY}]}{(g\mathrm{d}K/\mathrm{d}\tau)(\mathbf{k}_\perp \cdot \hat{\mathbf{g}})^2 (\mathrm{d}\alpha/\mathrm{d}l)^2} \right]_\nu^{\frac{1}{2}}$$

$$\times \frac{\left[\hat{\mathbf{e}}^* \cdot (\boldsymbol{\epsilon}_{eq} - \mathbf{1}) \cdot \hat{\mathbf{e}} \right]_\nu}{n_\nu} \exp(i2\phi_{G\nu}) \exp\left[ih_\nu(k_1)\right]. \tag{D.11}$$

Note that the integrand under the k_1 integral sign in (D.11) has a non-trivial dependence on k_1 through the Bragg condition $k_1 = -2K_\nu$ in (D.3). However, the integral can be simplified by noting that $k_1 - \mathbf{k}_\perp \cdot \hat{\mathbf{g}}_\mu \sim 1/W$. This follows from the Bragg conditions (3.4) and (D.3) and the exponential term in (D.9). Computing the difference between (3.4) and (D.3), we find

$$k_1 - \mathbf{k}_\perp \cdot \hat{\mathbf{g}}_\mu \approx -2\frac{\mathrm{d}K}{\mathrm{d}l}\bigg|_\mu (l_\nu - l_\mu). \tag{D.12}$$

Since $k_1 - \mathbf{k}_\perp \cdot \hat{\mathbf{g}}_\mu \sim 1/W$, to make the exponential term in (D.9) of order unity, we find $l_\nu - l_\mu \sim W$ and we Taylor-expand terms in h_ν in powers of $(k_1 - \mathbf{k}_\perp \cdot \hat{\mathbf{g}}_\mu)$. When calculating $\mathrm{d}h_\nu/\mathrm{d}k_1$ and $\mathrm{d}^2 h_\nu/\mathrm{d}k_1^2$, we will make use of (D.12), so that terms that are functions of l_ν can be calculated by using the chain rule

$$\frac{\mathrm{d}}{\mathrm{d}k_1} = -\frac{1}{2(\mathrm{d}K/\mathrm{d}l)_\nu} \frac{\mathrm{d}}{\mathrm{d}l_\nu}. \tag{D.13}$$

Equation (D.13) is particularly useful for computing $\mathrm{d}(\mathbf{k}_\perp \cdot \hat{\mathbf{g}}_\nu)/\mathrm{d}k_1$ and $\mathrm{d}(\mathbf{k}_\perp \cdot \hat{\mathbf{Y}}_\nu)/\mathrm{d}k_1$. Using (B.7) and (D.13), we have

$$\frac{\mathrm{d}(\mathbf{k}_\perp \cdot \hat{\mathbf{g}}_\nu)}{\mathrm{d}k_1} = \frac{(\mathrm{d}\alpha/\mathrm{d}l)_\nu}{2(\mathrm{d}K/\mathrm{d}l)_\nu} \mathbf{k}_\perp \cdot \hat{\mathbf{Y}}_\nu \sim \frac{\lambda}{W} \ll 1,$$
$$\frac{\mathrm{d}(\mathbf{k}_\perp \cdot \hat{\mathbf{Y}}_\nu)}{\mathrm{d}k_1} = -\frac{(\mathrm{d}\alpha/\mathrm{d}l)_\nu}{2(\mathrm{d}K/\mathrm{d}l)_\nu} \mathbf{k}_\perp \cdot \hat{\mathbf{g}}_\nu \sim 1, \tag{D.14}$$

where we have employed $\mathbf{k}_\perp \cdot \hat{\mathbf{Y}}_\nu \sim 1/W$. Using (D.12), (D.13) and (D.14), the large phase term $2s_\nu + \mathbf{k}_\perp \cdot \mathbf{q}_\nu$ can be expanded as

$$2s_\nu + \mathbf{k}_\perp \cdot \mathbf{q}_\nu = 2s_\mu + \mathbf{k}_\perp \cdot \mathbf{q}_\mu + \frac{1}{4(\mathrm{d}K/\mathrm{d}l)_\mu}(k_1 - \mathbf{k}_\perp \cdot \hat{\mathbf{g}}_\mu)^2 + O\left(\frac{\lambda}{W}\right), \tag{D.15}$$

where we have used the Bragg condition $2K_\mu + \mathbf{k}_\perp \cdot \hat{\mathbf{g}}_\mu \approx 0$. Next, we expand the third and fourth terms of h_ν in (D.10). We have

$$\frac{\mathbf{k}_\perp \cdot \hat{\mathbf{Y}}_\nu (k_1 - \mathbf{k}_\perp \cdot \hat{\mathbf{g}}_\nu)}{\mathbf{k}_\perp \cdot \hat{\mathbf{g}}_\nu \, (\mathrm{d}\alpha/\mathrm{d}l)_\nu} = \mathbf{k}_\perp \cdot \hat{\mathbf{Y}}_\mu \frac{k_1 - \mathbf{k}_\perp \cdot \hat{\mathbf{g}}_\mu}{\mathbf{k}_\perp \cdot \hat{\mathbf{g}}_\mu \, (\mathrm{d}\alpha/\mathrm{d}l)_\mu} - \frac{(k_1 - \mathbf{k}_\perp \cdot \hat{\mathbf{g}}_\mu)^2}{2(\mathrm{d}K/\mathrm{d}l)_\mu} + O\left(\frac{\lambda}{W}\right),$$
$$\frac{\Psi_{YY\nu}(k_1 - \mathbf{k}_\perp \cdot \hat{\mathbf{g}}_\nu)^2}{(\mathbf{k}_\perp \cdot \hat{\mathbf{g}}_\nu)^2 (\mathrm{d}\alpha/\mathrm{d}l)_\nu^2} = \frac{\Psi_{YY\mu}(k_1 - \mathbf{k}_\perp \cdot \hat{\mathbf{g}}_\mu)^2}{(\mathbf{k}_\perp \cdot \hat{\mathbf{g}}_\mu)^2 (\mathrm{d}\alpha/\mathrm{d}l)_\mu^2} + O\left(\frac{\lambda}{W}\right). \tag{D.16}$$

The phase h_ν now has explicit dependence on $(k_1 - \mathbf{k}_\perp \cdot \hat{\mathbf{g}}_\mu)$ and it is given by

$$h_\nu = 2s_\mu + \mathbf{k}_\perp \cdot \mathbf{q}_\mu + \frac{\mathbf{k}_\perp \cdot \hat{\mathbf{Y}}_\mu (k_1 - \mathbf{k}_\perp \cdot \hat{\mathbf{g}}_\mu)}{\mathbf{k}_\perp \cdot \hat{\mathbf{g}}_\mu \, (\mathrm{d}\alpha/\mathrm{d}l)_\mu} + \frac{\mathrm{d}^2 h_\nu}{\mathrm{d}k_1^2}\bigg|_\mu \frac{(k_1 - \mathbf{k}_\perp \cdot \hat{\mathbf{g}}_\mu)^2}{2} + O\left(\frac{\lambda}{W}\right),$$
(D.17)

where $\mathrm{d}^2 h_\nu/\mathrm{d}k_1^2\big|_\mu \sim L\lambda$ is given by

$$\frac{\mathrm{d}^2 h_\nu}{\mathrm{d}k_1^2}\bigg|_\mu = \frac{2\Psi_{YY\mu}}{(\mathbf{k}_\perp \cdot \hat{\mathbf{g}}_\mu)^2 (\mathrm{d}\alpha/\mathrm{d}l)_\mu^2} - \frac{1}{2(\mathrm{d}K/\mathrm{d}l)_\mu}.$$
(D.18)

With this approximation to h_ν, the integral over k_1 in (D.11) becomes a Gaussian integral that can be easily evaluated. We find that the integral in k_1 in (D.11) recovers (B.17) and (B.18). This is proof that the representations of the density in beam-aligned coordinates used by Hall-Chen *et al.* (2022*b*) and in Cartesian coordinates used by Gusakov *et al.* (2014, 2017) are completely equivalent.

We note that the equivalence obtained here between the beam-aligned and Cartesian representation of the density is proven for the scattered amplitude and not directly for the power. It is possible to directly prove the equivalence in the scattered power from the beam-aligned expression in (k_1, k_2) of Hall-Chen *et al.* (2022*b*) to the Cartesian expression in (k_x, k_y) in (3.7), (3.8). This requires mapping the correlation functions between beam-aligned $\hat{C}_b$ and Cartesian coordinates $\hat{C}$, which is non-trivial and will be the subject of a future publication.

It is worth commenting on the equivalence of the scattered-power contributions for beam-aligned and Cartesian coordinates when regarded as a one-dimensional integral in k_x or k_1. In this case, it is straightforward to directly map the Cartesian and beam-aligned representations of the scattered power, as follows.

The backscattered power in Cartesian coordinates from (3.9) can be rewritten as an integral over the beam-aligned k_1 (Hall-Chen *et al.* 2022*b*). To express the one-dimensional integral in (3.9) in terms of k_1, change variables using $\mathrm{d}k_x = \mathrm{d}k_1 K_\mu/|K_{x\mu}| = \mathrm{d}k_1/|\cos\alpha_\mu|$, where we used (A.9). We find

$$\frac{p_r}{P_{ant}} \approx \pi^{\frac{3}{2}} K_0 L \frac{e^4}{m_e^2 \epsilon_0^2 \Omega^4} \sum_\mu \int \mathrm{d}k_1 \frac{\langle|\delta\hat{n}_\mu(k_x, -2K_0 \sin\alpha_0)|^2\rangle_T}{|K_{x\mu}/K_0| W_{Y\mu}},$$
(D.19)

where we have used (B.25) to write the term $|g\mathrm{d}K/\mathrm{d}\tau|_\mu$ as a function of $K_{x\mu}$. The dependence of k_x on k_1 in (D.19) can be explained as follows. First, k_x is related to the location along the path l_μ through the Bragg condition in Cartesian coordinates in (3.6). In turn, l_μ is related to k_1 through the Bragg condition when expressed in beam-aligned coordinates, $k_1 \approx -2K_\mu$ to lowest order, since the difference $l_\mu - l_\nu$ is of order $\sim W$ as we just saw.

Equation (D.19) recovers the same result as Hall-Chen *et al.* (2022*b*) when using $\langle|\delta\hat{n}_{b,\mu}|^2\rangle_T$. The one-dimensional change of variables between k_x and k_1 shows that, to lowest order and at scales $\sim 1/\lambda$, the density-fluctuation spectra in Cartesian coordinates is related to the beam-aligned spectrum of Hall-Chen *et al.* (2022*b*) by a rotation of angle α_μ, and we have $\langle|\delta\hat{n}_\mu(k_x, -2K_0 \sin\alpha_0)|^2\rangle_T = \langle|\delta\hat{n}_{b,\mu}(k_x \cos\alpha_\mu - 2K_0 \sin\alpha_0 \sin\alpha_\mu, 0)|^2\rangle_T$. Noting that $k_x \cos\alpha_\mu - 2K_0 \sin\alpha_0 \sin\alpha_\mu \approx -2K_\mu \approx k_1$ by use of the Bragg conditions, we have therefore recovered the equivalence in the one-dimensional scattered power in both representations.

REFERENCES

BALAKIN, A., BALAKINA, M. & WESTERHOF, E. 2008 ECRH power deposition from a quasi-optical point of view. *Nucl. Fusion* **48** (6), 065003.

BALAKIN, A.A., BALAKINA, M.A., PERMITIN, G.V. & SMIRNOV, A.I. 2007 Quasi-optical description of wave beams in smoothly inhomogeneous anisotropic media. *J. Phys. D: Appl. Phys.* **40** (14), 4285–4296.

BARNES, M., PARRA, F.I. & LANDREMAN, M. 2019 Stella: an operator-split, implicit–explicit δf-gyrokinetic code for general magnetic field configurations. *J. Comput. Phys* **391**, 365–380.

BELRHALI, N., RUIZ RUIZ, J., PARRA, F. & HALL-CHEN, V.H. 2025 Limitations of Gaussian beam tracing near a turning-point caustic. *In Preparation for Journal of Plasma Physics*.

BENDER, C.M. & ORSZAG, S.A. 1978 *Advanced Mathematical Methods for Scientists and Engineers*. McGraw-Hill.

BERCZYŃSKI, P., KRAVTSOV, Y.A. & ŻEGLINSKI, G. 2008 Gaussian beam diffraction in inhomogeneous and nonlinear media: analytical and numerical solutions by complex geometrical optics. *Cent. Eur. J. Phys.* **6** (3), 603–611.

BLANCO, E. & ESTRADA, T. 2013 Two-dimensional full-wave simulations of radial correlation Doppler reflectometry in linear and non-linear regimes. *Plasma Phys. Control. Fusion* **55** (125006). doi: 10.1088/0741-3335/55/12/125006

BORNATICI, M. & MAJ, O. 2003 Wave beam propagation in a weakly inhomogeneous isotropic medium: paraxial approximation and beyond. *Plasma Phys. Control. Fusion* **45** (5), 707–719.

BRAVENEC, R.V., CHEN, Y., CANDY, J., WAN, W. & PARKER, S. 2013 A verification of the gyrokinetic microstability codes GEM, GYRO, and GS2. *Phys. Plasmas* **20** (104506),

BRAVENEC, R.V. & NEVINS, W.M. 2006 System for simulating fluctuation diagnostics for application to turbulence computations. *Rev. Sci. Instrum.* **77** (1), 015101, 1–10. 10.1063/1.2151857

CANDY, J. & BELLI, E. 2014 GYRO technical guide. General atomics technical report GA-A26818, P.O. Box 85608, San Diego, CA 92186-5608, USA.

CANDY, J., BELLI, E.A. & BRAVENEC, R.V. 2016 A high-accuracy Eulerian gyrokinetic solver for collisional plasmas. *J. Comput. Phys.* **324**, 73–93.

CANDY, J. & WALTZ, R.E. 2003*a* An Eulerian gyrokinetic-Maxwell solver. *J. Comput. Phys.* **186** (545), 545–581.

CANDY, J. & WALTZ, R.E. 2003*b* Anomalous transport scaling in the DIII-D tokamak matched by supercomputer simulation. *Phys. Rev. Lett.* **91** (045001). doi: 10.1103/PhysRevLett.91.045001

CASPERSON, L.W. 1973 Gaussian light beams in inhomogeneous media. *Appl. Opt.* **12** (10), 2434–2441.

CATTO, P.J. 1978 Linearized gyro-kinetics. *Plasma Phys.* **20** (7), 719–722.

ČERVENÝ, V., POPOV, M.M. & PŠENČÍK, I. 1982 Computation of wave fields in inhomogeneous media – Gaussian beam approach. *Geophys. J. Intl* **70** (1), 109–128. arXiv: https://academic.oup.com/gji/article-pdf/70/1/109/2085354/70-1-109.pdf

CIMA, G., BRAVENEC, R.V., WOOTTON, A.J., REMPEL, T.D., GANDY, R.F., WATTS, C. & KWON, M. 1995 Core temperature fluctuations and related heat transport in the Texas experimental tokamak-Upgrade. *Phys. Plasmas* **2** (720), 720–726.

CODA, S. & PORKOLAB, M. 1992 A phase contrast interferometer on DIII-D. *Rev. Sci. Instrum.* **63** (10), 4974–4976.

CONWAY, G.D., LECHTE, C., FOCHI, A. & the ASDEX Upgrade Team 2015 Assessment of Doppler reflectometry accuracy using full-wave codes with comparison to beam-tracing and analytic expressions. In Proc. 12th Intl. Reflectometry Workshop - IRW12, IAEA.

CONWAY, G.D., LECHTE, C., POLI, E. , MAJ, O. & the ASDEX Upgrade Team Recent progress in modelling the resolution and localization of Doppler reflectometry measurements. In Proc. 14th Intl. Reflectometry Workshop - IRW14, 2019, IAEA.

CONWAY, G.D., TROESTER, C., SCHIRMER, J., ANGIONI, C., HOLZHAUER, E., JENKO, F., MERZ, F., POLI, E., SCOTT, B. , SUTTROP, W. & the ASDEX Upgrade Team. 2007 Doppler reflectometry on ASDEX Upgrade: Foundations and latest results. In Proc. 8th Intl. Reflectometry Workshop - IRW08, IAEA.

COSTLEY, A.E., CRIPWELL, P., PRENTICE, R. & SIPS, A.C.C. 1990 Recent developments in microwave reflectometry at JET. *Rev. Sci. Instrum.* **61** (10), 2823–2828.

CREELY, A.J., GREENWALD, M.J., BALLINGER, S.B., BRUNNER, D., CANIK, J., DOODY, J., FÜLÖP, T., GARNIER, D.T., GRANETZ, R. & GRAY, T.K. 2020 Overview of the SPARC tokamak. *J. Plasma Phys.* **86** (5), 865860502.

CRIPWELL, P., COSTLEY, A.E. & HUBBARD, A.E. 1989 Proceedings of the 16th European Conference on Controlled Fusion and Plasma Physics, (ed. S., SEGRE, H., KNOEPFEL & E., SINDONI), European Physical Society, Vol. 12B, pp. 75.

DIMITS, A.M. 2000 Comparisons and physics basis of tokamak transport models and turbulence simulations. *Phys. Plasmas* **7** (3), 969–983.

FERNÁNDEZ-MARINA, F., ESTRADA, T. & BLANCO, E. 2014 Turbulence radial correlation length measurements using Doppler reflectometry in TJ-II. *Nucl. Fusion* **54** (072001). doi: 10.1088/0029-5515/54/7/072001

FONCK, R.J., DUPERREX, P.A. & PAUL, S.F. 1990 Plasma fluctuation measurements in tokamaks using beam-plasma interactions. *Rev. Sci. Instrum.* **61** (11), 3487–3495.

FRIEMAN, E.A. & CHEN, L. 1982 Nonlinear gyrokinetic equations for low-frequency electromagnetic waves in general plasma equilibria. *Phys. Fluids* **25** (3), 502–508.

GARBET, X. 2001 Turbulence in fusion plasmas: key issues and impact on transport modelling. *Plasma Phys. Control. Fusion* **43** (A251), A251–A266.

GARBET, X., IDOMURA, Y., VILLARD, L. & WATANABE, T.H. 2010 Gyrokinetic simulations of turbulent transport. *Nucl. Fusion* **50** (4), 043002.

GOLDSMITH, P.F. 1998 *Quasioptical Systems: Gaussian Beam Quasioptical Propagation and Applications*. IEEE Press.

GREENWALD, M. 2010 Verification and validation for magnetic fusion. *Phys. Plasmas* **17** (058101). doi: 10.1063/1.3298884

GUSAKOV, E. *et al.* 2013 Anomalous transport and multi-scale drift turbulence dynamics in tokamak ohmic discharge as measured by high resolution diagnostics and modeled by full-f gyrokinetic code. *Plasma Phys. Control. Fusion* **55** (124034). doi: 10.1088/0741-3335/55/12/124034

GUSAKOV, E., IRZAK, M. & POPOV, A. 2014 Radial correlation reflectometry at oblique probing wave incidence (linear scattering theory predictions). *Plasma Phys. Control. Fusion* **56** (025009). doi: 10.1088/0741-3335/56/2/025009

GUSAKOV, E.Z., IRZAK, M.A., POPOV, A.Y., KHITROV, S.A. & TEPLOVA, N.V. 2017 Reconstruction of turbulence radial wave number spectra based on the multi-frequency microwave Doppler backscattering data. *Phys. Plasmas* **24** (022119). doi: 10.1063/1.4976545

GUSAKOV, E.Z. & KRUTKIN, O.L. 2017 Recovery of the characteristics of plasma turbulence from the radial correlation backscattering diagnostics. *Plasma Phys. Rep.* **43** (6), 605–613.

GUSAKOV, E.Z. & POPOV, A.Y. 2011 Theory of radial correlation Doppler reflectometry. In Proc. 38th EPS Conference on Plasma Physics, 27 June–1 July (P4.056).

GUSAKOV, E.Z. & SURKOV, A.V. 2004 Spatial and wavenumber resolution of Doppler reflectometry. *Plasma Phys. Control. Fusion* **46** (7), 1143–1162.

GUSAKOV, E.Z., SURKOV, A.V. & POPOV, A.Y. 2005 Multiple scattering effect in Doppler reflectometry. *Plasma Phys. Control. Fusion* **47** (959), 959–974.

GUTTENFELDER, W. *et al.* 2022 NSTX-U theory, modeling and analysis results. *Nucl. Fusion* **62** (4), 042023.

HALL-CHEN, V. *et al.* 2022*a* Validating and optimising mismatch tolerance of Doppler backscattering measurements with the beam model. *Rev. Sci. Instrum.* **93** (10), 103536.

HALL-CHEN, V.H. , HILL, P. & contributors 2025 scotty beam tracing. Available at https://github.com/beam-tracing/Scotty, gitHub repository.

HALL-CHEN, V.H., PARRA, F.I. & HILLESHEIM, J.C. 2022*b* Beam model of Doppler backscattering. *Plasma Phys. Control. Fusion* **64** (9), 095002.

HALL-CHEN, V.H. *et al.* 2022*c* Effect of mismatch on Doppler backscattering in MAST and MAST-U plasmas. arXiv: 10.48550/arXiv.2211.17141.

HAPPEL, T. *et al.* 2017 Comparison of detailed experimental wavenumber spectra with gyrokinetic simulation aided by two-dimensional fullwave simulations. *Plasma Phys. Control. Fusion* **59** (054009). doi: 10.1088/1361-6587/aa645b

HENNEQUIN, P., HONORÉ, C., TRUC, A., QUÉMÉNEUR, A., FENZI-BONIZEC, C., BOURDELLE, C., GARBET, X., HOANG, G. & The tore supra team 2006 Fluctuation spectra and velocity profile from Doppler backscattering on tore supra. *Nucl. Fusion* **46** (S771). doi: 10.1088/0029-5515/46/9/S12

HENNEQUIN, P., HONORÉ, C., TRUC, A., QUÉMÉNEUR, A., LEMOINE, N., CHAREAU, J.-M. & SABOT, R. 2004 Doppler backscattering system for measuring fluctuations and their perpendicular velocity on tore supra. *Rev. Sci. Instrum.* **75** (10), 3881–3883.

HILLESHEIM, J.C., CROCKER, N.A., PEEBLES, W.A., MEYER, H., MEAKINS, A., FIELD, A.R., DUNAI, D., CARR, M., HAWKES, N. & the MAST Team 2015 Doppler backscattering for spherical tokamaks and measurement of high-k density fluctuation wavenumber spectrum in MAST. *Nucl. Fusion* **55** (073024). doi: 10.1088/0029-5515/55/7/073024

HILLESHEIM, J.C., DELABIE, E., MEYER, H., MAGGI, C.F., MENESES, L., POLI, E. & the JET Contributors 2016 Stationary zonal flows during the formation of the edge transport barrier in the JET tokamak. *Phys. Rev. Letter* **116** (065002). doi: 10.1103/PhysRevLett.116.065002

HILLESHEIM, J.C., HOLLAND, C., SCHMITZ, L., KUBOTA, S., RHODES, T.L. & CARTER, T.A. 2012 2D full wave modeling for a synthetic Doppler backscattering diagnostic. *Rev. Sci. Instrum.* **83** (10E331). doi: 10.1063/1.4733549

HIRSCH, M. & HOLZHAUER, E. 2004 Doppler reflectometry with optimized temporal resolution for the measurement of turbulence and its propagation velocity. *Plasma Phys. Control. Fusion* **46** (593), 593–609.

HIRSCH, M., HOLZHAUER, E., BALDZUHN, J. & KURZAN, B. 2001 Doppler reflectometry for the investigation of propagating density perturbations. *Rev. Sci. Instrum.* **72**, 324–327.

HOLLAND, C. 2016 Validation metrics for turbulent plasma transport. *Phys. Plasmas* **23** (060901). doi: 10.1063/1.4954151

HOLLAND, C. *et al.* 2012 Testing gyrokinetic simulations of electron turbulence. *Nucl. Fusion* **52** (063028). doi: 10.1088/0029-5515/52/6/063028

HOLLAND, C., WHITE, A.E., McKEE, G.R., SHAFER, M.W., CANDY, J., WALTZ, R.E., SCHMITZ, L. & TYNAN, G.R. 2009 Implementation and application of two synthetic diagnostics for validating simulations of core tokamak turbulence. *Phys. Plasmas* **16** (052301). doi: 10.1063/1.3085792

HOLZHAUER, E., HIRSCH, M., GROSSMANN, T., BRAÑAS, B. & SERRA, F. 1998 Theoretical and experimental investigation of the phase-runaway in microwave reflectometry. *Plasma Phys. Control. Fusion* **40** (11), 1869–1886.

HORTON, W. 1999 Drift waves and transport. *Rev. Mod. Phys.* **71** (3), 735–778.

HOWARD, N.T., WHITE, A.E., REINKE, M., GREENWALD, M., HOLL, C., CANDY, J. & WALK, J.R. 2013 Validation of the gyrokinetic model in ITG and TEM dominated L-mode plasmas. *Nucl. Fusion* **53** (123011). doi: 10.1088/0029-5515/53/12/123011

HUTCHINSON, I.H. 2002 *Principles of Plasma Diagnostics (2nd ed.)*. Cambridge University Press.

IKEDA, K. 2007 Progress in the iter physics basis. *Nucl. Fusion* **47** (6), E01.

IVANOV, P.G., SCHEKOCHIHIN, A.A., DORL, W., FIELD, A.R. & PARRA, F.I. 2020 Zonally dominated dynamics and dimits threshold in curvature-driven ITG turbulence. *J. Plasma Phys.* **86** (5), 855860502.

JENKO, F., DORLAND, W., KOTSCHENREUTHER, M. & ROGERS, B.N. 2000 Electron temperature gradient driven turbulence. *Phys. Plasmas* **7**, 1904–1910.

KOTSCHENREUTHER, M. 1995 Comparison of initial value and eigenvalue codes for kinetic toroidal plasma instabilities. *Comput. Phys. Commun.* **88**, 128–140.

KRUTKIN, O.L. *et al.* 2019a Validation of full-f global gyrokinetic modeling results against the FT-2 tokamak doppler reflectometry data using synthetic diagnostics. *Nucl. Fusion* **59** (096017). doi: 10.1088/1741-4326/ab1cfb

KRUTKIN, O.L., GUSAKOV, E.Z., HEURAUX, S. & LECHTE, C. 2019b Nonlinear doppler reflectometry power response. Analytical predictions and full-wave modelling. *Plasma Phys. Control. Fusion* **61** (045010). doi: 10.1088/1361-6587/ab0236

LECHTE, C., CONWAY, G.D., GOERLER, T. , HAPPEL, T. & the ASDEX Upgrade Team 2020 Fullwave doppler reflectometry simulations for density turbulence spectra in ASDEX upgrade using GENE and IPF-FD3D. *Plasma Sci. Technol.* **22** (064006). doi: 10.1088/2058-6272/ab7ce8

LECHTE, C., CONWAY, G.D., GOERLER, T. , TROESTER-SCHMID, C. & the ASDEX Upgrade Team 2017 X mode doppler reflectometry k-spectral measurements in ASDEX upgrade: experiments and simulations. *Plasma Phys. Control. Fusion* **59** (075006). doi: 10.1088/1361-6587/aa6fe7

LEERINK, S. *et al.* 2012 Multiscale investigations of drift-wave turbulence and plasma flows: measurements and total-distribution-function gyrokinetic simulations. *Phys. Rev. Lett.* **109** (16), 165001.

LEERINK, S., BULANIN, V.V., GUSAKOV, E.Z., HEIKKINEN, J., JANHUNEN, S.J., KIVINIEMI, T.P., KORPILO, T., NORA, M. & OGANDO, F. 2010 Synthetic doppler reflectometer diagnostic for nonlinear global gyrokinetic simulations. *Contrib. Plasma Phys.* **50** (3-5), 242–245. arXiv: https://onlinelibrary.wiley.com/doi/pdf/10.1002/ctpp.201010040

LIEWER, P.C. 1985 Measurements of microturbulence in tokamaks and comparisons with theories of turbulence and anomalous transport. *Nucl. Fusion* **25** (5), 543–621.

LIN, Y., NAZIKIAN, R., IRBY, J.H. & MARMAR, E.S. 2001 Plasma curvature effects on microwave reflectometry fluctuation measurements. *Plasma Phys. Control. Fusion* **43** (L1), L1–L8.

LOPEZ, N.A. & DODIN, I.Y. 2021 Metaplectic geometrical optics for modeling caustics in uniform and non-uniform media. *J. Opt.* **23** (2), 025601.

LOPEZ, N.A., KUR, E. & STROZZI, D.J. 2023 Intensity of focused waves near turning points. *Phys. Rev. E* **107** (5), 055204.

MAJ, O. 2005 The relationship between the Wigner-weyl kinetic formalism and the complex geometrical optics method. *J. Math. Phys.* **46**, 083510. https://pubs.aip.org/aip/jmp/article-pdf/doi/10.1063/1.1998833/15955142/083510_1_online.pdf

MAJ, O., BALAKIN, A.A. & POLI, E. 2010 Effects of aberration on paraxial wave beams: beam tracing versus quasi-optical solutions. *Plasma Phys. Control. Fusion* **52** (085006). doi: 10.1088/0741-3335/52/8/085006

MAJ, O., PEREVERZEV, G.V. & POLI, E. 2009 Validation of the paraxial beam-tracing method in critical cases. *Phys. Plasmas* **16** (062105). doi: 10.1088/0741-3335/52/8/085006

MAZZUCATO, E. 1976 Small-scale density fluctuations in the adiabatic toroidal compressor. *Phys. Rev. Lett.* **36** (14), 792–794.

NEVINS, W.M. *et al.* 2006 Characterizing electron temperature gradient turbulence via numerical simulation. *Phys. Plasmas* **13** (122306). doi: 10.1063/1.2402510

PATEL, B.S. *et al.* 2024 Pyrokinetics - a python library to standardise gyrokinetic analysis. *J. Open Source Softw.* **9** (95), 5866.

PEEBLES, W.A., JR., N.C., L., MASE, A., PARK, H. & SEMET, A. 1981 CW farinfrared laserscattering apparatus for plasma wave studies. *Rev. Sci. Instrum.* **52**, 360–370.

PEREVERZEV, G. 1992 Use of the multidimensional WKB method to describe propagation of lower hybrid waves in tokamak plasma. *Nucl. Fusion* **32** (7), 1091–1106.

PEREVERZEV, G.V. 1993 Paraxial WKB solution of a scalar wave equation, IPP–4/260. https://www.osti.gov/etdeweb/biblio/10192297

PEREVERZEV, G.V. 1996 *Paraxial WKB Solution of a Scalar Wave Equation*. Vol. 19. Springer.

PEREVERZEV, G.V. 1998 Beam tracing in inhomogeneous anisotropic plasmas. *Phys. Plasmas* **5** (10), 3529–3541. arXiv: https://doi.org/10.1063/1.873070.

POLI, E. *et al.* 2018 TORBEAM 2.0, a paraxial beam tracing code for electron-cyclotron beams in fusion plasmas for extended physics applications. *Comput. Phys. Commun.* **225**, 36–46.

POLI, E., PEETERS, A. & PEREVERZEV, G. 2001*a* TORBEAM, a beam tracing code for electron-cyclotron waves in tokamak plasmas. *Comput. Phys. Commun.* **136** (1), 90–104.

POLI, E., PEETERS, A.G. & PEREVERZEV, G.V. 2001*b* Boundary conditions for a Gaussian wave beam. *Phys. Plasmas* **8** (10), 4325–4330. arXiv: https://doi.org/10.1063/1.1401116.

POLI, E., PEREVERZEV, G., PEETERS, A. & BORNATICI, M. 2001*c* EC beam tracing in fusion plasmas. *Fusion Engng Des.* **53** (1), 9–21.

POLI, E., PEREVERZEV, G.V. & PEETERS, A.G. 1999 Paraxial Gaussian wave beam propagation in an anisotropic inhomogeneous plasma. *Phys. Plasmas* **6** (1), 5–11. arXiv: https://doi.org/10.1063/1.873254.

PRATT, Q. *et al.* 2023 Density wavenumber spectrum measurements, synthetic diagnostic development, and tests of quasilinear turbulence modeling in the core of electron-heated DIII-D H-mode plasmas. *Nucl. Fusion* **64** (1), 016001.

REN, Y. *et al.* 2020 Exploring the regime of validity of global gyrokinetic simulations with spherical tokamak plasmas. *Nucl. Fusion* **60** (026005). doi: 10.1088/1741-4326/ab5bf5

RHODES, T.L., PEEBLES, W.A., NGUYEN, X., VANZEELAND, M.A., DEGRASSIE, J.S., DOYLE, E.J., WANG, G. & ZENG, L. 2006 Millimeter-wave backscatter diagnostic for the study of short scale length plasma fluctuations. *Rev. Sci. Instrum.* **77** (10E922). doi: 10.1063/1.2235874

RUIZ, J.R., GUTTENFELDER, W., WHITE, A.E., HOWARD, N.T., CANDY, J., REN, Y., SMITH, D.R. & HOLLAND, C. 2020*a* Quantitative comparisons of electron-scale turbulence measurements in NSTX via synthetic diagnostics for high-k scattering. *Plasma Phys. Control. Fusion* **62** (075001). doi: 10.1088/1361-6587/ab82de

RUIZ, J.R., GUTTENFELDER, W., WHITE, A.E., HOWARD, N.T., CANDY, J., REN, Y., SMITH, D.R. & HOLLAND, C. 2020*b* Validation of gyrokinetic simulations in NSTX and projections for high-k turbulence measurements in NSTX-u. *Phys. Plasmas* **27** (122505). doi: 10.1088/1361-6587/ab82de

RUIZ, J.R., GUTTENFELDER, W., WHITE, A.E., HOWARD, N.T., CANDY, J., REN, Y., SMITH, D.R., LOUREIRO, N.F., HOLLAND, C. & DOMIER, C.W. 2019 Validation of gyrokinetic simulations of a national spherical torus eXperiment H-mode plasma and comparisons with a high-k scattering synthetic diagnostic. *Plasma Phys. Control. Fusion* **61** (115015). doi: 10.1088/1361-6587/ab4742

RUIZ, J.R. *et al.* 2022 Interpreting radial correlation Doppler reflectometry using gyrokinetic simulations. *Plasma Phys. Control. Fusion* **64** (055019). doi: 10.1088/1361-6587/ac5916

RUIZ, J.R. *et al.* 2015 Stabilization of electron-scale turbulence by electron density gradient in national spherical torus experiment. *Phys. Plasmas* **22** (122501). doi: 10.1063/1.4936110

SATTLER, S., HARTFUSS, H.J. & TEAM, W.-A. 1994 Experimental evidence for electron temperature fluctuations in the core plasma of the W7-AS stellarator. *Phys. Rev. Lett.* **72**, 653–656.

SCHIRMER, J., CONWAY, G.D., HOLZHAUER, E., W., S. , ZOHM, H. & the ASDEX Upgrade Team 2007 radial correlation length measurements on ASDEX upgrade using correlation Doppler reflectometry. *Plasma Phys. Control. Fusion* **49** (7), 1019–1039.

SHAFER, M.W., FONCK, R.J., MCKEE, G.R. & SCHLOSSBERG, D.J. 2006 Spatial transfer function for the beam emission spectroscopy diagnostic on DIII-D. *Rev. Sci. Instrum.* **77** (10F110). doi: 10.1063/1.2221908

SLUSHER, R.E. & SURKO, C.M. 1980 Study of density fluctuations in plasmas by smallangle CO2 laser scattering. *Phys. Fluids* **23**, 472–490.

SMIRNOV, A.P. *et al.* 2009 Proceedings of the 15th Workshop on ECE and ECRH (Singapore World Scientific), www.compxco.com/genray.html. pp. 301.

STAEBLER, G.M., KINSEY, J.E. & WALTZ, R.E. 2005 Gyro-Landau fluid equations for trapped and passing particles. *Phys. Plasmas* **12** (102508). doi: 10.1063/1.2044587

STROTH, U. *et al.* 2015 Experimental turbulence studies for gyro-kinetic code validation using advanced microwave diagnostics. *Nucl. Fusion* **55** (083027),

SURKO, C.M. & SLUSHER, R.E. 1976 Study of the density fluctuations in the adiabatic toroidal compressor scattering tokamak using CO2 laser. *Phys. Rev. Lett.* **37** (26), 1747–1750.

TERRY, P.W. *et al.* 2008 Validation in fusion research: towards guidelines and best practices. *Phys. Plasmas* **15** (062503). doi: 10.1063/1.2928909

TYNAN, G.R., FUJISAWA, A. & MCKEE, G. 2009 A review of experimental drift turbulence studies. *Plasma Phys. Control. Fusion* **51** (113001). doi: 10.1088/0741-3335/51/11/113001

WEBER, H., MAJ, O. & POLI, E. 2018 Paraxial expansion of the wave kinetic equation for electron cyclotron beams in turbulent plasmas. *J. Phys.: Conf. Ser.* **1125** (1), 012022.

WEISEN, H. 1988 The phase contrast method as an imaging diagnostic for plasma density fluctuations. *Rev. Sci. Instrum.* **59** (8), 1544–1549.

WHITE, A.E. 2019 Validation of nonlinear gyrokinetic transport models using turbulence measurements. *J. Plasma Phys.* **85** (925850102). doi: 10.1017/S0022377818001253

WHITE, A.E. *et al.* 2008 A correlation electron cyclotron emission diagnostic and the importance of multifield fluctuation measurements for testing nonlinear gyrokinetic turbulence simulations. *Rev. Sci. Instrum.* **79** (10), 103505. doi: 10.1063/1.2981186

WHITE, A.E. *et al.* 2008 Measurements of core electron temperature and density fluctuations in DIII-D and comparison to nonlinear gyrokinetic simulations. *Phys. Plasmas* **15** (056116). doi: 10.1063/1.2895408

WILSON, H., CHAPMAN, I., DENTON, T., MORRIS, W., PATEL, B., VOSS, G. , WALDON, C. & the STEP Team 2020 *Commercialising Fusion Energy, Vol. chapter 8: STEP-on the Pathway to Fusion Commercialization*. IOP Publishing Ltd.

KRAVTSOV, YU A. & BERCZYNSKI, P. 2007 Gaussian beams in inhomogeneous media: a review. *Stud. Geophys. Geod.* **51** (1), 1–36.